AFRL-AFOSR-UK-TR-2019-0006

Global Transient Growth Mechanisms in High-Speed Flows with Application to the Elliptic Cone

VASSILIOS Theofilis
NUMERICAL MODELLING SL.
CALLE DE MARIANO BARBACID, 1 - 9
BOADILLA DEL MONTE, 28660
ES

01/29/2019
Final Report

Air Force Research Laboratory
Air Force Office of Scientific Research
European Office of Aerospace Research and Development
Unit 4515 Box 14, APO AE 09421

REPORT DOCUMENTATION PAGE

Form Approved
OMB No. 0704-0188

1. REPORT DATE *(DD-MM-YYYY)*	2. REPORT TYPE	3. DATES COVERED *(From - To)*
29-01-2019	Final	15 Sep 2015 to 14 Sep 2018

4. TITLE AND SUBTITLE
Global Transient Growth Mechanisms in High-Speed Flows with Application to the Elliptic Cone

5a. CONTRACT NUMBER

5b. GRANT NUMBER
FA9550-15-1-0387

5c. PROGRAM ELEMENT NUMBER
61102F

6. AUTHOR(S)
VASSILIOS Theofilis

5d. PROJECT NUMBER

5e. TASK NUMBER

5f. WORK UNIT NUMBER

7. PERFORMING ORGANIZATION NAME(S) AND ADDRESS(ES)
NUMERICAL MODELLING SL.
CALLE DE MARIANO BARBACID, 1 - 9
BOADILLA DEL MONTE, 28660 ES

8. PERFORMING ORGANIZATION REPORT NUMBER

9. SPONSORING/MONITORING AGENCY NAME(S) AND ADDRESS(ES)
EOARD
Unit 4515
APO AE 09421-4515

10. SPONSOR/MONITOR'S ACRONYM(S)
AFRL/AFOSR IOE

11. SPONSOR/MONITOR'S REPORT NUMBER(S)
AFRL-AFOSR-UK-TR-2019-0006

12. DISTRIBUTION/AVAILABILITY STATEMENT
A DISTRIBUTION UNLIMITED: PB Public Release

13. SUPPLEMENTARY NOTES

14. ABSTRACT
Work performed has been a continuation and extension of AFOSR-supported modal global instability research in hypersonic
ow on the elliptic cone, initiated during Grant FA8655-12-1-2004 (2012-2015). Four distinct, interrelated paths were followed: (a) local transient growth analysis at several characteristic locations on the cone surface, (b) development and performance of global transient growth analysis on the cone via direct solution of the BiGlobal Singular Value Decomposition (SVD) problem, (c) further development of the nonlinear PSE-3D algorithm, which permits laminar-turbulent transition prediction on account of nonlinear interaction of either modal or non-modal linear disturbances and (d) development of LiGHT, a new massively parallel EVP and SVD solver for prediction of hypersonic transition, the latest version of which has been delivered to AFRL.

15. SUBJECT TERMS
EOARD, turbulence and transition, transient growth in high speed flows

16. SECURITY CLASSIFICATION OF:			17. LIMITATION OF ABSTRACT	18. NUMBER OF PAGES	19a. NAME OF RESPONSIBLE PERSON
a. REPORT	b. ABSTRACT	c. THIS PAGE			SMITH, DOUGLAS
Unclassified	Unclassified	Unclassified	SAR		19b. TELEPHONE NUMBER *(Include area code)* 314-235-6013

Standard Form 298 (Rev. 8/98)
Prescribed by ANSI Std. Z39.18

FINAL REPORT

Global transient growth mechanisms in high-speed flows, with application to the elliptic cone

Principal Investigator: VASSILIOS THEOFILIS, Ph.D.[1,2,3]
Graduate Student: HELIO QUINTANILHA JR[1]
Undergraduate Student: PANAGIOTIS B KATARAS[1]
Collaborators: PEDRO PAREDES, Ph.D.[4,5], **ARDESHIR HANIFI, Ph.D.**[6]

[1]**University of Liverpool, UK**
eMail: v.theofilis@liverpool.ac.uk

[2]**Universidade Federal Fluminense, Brasil**

[3]**NuModelling S.L. (Spain) and NuModelling LTD (UK)**

[4]**School of Aeronautics, Universidad Politécnica de Madrid, Spain**

[5]**NASA Langley Research Center**

[6]**Linne Flow Center, KTH Stockholm, Sweden**

EOARD Program Officers: RUSSELL CUMMINGS, Ph. D., DOUGLAS SMITH, Ph. D.
AFOSR Program Officer: IVETT LEYVA, Ph.D.

Dec 14, 2018

This page intentionally left blank

Executive Summary

This document is the final report on research activities jointly sponsored by the European Office of Aerospace Research and Development and the Air Force Office of Scientific Research, Air Force Material Command, USAF, under Grant number FA9550-15-1-0387, entitled **Global transient growth mechanisms in high-speed flows, with application to the elliptic cone**. The Grant has been jointly monitored by Dr. Russ Cummings and Dr. Douglas Smith of EOARD and Dr. Ivett Leyva of AFOSR. The present report covers the 36-month period from September 15, 2015, the inception of the grant, to Sept. 14, 2018, the end of the grant.

Work performed has been a continuation and extension of AFOSR-supported modal global instability research in hypersonic flow on the elliptic cone, initiated during Grant FA8655-12-1-2004 (2012-2015). Four distinct, interrelated paths were followed: (a) local transient growth analysis at several characteristic locations on the cone surface, (b) development and performance of global transient growth analysis on the cone via direct solution of the BiGlobal Singular Value Decomposition (SVD) problem, (c) further development of the nonlinear PSE-3D algorithm, which permits laminar-turbulent transition prediction on account of nonlinear interaction of either modal or non-modal linear disturbances and (d) development of *LiGHT*, a new massively parallel EVP and SVD solver for prediction of hypersonic transition, the latest version of which has been delivered to AFRL.

Research in (a) has extracted base flow profiles along the entire surface of the cone and analyzed them with respect to their ability to sustain transient energy growth in a local analysis context. The cone surface was discretized at a number of streamwise (axial) locations at each of which the azimuthal direction was also discretized fine enough for distinct physical instability phenomena known to exist from the modal analysis, such as attachment-line, crossflow or centerline instabilities, to manifest themselves in the spectrum. In addition to the known from earlier work modal growth, substantial transient growth was also discovered for the first time at several locations on the cone surface. Comparisons of results obtained at two altitudes, $h = 33km$ and $h = 21km$, showed that *transient growth becomes increasingly important as the flight altitude increases.*

In (b) the three-dimensional linear stability equations for arbitrarily complex geometries were derived in general tensor form. The equations governing global modal and non-modal instability on the elliptic cone were derived as a particular case and solved as an initial value problem (IVP) using Singular Value Decomposition (SVD) of the related discretized matrix. The assumption of periodicity of flow perturbations along the azimuthal direction of the elliptic cone was relaxed and the first compressible non-modal BiGlobal instability analysis was performed. Consistently with local transient growth analysis results obtained in (a), it was found that *transient growth is increasingly significant as the flight altitude increases and the unit Reynolds number decreases.* The formalism developed is applicable to *any complex three-dimensional geometry*, and will be exploited in future work.

In (c) the development of a new nonlinear three-dimensional (plane-marching) Parabolized Stability Equations (NL-PSE3D) code has been substantially advanced. Validations have been performed using well-known flow instability mechanisms, such as streamwise-oriented and crossflow linear disturbances; excellent agreement with literature results has been obtained. The NL-PSE3D methodology is currently being exploited by Dr. Paredes in his current research at NASA Langley.

The line of work in (d) was motivated by both modal and nonmodal analyses performed, which revealed the limitations of the computational approach employed in both our previous modal and our current non-modal work in terms of its parallel (in)efficiency when applied to the solution of very large EVP and SVD problems. This, combined with a request of Dr. Roger Kimmel (AFRL) to employ (at AFRL) a global instability analysis code to study the available flight-testing transition data, led the PI to start, at the beginning of the second year of the present effort, the development of a new computer code, denominated *LiGHT*, (*Li*near *G*lobal instability for *H*ypersonic *T*ransition). During the lifetime of the present grant this effort has advanced to the point of the code being able to solve massively parallel real and complex matrix EVP and SVD problems; *the latest version of the LiGHT code has been delivered to AFRL* during a Window on Science visit of the PI to Dayton in July 2018.

This page intentionally left blank

Acknowledgments

This material is based upon work supported by the Air Force Office of Scientific Research, Air Force Material Command, USAF, under Grant number FA9550-15-1-0387. Access to the Copper Cray XE6m supercomputer was provided by project AFVAW10102F62 with Dr. Nicholas Bisek as Principal Investigator and is gratefully acknowledged. I certify that there were no subject inventions to declare during the performance of this Grant. The U.S Government is authorized to reproduce and distribute reprints for Governmental purpose notwithstanding any copyright notation thereon. The views and conclusions contained herein are those of the author and should not be interpreted as necessarily representing the official policies or endorsements, either expressed or implied, of the Air Force Office of Scientific Research or the U.S. Government.

This page intentionally left blank

Contents

List of Figures

List of Tables

Activities supported by the Grant

Personnel Supported

- Helio R. de A. Quintanilha Jr. *Research Student*. Fully supported by this Grant as registered Ph.D. student at the Department of Mechanical, Materials and Aerospace Engineering of the University of Liverpool. Travel support used for the 23rd AIAA Computational Fluid Dynamics Conference, Denver, CO, USA, June 2017, Flow Autumn School on Aeroacoustics and Thermoacoustics of Propulsion Systems, Stockholm, Sweden, October 2017 and 58th Israel Annual Conference on Aerospace Sciences, Tel Aviv and Haifa, Israel, March 2018
- V. Theofilis. *Professor*. Travel support used for: AFOSR Annual Review meetings, Arlington, VA, June 2016 and July 2018 and Hampton, VA, July 2017; 57th Israel Annual Conference on Aerospace Sciences, Tel Aviv and Haifa, Israel, March 2017; 23rd AIAA Computational Fluid Dynamics Conference, Denver, CO, June 2017; APS Fluid Dynamics meeting, Denver, CO, Nov 2017; ERCOFTAC SIG-33 Meeting, Paraty, Brazil; GAMM 61st Ludwig Prandtl Memorial Lecture, Munich, Germany, March 2018

Dissertations

- Ph.D. Thesis
  - Helio R. de A. Quintanilha Jr. *Global transient growth mechanisms in high-speed flows, with application to the elliptic cone* (in preparation)
- M.Eng. Thesis
  - Panagiotis Belesiotis Kataras *Nonmodal Stability of Hypersonic Flow on an Eliptic Cone* (May 2017)

Publications

- Journal Articles
  - Tumuklu O, Theofilis V, Levin DA (2018) *On the unsteadiness of shock–laminar boundary layer interactions of hypersonic flows over a double cone*, Physics of Fluids, 30:106111 **(Featured Article)**
  - Tumuklu O, Levin DA, Theofilis V (2018) *Investigation of unsteady, hypersonic, laminar separated flows over a double cone geometry using a kinetic approach*, Physics of Fluids, 30:046103 **(Editor's Pick)**
  - Taira K, Brunton SL, Dawson STM, Rowley CW, Colonius T, McKeon BJ, Schmidt OT, Gordeyev S, Theofilis V, Ukeiley LS (2017) *Modal Analysis of Fluid Flows: An Overview*, AIAA Journal, 55(12):4013-4041
  - Theofilis V (2017) *The linearized pressure Poisson equation for global instability analysis of incompressible flows*, Theoretical and Computational Fluid Dynamics, 31:623–642

- Paredes P, Gosse R, Theofilis V & Kimmel R (2016) *Linear modal instabilities of hypersonic flow over an elliptic cone*, Journal of Fluid Mechanics 804:442-466

- Book Chapters
  - Paredes P, Hanifi A, Theofilis V & Henningson D S (2015) *The nonlinear PSE-3D concept for transition predictoin in flows with a single slowly-varying spatial direction*, Procedia IUTAM, Elsevier, IUTAM-ABCM Symposium on Laminar Turbulent Transition, 14: 36-44
  - Perez J M, Paredes P & Theofilis V (2015) *Stability analysis of shock-wave dominated flow over a transonic bump*, Procedia IUTAM, Elsevier, IUTAM-ABCM Symposium on Laminar Turbulent Transition, 14:503-510

- Invited Presentations
  - Theofilis V (2018) *Global linear stability theory in aerospace applications*, 61st Ludwig Prandtl Memorial Lecture, 89th Annual Meeting of the GAMM - International Association of Applied Mathematics and Mechanics, March 19-23, 2018 Munich, Germany
  - Levin D, Tumuklu O, Theofilis V (2018) *Hyperonic flows at moderate Reynolds numbers.* 31st International Symposium on Rarefied Gas Dynamics, July 23-27, 2018, Glasgow, UK
  - Theofilis V (2018) *Global linear stability theory in aerospace applications.* 13th ERCOFTAC SIG 33 Workshop, Progress in Transition Modeling and Control, March 6-8, 2018, Paraty, Brazil
  - Theofilis V (2017) *An overview of global stability analysis: highlights, a closure and new frontiers.* 70th Annual Meeting of the APS Division of Fluid Dynamics, November 19-21, Denver, Colorado, USA
  - Theofilis V (2016) *Flow and flow instability around complex geometries at supersonic and hypersonic speeds*, 16th Brazilian Congress of Thermal Sciences and Engineering (ENCIT), December 7-10, Vitoria, Brazil
  - Theofilis V, Pérez JM (2016) *Global stability analysis past the solution of multidimensional EVP and SVD problems*, AIAA Discussion Group Modal Decomposition Methods for Aerodynamic Flows, Washington DC

- Presentations

  2018
  - Theofilis V (2018) *Global linear stability theory in aerospace applications*, Window on Science visit to AFRL, July 2018, Dayton, OH
  - Tumuklu O, Levin DA, Theofilis V (2018) *Development of New Techniques for Studying Unsteady Behavior in Hypersonic Boundary Layer Interactions*, 2018 Fluid Dynamics Conference, Atlanta, GA, AIAA Pap. 2018-3709
  - Tumuklu O, Levin DA, Theofilis V (2018) *Effects of Reynolds Number on Laminar Boundary Layer Shock-Interaction Hypersonic Flows on a Double Cone*, Fluid Dynamics Conference, Atlanta, GA, AIAA Pap. 2018-4032
  - Quintanilha Jr, HRDA, Kataras PB, Theofilis V, Hanifi A (2018) *Nonmodal stability analysis of the HIFiRE-5 elliptic cone model flow in different flight altitudes*, 58th Israel Annual Conference on Aerospace Sciences, March 2018, Tel Aviv and Haifa, Israel
  - Quintanilha Jr HRDA, Alves LS (2018) *On the existence of multiple self-excitation frequencies in the absolute instability of interacting mixing-layers and wakes*, 31st Congress of the International Council of the Aeronautical Sciences, September 2018, Belo Horizonte, Brazil

2017

- Quintanilha Jr HRDA, Santos R, Alves LS, Theofilis V (2017) *Distributed Solution of Global Eigenvalue Problems on Large Clusters*, 23rd AIAA Computational Fluid Dynamics Conference, Denver, CO
- Tumuklu O, Perez JM, Levin D, Theofilis V (2017) *On Linear Stability Analyses of Hypersonic Laminar Separated Flows in a DSMC Framework. Part I: Base Flow Computations in a Double Cone and a Tick Model*, 57th Israel Annual Conference on Aerospace Sciences, March 2017, Tel Aviv and Haifa, Israel
- Tumuklu O, Perez JM, Theofilis V, Levin D (2017) *On Linear Stability Analyses of Hypersonic Laminar Separated Flows in a DSMC Framework. Part II Residuals Algorithm and the Least Damped Global Modes*, 57th Israel Annual Conference on Aerospace Sciences, March 2017, Tel Aviv and Haifa, Israel

2016

- Quintanilha Jr HRDA, Alves LS (2016) *Linear Stability Analysis of Incompressible Mixing Layer Using Boundary Layer Theory*, 16th Brazilian Congress of Thermal Sciences and Engineering (ENCIT), December 7-10, Vitoria, Brazil.

Collaborations

- On account of the affinity of the research topic of the grant, the PI's group continued its participation in the NATO STO AVT-240 & RTG-082: Hypersonic Boundary-Layer Transition Prediction
- Dr. H. Reed, Dr. R. Bowersox (Texas A & M)

  Interactions regarding sharing numerical and experimental data produced at Texas A& M, aiming to perform non-modal (transient growth) analyses
- Dr. D. S. Henningson and Dr. A. Hanifi (KTH Stockholm)

  Joint work in preparation on nonlinear PSE-3D development

Visits / Student Exchanges

- Dr. P. Martin (and her graduate student, Ms. Clara Helm) visited:
  - V. Theofilis and J. M. Pérez at Univ. Politécnica de Madrid, August 1 – 15, 2016
- Dr. J. M. Pérez visited:
  - V. Theofilis at U. Liverpool, UK: Sept. 23 – 25, 2016

Honors and Awards

- Dr. V. Theofilis
  - 61st Ludwig Prandtl Memorial Lecture, 2018
  - Associate Fellow AIAA, 2010

Chapter 1

Introduction

1.1 Modal and non-modal linear global instability analysis of supersonic and hypersonic flows

Laminar-turbulent transition research has traditionally sought to identify exponentially amplifying small-amplitude perturbations that potentially lead a laminar flow through linear instability mechanisms to breakdown and turbulence. This so-called modal linear instability scenario (Lin 1955) can explain classic laminar flow instability mechanisms, such as Tollmien-Schlichting waves and crossflow modes in boundary layers, but has also led to spectacular failures, such as the prediction of linear stability at all Reynolds numbers in circular pipe flow, or more recently in one of the first applications of global linear theory to the rectangular duct (Tatsumi and Yoshimura 1990). Mathematical feasibility and computing expediency resulted in the vast majority of modal analysis performed in the last century to focus on one-dimensional base flows, such as Poiseuille flow in a plane channel or the Blasius boundary layer and its compressible counterpart (Hanifi et al. 1996a). Work in the hypersonic boundary layer has been reviewed by Schneider (2004), who discussed the findings of local analysis, obtained by solution of the compressible analogue of the Orr-Sommerfeld equation, as well as those obtained by the Parabolised Stability Equations applied to weakly-nonparallel boundary layer flows. The more recent work of Fedorov (2011) is also confined within local analyses but clarifies the misconceptions that have arisen in compressible boundary layer stability regarding the (Mack) mode terminology introduced in the classic work of Mack (1969, 1984).

Modal analysis of basic flows described by one-dimensional profiles has been extended in the last two decades by the introduction of global linear instability theory, reviewed by Theofilis (2003). Riding on the crest of ever increasing computing power and a wider availability of open-source libraries for large-scale linear algebra computations, the scope of global instability research has broadened substantially in the past decade. Numerical methods that have enabled linear modal global instability analysis have matured in both of the two major flavours of this analysis: matrix-forming and time-stepping. This has permitted obtaining novel global instability results in a series of configurations that were previously inaccessible to either of local analysis or PSE: corner and backstep geometries as well as lid-driven and open cavities have been analyzed, as have been pipe flows with geometric constrictions, the flowfield around entire airfoils and low-pressure turbine cascades, all within a spanwise homogeneous flow approximation and a BiGlobal linear modal analysis framework. More recently, flows that are fully inhomogeneous in all three spatial dimensions have also been analyzed with respect to their potential to amplify small-amplitude three-dimensional perturbations: an ellipsoid at an angle of attack, jet flow through an orifice into a crossflow, flow around a staked cylinder or that in the classic three-dimensional lid-driven cavity are examples of application of the so-called TriGlobal linear modal instability analysis. Between the two classes of spanwise homogeneous and fully inhomogeneous three-dimensional flows, PSE3D deals with global instability analysis of flows which depend strongly on two and weakly on the third spatial direction. Boundary layer flow in the wake of an isolated roughness element of size comparable with the local boundary layer thickness in supersonic (De Tullio et al. 2013) and

hypersonic (Paredes et al. 2016a) flow has served as a demonstrator of the capacity of the PSE3D methodology to recover results otherwise only accessible to spatial direct numerical simulation at orders of magnitude higher level of computational effort. Nevertheless, on the one hand owing to the cost of solving the global linear instability equations in compressible flow and on the other hand due to the wide availability of open source direct numerical simulation codes for the solution of the incompressible equations of motion, the vast majority of global linear instability analysis work performed to-date has been in the incompressible regime.

At the same time as global linear theory extended the classic (modal) linear stability theory, a second path leading laminar flow through transition to turbulence has been recognized, namely transient growth caused by non-modal, algebraically growing linear disturbances (Trefethen et al. 1993, Schmid and Henningson 2001, Tumin and Reshotko 2001, Tempelmann et al. 2010). The non-modal analysis of compressible boundary layer flow has been first performed by (Hanifi et al. 1996a). In incompressible boundary layer flows, the laminar-turbulent transition scenario based on short-time (transient) algebraic growth of non-modal perturbations, typically streamwise aligned streaks, is well-known to constitute a path to transition alternative to the modal scenario based on exponential amplification of Tollmien-Schlichting waves and crossflow eigenmodes at subcritical Reynolds numbers. Under certain subcritical flow conditions, the transient growth scenario can altogether bypass that based on modal exponential amplification, rendering the modal decay irrelevant. In other situations, optimal perturbations growing algebraically at early times transform into modal perturbations that eventually grow. Non-modal perturbations growing algebraically are known to modify the underlying base state, which can then undergo laminar-turbulent flow transition on account of exponentially amplifying secondary disturbances. The currently accepted "updated roadmap to transition", due to Morkovin (1994) summarizes these possible paths leading laminar flow to turbulence.

The vast majority of transient growth work has to-date also been performed in a local analysis framework, considering flows the basic state of which is homogeneous in two spatial directions, although global linear theory also permits monitoring non-modal disturbances. The first work that combined non-modal and global linear instability analysis in the incompressible regime has discovered strong transient growth analysis in a Low Pressure Turbine (LPT) cascade (Abdessemed et al. 2009). A number of non-modal analyses of separated flows followed in the literature and demonstrated the potential of flow separation to sustain large levels of transient growth, besides the well-known modal scenarios following the Kelvin-Helmholtz instability of traveling perturbations entering the separation zone, or the global stationary three-dimensional mechanism discovered by Theofilis et al. (2000). Recent work has considered the stability of flow over stalled airfoils and has also demonstrated the potential of this flow to sustain strong transient growth non-modal instability, besides the previously known traveling KH and stationary global mode paths to transition (He et al. 2017).

Comparatively less non-modal instability analyses have been performed in compressible flow. Following work in the incompressible flat plate boundary layer (Reddy and Henningson 1993, Corbett and Bottaro 2001a, Tempelmann et al. 2010) transient growth analyses of the compressible boundary layer demonstrated the potential of this flow to sustain algebraic growth of streamwise aligned perturbations at conditions subcritical to exponential amplification of Tollmien-Schlichting or crossflow disturbances (Hanifi et al. 1996a, Tumin and Reshotko 2003, Zuccher et al. 2006, 2007, Tempelmann et al. 2012). Finally, very recently, Paredes et al. (2017a) and Paredes et al. (2018) studied the blunt-body paradox and transient growth to leeward transition over a hypersonic spherical fore-body. They show the importance of the choice of an appropriate energy norm and highlighted the need to further investigate the optimal-growth criterion underlying the Reshotko-Tumin correlation.

1.2 The HIFiRE program

The HIFiRE hypersonic flight test program lead by the Air Force Research Laboratory (AFRL) and the Australian Defence Science and Technology Organization (DSTO) (Dolvin 2008) aimed to demonstrate fundamental technologies critical to design of next generation aerospace systems. The first experiment, HIFiRE-1, used a 7° AoA cylinder cone to obtain in-flight transitional and turbulent boundary layer heating data on axisymmetric configurations. The design of this experiment, the associated pre-flight effort and actual flight data as well as transitional analysis can be found in Kimmel et al. (2007), Kimmel (2008), Kimmel et al. (2011), Adamczak et al. (2011), Stanfield et al. (2012) and Fei et al. (2011).

HIFiRE-5 was the the follow-on flight test program, designed to provide transition data in the boundary-layer of a three-dimensional geometry. Figure 1.2 shows the HIFiRE-5 configuration consisting of an S-30 first stage and Improved Orion second stage, as well as the payload and the transition section. The S-30 and the Orion stack boost the test geometry to approximately 270km with a peak Mach number of 7.5. The geometry consists of a blunt-nosed elliptic cone of 2:1 aspect ratio and 0.86m in length.The nose tip cross-section in the minor-axis (centreline) describes a 2.5mm radius circular arc, tangent to the cone ray describing the minor axis, and retains a 2:1 elliptical cross-section to the tip. Kimmel et al. (2010) presented the flight vehicle design with more details. The elliptic cone geometry was chosen based on past ground test and CFD (Choudhari et al. 2009). Several authors investigated hypersonic transition on this geometry (Kimmel and Poggie 1997b,a, Kimmel et al. 1999, Schmisseur et al. 1998, Holden 1998, Schmisseur et al. 1999, Lyttle and Reed 1995). A 2:1 aspect ration of the ellipse is chosen since it presents significant crossflow and second-mode instabilities and they are expected to be the dominant instability mechanism on hypersonic vehicles.

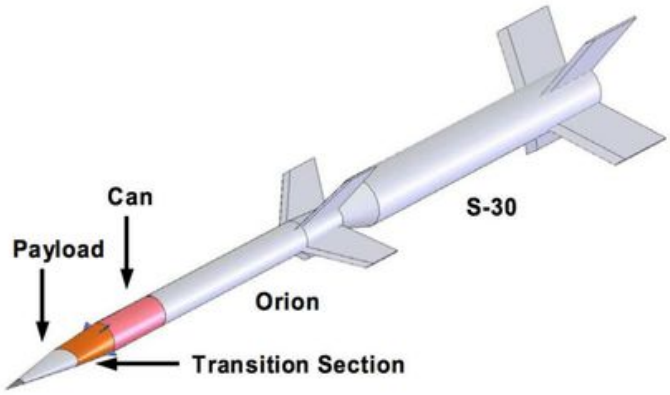

Figure 1.1: HIFiRE-5 stack (Kimmel et al. 2010).

Choudhari et al. (2009), Paredes and Theofilis (2015) and Paredes et al. (2016a), studied the modal stability over the HIFiRE-5 test geometry. Four classes of linear disturbances were found: shear-layer instability due to the centreline, second Mack modes at the attachment-line and oblique second modes and cross-flow instabilities in the boundary layer between the centreline and attachment-line. Experiments were performed in a quiet hypersonic wind tunnel by Borg et al. (2012). They found that the unperturbed stationary wavelength is damped out with some roughness spacings, exciting wavelengths that were stable in the unperturbed boundary layer.

The interaction between modal and non-modal stability was studied by Paredes et al. (2017b) for the HIFiRE-1 flight experiment geometry. The base flow containing the streaks from the transient growth was analyzed through a modal stability analysis, confirming previous findings that the mean-flow distortion of the nonlinear streak perturbation reduces the amplification rates of the Mack-mode instability. They also demonstrated that the spanwise varying component of this streak can produce a larger effect on the Mack-mode amplification itself.

The present work has applied the world-first non-modal (transient-growth) instability analysis of HIFiRE-5 elliptic cone geometry to interrogate the flow field with respect to its potential to sustain transient growth, as well as clarify the instability mechanism giving rise to streamwise aligned structures visible on the elliptic cone at both supersonic and hypersonic speeds, both in the laboratory and in flight testing. In a parallel development, it was deemed interesting to extend the transient growth code functionality by including linear resolvent analysis, since the latter permits to predict the linear response of the flow to external harmonic forcing. In other words, the originally planned TG analysis, which is underway, predicts the intrinsic instability behavior of the elliptic cone at the given conditions analyzed, while the resolvent analysis extends the TG work in predicting the response of the same flow to a wide variety of externally imposed forcing functions. Linear resolvent analysis incorporates the

solution of the unforced initial value problem (IVP), which is identical with the above mentioned transient growth analysis. The costly element in the IVP solution is the inversion of the operator. In order to perform efficient inversion of the global matrix, it has been decided to work during subsequent years of the present effort on the development of a massively parallel solution of the eigenvalue and singular value problems.

The HIFiRE-5 geometry was modeled by a blunt-nosed elliptic cone of 2:1 ellipticity and 0.86m in length. Flight flow conditions were calculated for a Mach 7 at altitude of 33km. The free-stream velocity is $U_\infty = 2452.17$ m/s, the temperature of reference is $T_\infty = 230.97$ K and the unit Reynolds number is Re'=1.89x10^6 m^{-1}. The steady laminar flow solution is the same used by Paredes et al. (2016a) and has been calculated using the US3D non-equilibrium solver with shock capturing algorithm. Chemistry interactions were not yet considered at the moment due to the relatively low hypersonic Mach number. A more detailed description of the base flow computation can be found in Gosse et al. (2010, 2013).

Figure 1.2 shows contours of the base flow streamwise velocity and temperature, respectively, at position x=0.62 m. The two-dimensional profile at this location is used to compute the BiGlobal stability analysis. The three-dimensional geometry of the elliptic cone produces pressure gradients in the spanwise direction, inducing the formation of crossflow velocity components.The boundary layer near the surface is deflected from the leading-edge towards the centreline producing a lift-up of low momentum boundary layer fluid, generating a mushroom-like structure.

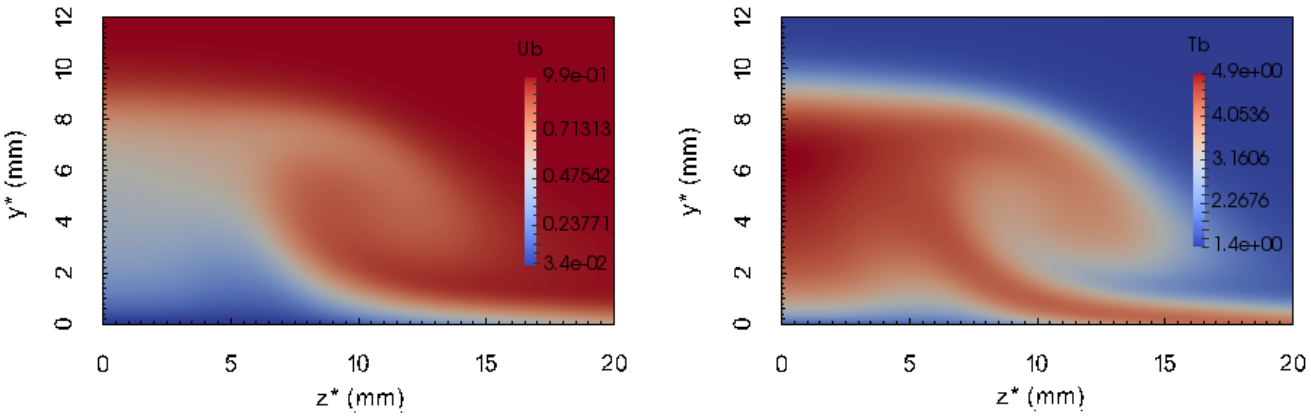

Figure 1.2: Streamwise velocity and temperature base flow calculated by Gosse et al. (2010) using US3D solver, extracted at the axial location $x = 0.62m$

Chapter 2

Linear Global Instability Analysis

2.1 The linearized Navier-Stokes equations (LNSE)

The governing equations of the evolution of infinitesimal amplitude disturbances study here starts from the compressible Navier-Stokes equations. In this part of the analysis, Cartesian coordinate system will be employed since the primary objective is presenting the idea of the analysis itself. In the general form:

$$\frac{\partial \rho}{\partial t} + \nabla.(\rho \mathbf{V}) = \mathbf{0}, \tag{2.1}$$

$$\frac{\partial (\rho \mathbf{V})}{\partial t} + \nabla.(\rho \mathbf{V}\mathbf{V}) = -\nabla p + \frac{1}{Re}\nabla.\sigma \tag{2.2}$$

$$\frac{\partial p}{\partial t} + \mathbf{V}.\nabla p + \gamma p \nabla.\mathbf{V} = \frac{1}{RePrM^2}\nabla.(k\nabla T) + \frac{(\gamma-1)}{Re}\frac{1}{2}(\nabla \mathbf{V} + \nabla \mathbf{V}) : \sigma \tag{2.3}$$

$$p = \frac{\rho T}{\gamma M a^2} \tag{2.4}$$

where,

$$\sigma = [\mu(\nabla \mathbf{V} + (\nabla \mathbf{V})^T)] + \nabla[\lambda(\nabla.\mathbf{V})]$$

is the viscous stress tensor, $\mathbf{V} = \{\mathrm{u,v,w}\}^T$ is the velocity vector, ρ is the density, p is the pressure, T is the temperature, μ is the first coefficient of viscosity, λ is the second coefficient of viscosity and k is the thermal conductivity. The equation of state of perfect gases with constant $\gamma = 1.4$ is also presented. The Prandtl number Pr is chosen as constant and equals 0.72 and Stokes' hypothesis has been applied to calculate λ.
The linearized Navier-Stokes equations (LNSE) result from the substitution of a linear decomposition of all flow quantities, $\mathbf{q} = (\rho, \mathbf{u_1}, \mathbf{u_2}, \mathbf{u_3}, \mathbf{p})^{\mathbf{T}}$ into a steady laminar base or mean flow and a small amplitude disturbance, according to

$$\mathbf{q}(\mathbf{x}, t) = \bar{\mathbf{q}}(\mathbf{x}) + \epsilon \tilde{\mathbf{q}}(\mathbf{x}, t), \qquad with \quad \epsilon \ll 1. \tag{2.5}$$

The $O(1)$ resulting equations are those governing the base state and are satisfied by construction, the $O(\epsilon^2)$ equations are neglected, on account of smallness of the perturbation amplitudes, while the $O(\epsilon)$ equations are the LNSE, that need to be solved, either as an eigenvalue problem (modal analysis) or as an initial value problem (non-modal analysis).

2.2 Local and global linear stability analysis

The decomposition (2.5) is valid irrespectively of the spatial dimensionality of the base flow and small perturbations. The classification of Table 2.1 shows the decomposition in a local and a global linear stability analysis context.

	Denomination	Base Flow assumptions		Amplitude function	Phase function
	TriGlobal	—	$\overline{\mathbf{q}}(x,y,z)$	$\hat{\mathbf{q}}(x,y,z)$	ωt
Global	PSE-3D	$\partial_x\overline{\mathbf{q}} \ll \partial_y\overline{\mathbf{q}}$	$\overline{\mathbf{q}}(X,y,z)$	$\hat{\mathbf{q}}(X,y,z)$	$\int_0^X \alpha(\xi)d\xi - \omega$t
	BiGlobal	$\partial_x\overline{\mathbf{q}} = 0$	$\overline{\mathbf{q}}(y,z)$	$\hat{\mathbf{q}}(y,z)$	$\alpha x - \omega$t
Nonlocal	PSE	$\partial_x\overline{\mathbf{q}} \ll \partial_y\overline{\mathbf{q}}; \partial_z\overline{\mathbf{q}} = 0$	$\overline{\mathbf{q}}(X,y)$	$\hat{\mathbf{q}}(X,y)$	$\int_0^X \alpha(\xi)d\xi + \beta z - \omega$t
Local	OSE	$\partial_x\overline{\mathbf{q}} = \partial_z\overline{\mathbf{q}} = 0$	$\overline{\mathbf{q}}(y)$	$\hat{\mathbf{q}}(y)$	$\alpha x + \beta z - \omega$t

Table 2.1: Classification of linear stability theories

2.2.1 Local instability

In local and nonlocal analysis, as defined in Table 2.1, only one spatial direction is taken to be inhomogeneous, in both the base flow and the amplitude functions. Parallel shear flows (Schmid and Henningson 2001, Schmidt and Rist 2011) can be analyzed using this concept, in which the velocity field comprises a streamwise and a spanwise component, both of which are functions of the transverse spatial direction only, while the transverse/wall-normal base flow velocity component is neglected. In axisymmetric geometries, the base flow and amplitude functions dependent only on the radial coordinate. Applying separation of variables, the two homogeneous directions can be decomposed in the Fourier space and the linearized equations of motion may be re-written as a system of linear ordinary differential equations, as discussed by Mack (1984), one form of which is the celebrated Orr-Sommerfeld equations (OSE).

Mathematically, assuming x and z as the homogeneous spatial directions, such that the base flow is only dependent on the y spatial coordinate, modal perturbations are of the form

$$\tilde{\mathbf{q}}(x,y,z,t) = \hat{\mathbf{q}}(y)\ exp[i\ (\alpha x + \beta z - \omega t)], \tag{2.6}$$

where $L_x = \frac{2\pi}{\alpha}$ and $L_z = \frac{2\pi}{\beta}$ are periodicity lengths along the homogeneous spatial directions, while α and β are the corresponding wavenumbers. Substituting this Ansatz into the compressible LNSE leads to the one-dimensional eigenvalue problem presented and solved by Mack (1969, 1984). In the incompressible limit, the resulting system, after the substitution of the Ansatz (2.6), can be reduced into two coupled ordinary differential equations, by eliminating the pressure variable and using the definition of normal vorticity,

$$\begin{aligned}[(-i\omega + i\alpha\bar{u})(D_{yy}^2 - k^2) - i\alpha\bar{u}_{yy} - \frac{1}{Re}(D_{yy}^2 - k^2)]\hat{v} = 0 \\ [(-i\omega + i\alpha\bar{u}) - \frac{1}{Re}(D_{yy}^2 - k^2)]\hat{\eta} = -i\beta\bar{u}_y\bar{v},\end{aligned} \tag{2.7}$$

where $k^2 = \alpha^2 + \beta^2$. The first of these is the Orr-Sommerfeld equation, while the second is known as the Squire equation; they have been used to analyze linear modal instability of shear flows since the beginning of the XX century (Drazin et al. 1982),(Lin 1955). Despite the simplicity of these equations, they provide the exact eigenmodes

of strictly parallel flows and are reasonable approximations for quasi-parallel, slowly diverging flows, such as the boundary layer or a free shear layer. The $Re \to \infty$ limit of the Orr-Sommerfeld was derived by Lord Rayleigh and describes inviscid instability of flows with inflectional base flow profiles.

Linear perturbations may be taken grow in time or space; the respective temporal analysis framework is assuming real wavenumber parameters and solves for a complex eigenvalue ω in the temporal *linear* eigenvalue problem

$$\mathcal{A}\hat{\mathbf{q}} = \omega\mathcal{B}\hat{\mathbf{q}}, \tag{2.8}$$

while the spatial EVP assumes a real perturbation frequency ω and solves the *nonlinear* eigenvalue problem

$$\mathcal{A}\hat{\mathbf{q}} = \sum_{k=1}^{2}\alpha^k\mathcal{B}_k\hat{\mathbf{q}}, \tag{2.9}$$

for a complex eigenvalue α. Equation (2.9) can be converted into a linear EVP using a companion matrix method (Bridges and Morris 1984a, Theofilis 1995, Heeg and Geurts 1997).

2.2.2 BiGlobal instability

If the base flow is now assumed to be dependent on two spatial directions, say x and y, BiGlobal linear instability theory can be applied; the reader is referred to the review of Theofilis (2003) for more details. A harmonic dependence of the small-amplitude perturbations is assumed along the homogeneous spatial direction, z, with periodicity length $L_z = 2\pi/\beta$, permitting further expansion of (2.5) using

$$\tilde{\mathbf{q}}(x, y, z, t) = \hat{\mathbf{q}}(y, z) = \exp[i(\beta z - \omega t)]. \tag{2.10}$$

Substituting this above Ansatz in the compressible LNSE, the resulting components of the temporal operators $\mathcal{A}$ and $\mathcal{B}$ are

$$\begin{pmatrix} \mathcal{A}_{11} & \mathcal{A}_{12} & \mathcal{A}_{13} & \mathcal{A}_{14} & \mathcal{A}_{15} \\ \mathcal{A}_{21} & \mathcal{A}_{22} & \mathcal{A}_{23} & \mathcal{A}_{24} & \mathcal{A}_{25} \\ \mathcal{A}_{31} & \mathcal{A}_{32} & \mathcal{A}_{33} & \mathcal{A}_{34} & \mathcal{A}_{35} \\ \mathcal{A}_{41} & \mathcal{A}_{42} & \mathcal{A}_{43} & \mathcal{A}_{44} & \mathcal{A}_{45} \\ \mathcal{A}_{51} & \mathcal{A}_{52} & \mathcal{A}_{53} & \mathcal{A}_{54} & \mathcal{A}_{55} \end{pmatrix} \begin{pmatrix} \hat{u} \\ \hat{v} \\ \hat{w} \\ \hat{T} \\ \hat{p} \end{pmatrix} = \omega \begin{pmatrix} \mathcal{B}_{11} & 0 & 0 & 0 & 0 \\ 0 & \mathcal{B}_{22} & 0 & 0 & 0 \\ 0 & 0 & \mathcal{B}_{33} & 0 & 0 \\ 0 & 0 & 0 & 0 & \mathcal{B}_{45} \\ 0 & 0 & 0 & \mathcal{B}_{54} & \mathcal{B}_{55} \end{pmatrix} \begin{pmatrix} \hat{u} \\ \hat{v} \\ \hat{w} \\ \hat{T} \\ \hat{p} \end{pmatrix} \tag{2.11}$$

The explicit form of these operators can be found in Appendix B. Following the same reasoning from the local analysis, $\beta = \frac{2\pi}{L_z}$ and the sought complex eigenvalue is ω. Equation (2.11) was first solved for the elliptic cone in a global modal stability analysis context by Choudhari et al. (2009) and subsequently by Paredes et al. (2016b).

2.3 Instability analysis in generalized coordinates

The three-dimensional nature of the elliptic cone necessitates solution of the global linear instability problem in a general three-dimensional geometry of arbitrary complexity. In the following sections, the general equations are presented, alongside the analytic transformation used to solve these for the elliptic cone geometry.

2.3.1 Coordinate transformation

The generalized three-dimensional coordinate system (ξ, η, ζ) can be related to the Cartesian coordinates (x,y,z) by the transformation

$$\xi = \xi(x, y, z), \qquad \eta = \eta(x, y, z), \qquad \zeta = \zeta(x, y, z) \tag{2.12}$$

To express the first order partial derivatives, the chain rule can be used

$$\frac{\partial}{\partial x} = \xi_x \frac{\partial}{\partial \xi} + \eta_x \frac{\partial}{\partial \eta} + \zeta_x \frac{\partial}{\partial \zeta}, \qquad \frac{\partial}{\partial y} = \xi_y \frac{\partial}{\partial \xi} + \eta_y \frac{\partial}{\partial \eta} + \zeta_y \frac{\partial}{\partial \zeta}, \qquad \frac{\partial}{\partial z} = \xi_z \frac{\partial}{\partial \xi} + \eta_z \frac{\partial}{\partial \eta} + \zeta_z \frac{\partial}{\partial \zeta} \tag{2.13}$$

The metrics appearing in these equations $(\xi_x, \xi_y, \xi_z, \eta_x, \eta_y, \eta_z, \zeta_x, \zeta_y, \zeta_z)$ can be obtained directly if an explicit expression for ξ, η and ζ is provided. If not, they are determined solving the system

$$\begin{pmatrix} \xi_x & \xi_y & \xi_z \\ \eta_x & \eta_y & \eta_z \\ \zeta_x & \zeta_y & \zeta_z \end{pmatrix} = \begin{pmatrix} x_\xi & x_\eta & x_\zeta \\ y_\xi & y_\eta & y_\zeta \\ z_\xi & z_\eta & z_\zeta \end{pmatrix}^{-1} = J \begin{pmatrix} y_\eta z_\zeta - y_\zeta z_\eta & -(x_\eta z_\zeta - x_\zeta z_\eta) & x_\eta y_\zeta - x_\zeta y_\eta \\ -(y_\xi z_\zeta - y_\zeta z_\xi) & x_\xi z_\zeta - x_\zeta z_\xi & -(x_\xi y_\zeta - x_\zeta y_\xi) \\ y_\xi z_\eta - y_\eta z_\xi & -(x_\xi z_\eta - x_\eta z_\xi) & x_\xi y_\eta - x_\eta y_\xi \end{pmatrix} \tag{2.14}$$

where J is the Jacobian of the transformation

$$J = \frac{\partial(\xi, \eta, \zeta)}{\partial(x, y, z)} = \frac{1}{\frac{\partial(x,y,z)}{\partial(\xi,\eta,\zeta)}} = \frac{1}{x_\xi(y_\eta z_\zeta - y_\zeta z_\eta) - x_\eta(y_\xi z_\zeta - y_\zeta z_\xi) + x_\zeta(y_\xi z_\eta - y_\eta z_\xi)}. \tag{2.15}$$

For cases where the transformation is the direct result of the grid generation scheme, the metrics can be computed numerically. In the case of second order derivatives in terms of computational coordinate, the result from the system 2.14 can be derived in respect to the appropriated variable leading to the second derivative metric. Particularly, the derivative of ξ_x in respect to x is

$$\begin{aligned} \frac{\partial^2 \xi}{\partial x^2} = J\Bigg[&- \frac{\partial z}{\partial \eta}\left(\frac{\partial \eta}{\partial x}\frac{\partial^2 y}{\partial \eta \partial \zeta} + \frac{\partial \xi}{\partial x}\frac{\partial^2 y}{\partial \xi\, \partial \zeta} + \frac{\partial \zeta}{\partial x}\frac{\partial^2 y}{\partial \zeta^2}\right) + \frac{\partial y}{\partial \eta}\left(\frac{\partial \eta}{\partial x}\frac{\partial^2 z}{\partial \eta \partial \zeta} + \frac{\partial \xi}{\partial x}\frac{\partial^2 z}{\partial \xi\, \partial \zeta} + \frac{\partial \zeta}{\partial x}\frac{\partial^2 z}{\partial \zeta^2}\right) + \\ &\frac{\partial z}{\partial \zeta}\left(\frac{\partial \zeta}{\partial x}\frac{\partial^2 y}{\partial \eta \partial \zeta} + \frac{\partial \xi}{\partial x}\frac{\partial^2 y}{\partial \xi \partial \eta} + \frac{\partial \eta}{\partial x}\frac{\partial^2 y}{\partial \eta^2}\right) - \frac{\partial y}{\partial \zeta}\left(\frac{\partial \zeta}{\partial x}\frac{\partial^2 z}{\partial \eta \partial \zeta} + \frac{\partial \xi}{\partial x}\frac{\partial^2 z}{\partial \xi \partial \eta} + \frac{\partial \eta}{\partial x}\frac{\partial^2 z}{\partial \eta^2}\right)\Bigg] + \\ &\left(\frac{\partial y}{\partial \eta}\frac{\partial z}{\partial \zeta} - \frac{\partial y}{\partial \zeta}\frac{\partial z}{\partial \eta}\right)\left(\frac{\partial J}{\partial \zeta}\frac{\partial \zeta}{\partial x} + \frac{\partial J}{\partial \eta}\frac{\partial \eta}{\partial x} + \frac{\partial J}{\partial \xi}\frac{\partial \xi}{\partial x}\right). \end{aligned} \tag{2.16}$$

Applying the transformation (2.13) to the compressible Navier-Stokes equations leads to the compressible generalized Navier-Stokes equations, found in Appendix A. Once the Jacobian is provided (analytically or numerically) linear stability of flow around or through any complex geometry can be analyzed.

2.3.2 Elliptic confocal coordinates on the elliptic cone

The transformation from the physical coordinate system (x, y, z) to the computational coordinate system (ξ, η, ζ) is made using the follow orthogonal elliptic confocal transformation (Paredes et al. 2016b)

$$x = \xi, \qquad y = c\ \sinh(\eta)\sin(\zeta), \qquad z = c\ \cosh(\eta)\cos(\zeta) \tag{2.17}$$

where $c = 2/\sinh(\eta_0)$ sets the half angle of the cone minor-axis and η_0 is a parameter controlling the Aspect Ratio (AR) of the cone, $\eta_0 = \text{atanh}(1/\text{AR})$. With the above transformation, the Jacobian from equation (2.15) is then defined as:

$$J = \frac{2}{c^2\big(\cos(2\zeta) - \cosh(2\eta)\big)},$$

also known as the metric factor.

The linearized equations of motion addressed as either an eigenvalue or a singular value problem are obtained from substitution of the elliptic confocal transformation into the compressible continuity, Navier-Stokes and energy equations (2.1-2.3). To this end the equations of motion are written in a general three-dimensional coordinate system, as shown in Appendix A. Linearizing and retaining the $O(\epsilon)$ quantities, the equations solved to determine modal and non-modal instability on the elliptic cone, shown in Appendix C, result.

Chapter 3

Transient Growth in Non-normal Systems

3.1 Modal vs. non-modal linear instability

For over a century, modal analysis, which interrogates exponential growth or decay of an infinitesimal flow perturbation, has been the workhorse of linear flow instability analyses. In this, so-called *modal* context, the objective is identification of a minimum of a critical parameter, such as the flow Reynolds number in a boundary layer, rotation rate in Taylor-Couette flow, or Rayleigh number in the classic Rayleigh-Bernard convection, beyond which a specific initial small-amplitude perturbation grows exponentially in time and/or space. This minimum value of the critical parameter is calculated via an eigenvalue decomposition of the linearized operator which describes time- or space-evolution of small-amplitude perturbations superposed upon a given flow, and the associated eigenvalues dictate the behavior of the perturbation, namely exponentially growing or decaying flow instabilities at asymptotically large times. This modal linear theory is shown to deliver accurate predictions in a number of flow paradigms, such as the Rayleigh-Bernard convection, where a critical Rayleigh number of $Ra = 1708$ is predicted, while experiments show $Ra = 1710$, thus confirming the ability of modal analysis to correctly predict flow instability physics. However, modal linear theory has also produced glaring failures, starting with the famous Reynolds (1883) experiment, where the theoretically predicted flow stability at all Reynolds numbers starkly contrasts with experimental reality which delivers transition to turbulent flow at Reynolds numbers $Re = O(2000)$. Incomplete predictions are also delivered by solution of the famous Orr-Sommerfeld equation for plane channel flow, where again experimental evidence of transition at Reynolds number $Re = O(1500)$ cannot be matched by the theoretical prediction of modal analysis, $Re = 5772$.

These discrepancies have been attributed to the linearization of the governing equations within a modal context, i.e. one that explicitly introduces a harmonic time-dependence of the linear perturbations and monitors their development at large times. On the other hand, the non-linear terms in the Navies-Stokes equation conserve energy (Waleffe 1995, Henningson 1996) and during transition a substantial *algebraic*, as opposed to exponential, increase in kinetic energy of linear perturbations may be observed in a number of systems. In other words, amplification of linear perturbations may be observed that cannot be accounted for by eigenvalue analysis. Linear stability analysis consists of a two-step procedure, namely linearization of the governing equations and diagonalization. Intense research over the past two decades has shown that most of the shortcomings as well as the failures of the linear modal stability theory arise in the second step, namely the diagonalization of the operator. The explanation of the erroneous predictions of modal analysis lies in the fact that the operator describing the linearized Navier-Stokes equations is non-normal, several of its eigenvectors are nearly parallel and the condition number of the matrix that discretises this operator is (extremely) large. Amplification of infinitesimal disturbances is possible even if the eigenvalues of a linear system are found to be stable, the reason being that, when the eigenvectors of the system are

not orthogonal to each other, growth of their resultant magnitude can occur over short time horizons, even though the eigenvalues are stable and the eigenvectors are decaying in time. Operators exhibiting a set of non-orthogonal eigenvectors are referred to as non-normal operators (Trefethen et al. 1993, Trefethen 1997, Schmid and Henningson 2001) and the associated short-time horizon algebraic growth is referred to as *non-modal* or *transient growth*.

3.2 Geometric interpretation of transient growth

Before addressing specific forms of the equations of fluid flow motion, the above ideas are exemplified by a generic Initial Value Problem (IVP)

$$\partial_t \hat{\mathbf{q}} = \mathcal{L}(\bar{\mathbf{q}})\hat{\mathbf{q}}, \tag{3.1}$$

where $\bar{\mathbf{q}}$ is the state whose linear perturbations $\hat{\mathbf{q}}$ are sought. In a fluid context the operator $\mathcal{L}$ would contain the base flow and its spatial derivatives in the Linearized Navier-Stokes Equations (LNSE) in which the Reynolds, Re, and Mach, Ma, numbers would appear as parameters. However, the discussion at this point is broader and the IVP may come from a number of fields in physics (Trefethen 1992). The exact solution of the IVP is written with the aid of the matrix exponential (Moller and Van Loan 2003)

$$\hat{\mathbf{q}}(t) = \hat{\mathbf{q}}(0)e^{\mathcal{A}t}, \tag{3.2}$$

where matrix $\mathcal{A}$ represents the numerical discretization of the linear operator $\mathcal{L}$. If this matrix were normal, its eigenvalue spectrum could be used to simplify this expression. However, $\mathcal{A}$ of the LNSE is (highly) non-normal leading to a non-trivial behavior at early times, which arises on account of the near-parallel nature of certain eigenvectors (Schmid and Henningson 2001) in the eigenspectrum.

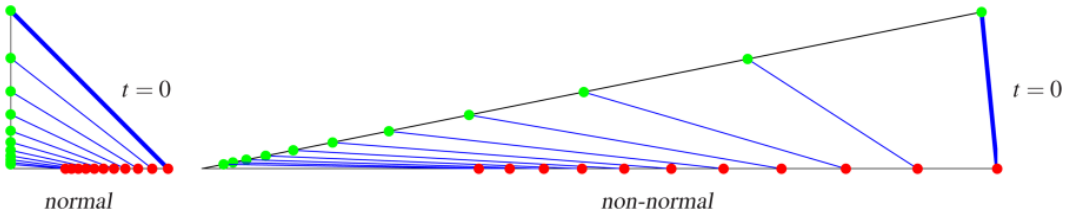

Figure 3.1: Geometric interpretation of transient growth (Schmid and Brandt 2014)

A simple example shown in Fig.3.1 illustrates the transient growth phenomenon graphically. On the left hand side of this plot the eigenvectors are normal to each other. As a result, when the eigenvalues are decaying, the eigenvectors are also decaying. On the other side, the eigenvectors are non-normal to each other. Thus, although the eigenvalues are damped, it can be noticed that the eigenvectors transiently grow in size before their ultimate decay. This geometric interpretation helps clarify a central idea in transient growth analysis, namely that *in a short time-horizon (time is a parameter in the analysis) linear superposition of decaying non-orthogonal eigenvectors can indeed produce growth in the norm of a disturbance.* The decaying nature of the individual eigenvectors will only manifest itself at asymptotically large times.

3.3 A quantitative example of transient growth (Trefethen 1992)

A further example demonstrates transient growth quantitatively. Take the matrices

$$A = \begin{bmatrix} -1 & 1 \\ 1 & -10 \end{bmatrix}, \quad A = \begin{bmatrix} -1 & 10 \\ 0 & -2 \end{bmatrix}, \quad \text{and} \quad A = \begin{bmatrix} 0.2 & 0.1 \\ 0 & -0.2 \end{bmatrix}$$

and solve the Initial Value Problems (IVP)

$$\partial_t \hat{\mathbf{q}} = \mathrm{A}\hat{\mathbf{q}} \quad \text{with A normal, 2 -ve EVs,} \tag{3.3}$$

$$\partial_t \hat{\mathbf{q}} = \mathrm{A}\hat{\mathbf{q}} \quad \text{with A non-normal, 2 -ve EVs,} \tag{3.4}$$

$$\partial_t \hat{\mathbf{q}} = \mathrm{A}\hat{\mathbf{q}} \quad \text{with A non-normal, 1 +ve / 1 -ve EV.} \tag{3.5}$$

The respective eigenvalues are $\Lambda\{A\} = \{-1, -1\}$, $\Lambda\{A\} = \{-2, -1\}$ and $\Lambda\{A\} = \{-0.2, 0.2\}$.
The solutions of (3.3-3.5) with $\hat{q}(0) = 1$ are shown in Figure 3.2. One notes the expected behavior of A and A. The negative eigenvalues of A are reflected in the monotonic decay of the signal (left figure) and in the constant slope of the decaying straight line (right figure). Analogously for A, the positive eigenvalue determines the monotonic growth of the respective signal, as seen in both linear and semi-logarithmic scales. By contrast, the signal corresponding to A, which only has negative eigenvalues and should also display monotonic decay in time, can clearly be seen to grow at early times, before ultimately decaying as the eigenvalues would predict. This *transient* growth at early times is due to the non-normality of A, which contrasts with the normal behavior of the matrices A and A.

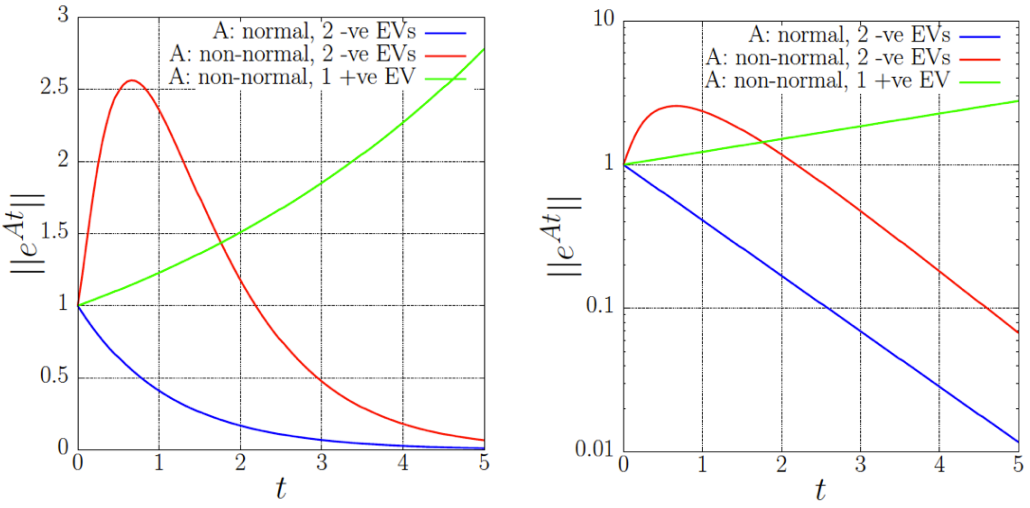

Figure 3.2: Solutions of (3.3-3.5) in linear (left) and semi-logarithmic (right) scales

The behavior exhibited by A is common to non-normal matrices, such as those resulting from spatial discretization of the linearized Navier-Stokes equations (LNSE). Here too, rather than focusing on the eigenvalue problem (EVP) alone, one needs to solve both of the EVP and the initial value problem (IVP) in order for complete predictions on the *linear* instability behavior to be obtained. The (matrix exponential) solution may exhibit transient growth (at short times), even if the eigenvalue predicts decay in (asymptotically large) time. Of course, the EVP predictions are identical with those yielded by the asymptotically large time, $t \to \infty$ in the solution of the IVP. This behavior is absent in normal matrices (here the "blue" and "green" example matrices) in which the eigenvalues completely determine the dynamic behavior of the system. From a numerical analysis point of view, the growth observed transiently is intimately linked with, and is actually proportional to, the condition number of the discretized matrix in question.
A new concept, that of $\epsilon-$*pseudospectrum*, which extends the well-known eigenspectrum, is necessary to quantify the transient behavior of non-normal matrices. In order for quantitative predictions to be made, first the *resolvent* of $\mathcal{A}$ is defined as

$$(zI - \mathcal{A})^{-1}, \quad z \in \mathbb{C}. \tag{3.6}$$

The resolvent becomes infinite when z is an eigenvalue of $\mathcal{A}$. With the help of the resolvent, the $\epsilon-$*pseudospectrum* of $\mathcal{A}$, is defined as

$$\Lambda_\epsilon(\mathcal{A}) \equiv \left\{z \in \mathbb{C} : ||(zI-\mathcal{A})^{-1}|| \geq \epsilon^{-1}\right\} \quad (3.7)$$
$$\equiv \left\{z \in \mathbb{C} : \sigma_{\min}(zI-\mathcal{A})^{-1} \leq \epsilon\right\} \quad (3.8)$$
$$\equiv \{z \in \mathbb{C} : z \text{ is an eigenvalue of } \mathcal{A}+\mathcal{E}, \text{ for some } \mathcal{E} \text{ with } ||\mathcal{E}|| \leq \epsilon\} \quad (3.9)$$

Here $||.||$ is the L2-norm of a vector and σ is a singular value of a matrix. Any of the three definitions,

- resolvent norm,
- minimum singular value of the resolvent, or
- eigenspectrum of the randomly perturbed matrix

may be used to compute the ϵ-pseudospectrum. When employing the matrix-perturbations approach, transient growth is expected to occur in the non-sharply defined parts of the eigenspectrum, as a consequence of the superposition of the corresponding non-orthogonal eigenvectors. When solving the matrix exponential, time becomes a parameter; as such transient growth theory permits analysis of time-dependent flows. However, a reasonably large time-window needs to be examined, in order to cover both the early-time and the asymptotic-time perturbation behavior. It should also be noted that the asymptotically long time result of transient growth theory is identical with that predicted by modal analysis via solution of the EVP.
Finally, The *gain function*, $G(t)$, is defined (Schmid and Henningson 2001) at an arbitrary time, t, as the ratio of perturbation energy at any time to initial perturbation energy of an eigenvector $\hat{\mathbf{q}}$, itself a function of the streamwise and spanwise wavenumbers, α and β respectively, as

$$G(t) \equiv G(\alpha,\beta,R,t) = \max_{\hat{\mathbf{q}}(0)} \frac{\|\hat{\mathbf{q}}(t)\|_E^2}{\|\hat{\mathbf{q}}(0)\|_E^2}$$
$$= \|e^{-it\mathscr{L}}\|_E^2 = \|\mathbf{F}\Lambda\mathbf{F}^{-1}\|_2^2$$

Table 3.1: Definition of the energy gain function

Since transient growth analysis is linear, it is necessary to refer predictions at any given time, t, to an initial level of the monitored quantity. From a physical point of view it is meaningful to define the gain in terms of an initial perturbation energy and monitor its evolution in time. The level of TG is then quantified by $G_{\max}(t)$, the maximum value of the gain function attained over time, and referred to its initial value that is commonly scaled to unity in this linear context. As can be seen in (3.1) the base flow may be time-dependent, since time is treated in as a parameter of transient growth analysis. The objective of linear TG analysis is the identification of conditions at which large energy gains can lead flow to nonlinearity. The analysis can also identify the (optimal) initial conditions that give rise to transiently most amplified perturbations. From a technical point of view one solves the direct and adjoint eigenvalue problems, a small number of eigenvectors is retained, the bi-orthogonality condition is used to determine mode amplitudes and the solution of the IVP is reconstructed using this small number of eigenvectors (Theofilis et al. 2003, Rodríguez et al. 2011). The utility of the $\epsilon-$pseudospectrum lies in that it provides bounds on the level of (environmental) perturbations necessary for the modal scenario to be by-passed. Pseudo-resonances may be identified by the resolvent at parameters (well) away from those delivered by EVP analysis.

3.4 Linear resolvent analysis

The concept of transient growth analysis discussed in the previous sections can be extended to include the response of a given flow to linear external forcing. The underlying theory is commonly known as *resolvent analysis*, although

the term resolvent is strictly defined by equation (3.6). While TG analysis predicts the intrinsic instability behavior of the EC at the given conditions analyzed, resolvent analysis predicts the response of the same flow to a wide variety of externally imposed forcing functions f. Formally, equation (3.1) is extended to include an arbitrary forcing, f,

$$\frac{\partial \hat{\mathbf{q}}}{\partial t} = \mathcal{L}\hat{\mathbf{q}} + f\mathrm{e}^{i\omega t}. \tag{3.10}$$

The relationship of (3.10) with the resolvent can be made clear by introducing a harmonic perturbation and rearranging

$$\hat{\mathbf{q}} = \tilde{\mathbf{q}}_p \mathrm{e}^{i\omega t}, \tag{3.11}$$
$$i\omega\tilde{\mathbf{q}}_p = \mathcal{L}\tilde{\mathbf{q}}_p + f, \tag{3.12}$$
$$\tilde{\mathbf{q}} = (i\omega - \mathcal{L})^{-1} f. \tag{3.13}$$

During the execution of the present grant the above expressions have been implemented into the transient-growth analysis code constructed. However a systematic investigation of the effect of harmonic perturbations introduced on the elliptic cone surface has not been performed but has been identified as a potential field for future work in this area.

Chapter 4

Global Transient Growth in Compressible 3D Flows

The objective of the present effort is the development of global linear non-modal / transient growth (TG) instability analysis tools for hypersonic spatially inhomogeneous flows. Subsequently, the codes developed are to be applied to determine the relative importance of modal and non-modal scenarios on an elliptic cone. The approach followed first computes the pseudospectrum / resolvent of the discretized Jacobian and subsequently computes optimal initial perturbations and their time-evolution. The level of transient energy growth, $G(t)$, may be used to identify the potential of hypersonic flows to sustain streamwise-aligned (linear) algebraically growing perturbations in low-disturbance (flight) and high-disturbance (wind-tunnel) environments. Flow parameters affecting the TG scenario and need to be examined include altitude, frequency(-ies) as well as streamwise and spanwise wavenumber(-s). In the present work, the same base flows received from WPAFB and analyzed with respect to their modal instability by Paredes et al. (2016b) are employed to enquire their potential to sustain global transient growth. Specifically, attention is first paid to the conditions at which the modal analysis has been performed $Ma = 7$, unit $Re = 1.9 \times 10^6 \frac{1}{m}$, corresponding to an altitude of $h = 33km$, and the results obtained are compared with those at a second set of conditions at $H = 21km$. Details of the underlying theory and the parametric studies performed follow.

4.1 The initial value problem

The decomposition of any flow quantity ($\mathbf{q}$) into a steady laminar base or mean flow plus a small amplitude disturbance

$$\mathbf{q}(\mathbf{x}, t) = \bar{\mathbf{q}}(\mathbf{x}) + \epsilon \tilde{\mathbf{q}}(\mathbf{x}, t), \qquad with \quad \epsilon \ll 1, \tag{4.1}$$

substituted into the compressible Navier-Stokes equations presented in the earlier section gives rise to the well-known compressible linearized Navier-Stokes equations (LNSE). These can be written as an initial-value-problem (IVP) in the form of

$$\mathcal{B} \frac{\partial \tilde{\mathbf{q}}}{\partial t} = \mathcal{A} \tilde{\mathbf{q}} \tag{4.2}$$

where the matrices $\mathcal{A}$ and $\mathcal{B}$ contain the spatial discretization, the base flow and its derivatives.
Multiplying both sides of the system by $\mathcal{B}^{-1}$ gives

$$\frac{\partial \tilde{\mathbf{q}}}{\partial t} = \mathcal{L} \tilde{\mathbf{q}} \tag{4.3}$$

where $\tilde{\mathbf{q}}(x,y,z,t) = (\tilde{u},\tilde{v},\tilde{w},\tilde{T},\tilde{P})^T$ is the vector containing the disturbance functions of velocity, temperature and pressure (Theofilis 2011a) and $\mathcal{L} = \mathcal{B}^{-1}\mathcal{A}$ is a linear operator mapping the flow field to its time derivative and contain the appropriated boundary conditions. Note that the matrix $\mathcal{B}$ is non-singular in the compressible regime, so it is possible to compute its inverse.
The solution of the IVP is given in general form by

$$\tilde{\mathbf{q}} = \exp(t\mathcal{L})\tilde{\mathbf{q}}_\mathbf{0}, \tag{4.4}$$

where $\tilde{q}_0$ is the initial condition. It is important to notice that, so far, no approximations regarding the shape of the disturbances or their temporal behavior have been introduced. The matrix exponential $\mathcal{L}$ can also been seen as the stability operator after the linearization step described before.

4.2 Quantitative description of energy growth - the Gain function

Defining stability as the amplification of initial disturbance energy over a prescribed time interval (Schmid and Henningson 2001, Schmid 2007) and optimizing it over all permissible initial conditions the *gain function* $G(t)$ may be defined as the maximum optimal energy amplification

$$G(t) = \underset{\tilde{\mathbf{q}}_\mathbf{0}}{max}\frac{E(\tilde{\mathbf{q}}(t))}{E(\tilde{\mathbf{q}}_\mathbf{0})}, \tag{4.5}$$

($E\tilde{\mathbf{q}}$) being the energy of the disturbance. Substituting (4.4) into the above definition of energy amplification yields to

$$G(t) = \underset{\tilde{\mathbf{q}}_\mathbf{0}}{max}\frac{||\tilde{\mathbf{q}}(t)||_E^2}{||\tilde{\mathbf{q}}_\mathbf{0}||_E^2} = \underset{\tilde{\mathbf{q}}_\mathbf{0}}{max}\frac{||\exp(t\mathcal{L}\tilde{\mathbf{q}}_\mathbf{0})||_E^2}{||\tilde{\mathbf{q}}_\mathbf{0}||_E^2} = ||\exp(t\mathcal{L})||_E^2 \tag{4.6}$$

The norm of the disturbance will be defined shortly. This energy norm of the matrix exponential represents therefore the largest amplification of energy that any infinitesimal initial disturbance can experience given a time interval. In general, the matrix exponential is hard to compute, and an eigenvalues decomposition of $\mathcal{L}$ is used as proxies

$$||\exp(t\mathcal{L})||_E^2 = ||\exp(t\mathcal{V}\Lambda\mathcal{V}^{-1})||_E^2 = ||\mathcal{V}\exp(t\Lambda)\mathcal{V}^{-1}||_E^2 \tag{4.7}$$

where $\mathcal{V}$ is the matrix containing the normalized eigenvectors and Λ is a matrix containing the eigenvalues in its diagonal. The above expression is very important to understand the difference between the present analysis and a classical stability analysis. The eigenvalues of Λ represent only part of G(t), and this will predict indeed the behavior of the disturbances only if the similarity transformation give by the eigenvectors does not change the value of the norm. This is true only when the eigenvectors are orthogonal to each other. System matrices resulting in non orthogonal eigenvectors are called non-normal matrices, whereas matrices with orthogonal eigenvectors are called normal. Schmid and Henningson (2001) summarized this presenting upper and lower bounds (estimates) of the operator exponential norm. They showed that since the energy cannot decay at a faster rate than that given by the least stable eigenvalue the lower bound is given by this mode. For the upper bond, the eigenvalue decomposition 4.7 is used evoking the triangle inequality to split the norm

$$\exp(2t\lambda_{max}) \quad \leq \quad ||\exp(t\mathcal{L})||_E^2 \quad \leq \quad ||\mathcal{V}||_E^2||\mathcal{V}^{-1}||_E^2 \ \exp(2t\lambda_{max}). \tag{4.8}$$

From this bonds, two cases can be distinguished. If $||\mathcal{V}||_E^2||\mathcal{V}^{-1}||_E^2 = 1$ then the upper and lower bound are the same. In this case, the energy amplification is indeed governed by the least stable eigenvalue λ_{max}. However, if this value is much larger then 1, the upper and lower bound differ significantly and the energy amplification is governed by the least stable eigenvalue only for asymptotic period of time.
To capture the short time dynamics, the energy growth rate is expanded around $t = 0^+$ using a Taylor-series. The initial growth rate is given by

$$\left.\frac{dG}{dt}\right|_{t=0^+} = \frac{\langle \tilde{\mathbf{q}}_\mathbf{0}, (\mathcal{L}+\mathcal{L}^H)\tilde{\mathbf{q}}_\mathbf{0}\rangle}{\tilde{\mathbf{q}}_\mathbf{0}, \tilde{\mathbf{q}}_\mathbf{0}} = \lambda_{max}(\mathcal{L}+\mathcal{L}^H) \tag{4.9}$$

where $(\mathcal{L}+\mathcal{L}^H)$ is hermitian. The full calculation is showed by Farrell and Ioannou (1996), Schmid and Henningson (2001) and Trefethen and Embree (2005). The slop of G(t) at $t = 0^+$ is given by the largest eigenvalue of $(\mathcal{L}+\mathcal{L}^H)$ as addressed in (4.9). This quantity is known as the numerical abscissa. This expression can be further generalized given rise to the concept of numerical range or field of values. Following a similar procedure:

$$\frac{d}{dt}||\tilde{\mathbf{q}}||_E^2 = \left\langle \frac{d}{dt}\tilde{\mathbf{q}}, \tilde{\mathbf{q}} \right\rangle_E + \left\langle \tilde{\mathbf{q}}, \frac{d}{dt}\tilde{\mathbf{q}} \right\rangle_E = 2\Re\{\langle \mathcal{L}\tilde{\mathbf{q}}, \tilde{\mathbf{q}}\rangle_E\}. \tag{4.10}$$

This establishes the set in the complex plane of all Rayleigh quotients of $\mathcal{L}$. The maximum real part of the numerical range is equivalent to the numerical abscissa. Thus, the slop of G(t) at $t = 0^+$ corresponds to the maximum protrusion of the numerical range into the unstable half-plane. Two important properties of the numerical range can be addresses. The numerical range is convex and, for normal $\mathcal{L}$, it is simply the convex hull of the spectrum. To summarize, for non-normal stability problems, the numerical range (abscissa) governs the very short time behavior whereas the least stable eigenvalue governs the long time behavior.

For intermediate time, the amount of maximum transient growth can be approximated by the ϵ-pseudospectrum (Trefethen 1997). The ϵ-pseudospectra can be defined as the set in the complex plane, parameterized by ϵ, where the resolvent norm is larger than the inverse of ϵ. Measuring how far the contours of the this norm extend into the unstable half-plane indicates a lower bound for the maximum achievable transient growth in time. Trefethen and Embree (2005) defined a constant $\mathcal{K}$, known as the Kreiss constant, used to determine this lower band as $max_{t>0}\ G(t) \geq \mathcal{K}^2$.

The concepts explained here are better understood by calculating the spectrum, numerical range and the ϵ-pseudospectrum for the two-dimensional plane Poiseuille flow and the results can be seen in Fig. 4.1. The eigenvalues are displayed as blued dots, and for the parameters chosen, they are all asymptotically stable (driven by the least stable eigenvalue). The boundary of numerical range is indicated in red and it extends into the unstable half-plane, showing that transient growth are expect for small times. The red dot represents the numerical abscissa, which measures the maximum protrusion of the numerical range into the unstable half-plane. The numerical abscissa gives the slope of the initial maximum energy growth G(t) as presented in (4.9). Finally, the square of the Kreiss constant ($\mathcal{K}^2$), indicated by a black dot, gives a lower estimate for the peak of energy amplification.

Additional interpretation of the resolvent norm is as an eigenvalue sensitivity. For a well-posed system, it is expected that small disturbances have a minimum effect. Disturbing the matrix exponential $\mathcal{L}$ by random matrices of small norm and estimating the effect on the eigenvalues show that resolvent contours contain eigenvalues of the disturbed matrix. Therefore, highly sensitive eigenvalues are often the first sign of non-normality.

4.3 Definition of the energy norm

Recapitulating the start of the analysis, (4.5) requires the definition of an inner product and its associated norm. These quantities constitute the fundamental measure and orthogonality describing the transient behavior. As pointed out by Hanifi et al. (1996a), the energy density of a disturbance is a natural and physically meaningful measure of its size in the context of an incompressible flow. However, no obvious choice exists when dealing with compressible flows. For this reason, they re-derived the norm proposed by Mack (1969) in the context of modal instability, requiring pressure work to be conservative. Chu (1965) also described this energy norm, and the possibility to use different $\tilde{\mathbf{q}}$ vectors. Mathematically, the inner product can be written as

$$(\tilde{\mathbf{q}}_\mathbf{i}, \tilde{\mathbf{q}}_\mathbf{j}) = \int_0^\infty \tilde{\mathbf{q}}_\mathbf{i}^H \mathcal{M} \tilde{\mathbf{q}}_\mathbf{j} dy \tag{4.11}$$

whereas the associated norm is

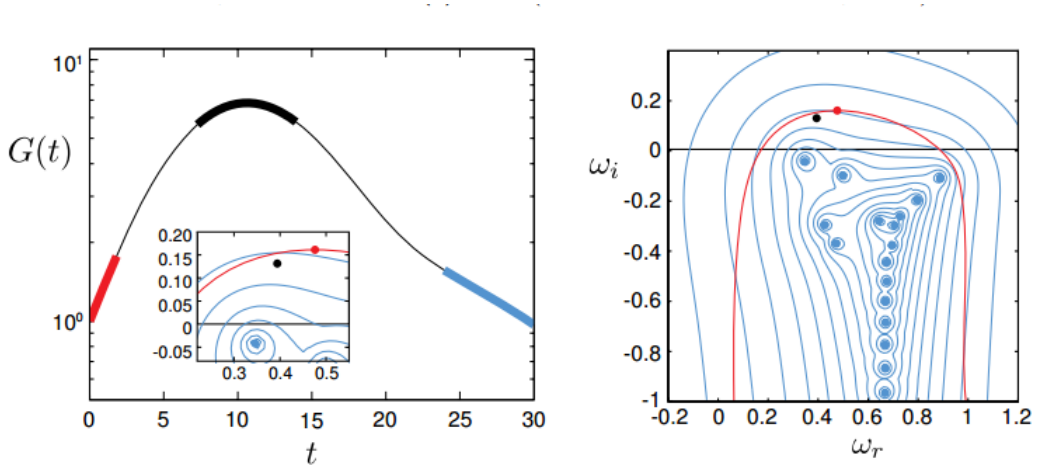

Figure 4.1: Transient growth of disturbance energy for the two-dimensional plane Poiseuille flow at $Re = 10^3$ and $\alpha = 1$. Left hand side shows energy growth x time. The right hand side shows contour plot (blue lines) of the resolvent norm in the complex plane.

$$2E = (\tilde{\mathbf{q}}, \tilde{\mathbf{q}}) = ||\tilde{\mathbf{q}}||_E^2 \tag{4.12}$$

with

$$\mathcal{M} = diag\left(\bar{\rho}, \bar{\rho}, \bar{\rho}, \frac{\bar{\rho}}{\gamma(\gamma-1)\bar{T}Ma^2}, \frac{Ma^2}{\bar{\rho}\bar{T}}\right) \tag{4.13}$$

if $\tilde{\mathbf{q}} = (\tilde{u}, \tilde{v}, \tilde{w}, \tilde{T}, \tilde{p})$. The overbar indicates base flow quantities. The relation between the above energy norm and the standard Euclidean L_2 norm can be established by the following transformation (Reddy and Henningson 1993, Schmid and Henningson 2001, Trefethen and Embree 2005):

$$E(\tilde{\mathbf{q}}) = ||\tilde{\mathbf{q}}||_E^2 = \langle \tilde{\mathbf{q}}, \tilde{\mathbf{q}} \rangle_E = \tilde{\mathbf{q}}^H \mathcal{M} \tilde{\mathbf{q}} = \tilde{\mathbf{q}}^H F^H F \tilde{\mathbf{q}} = \langle F\tilde{\mathbf{q}}, F\tilde{\mathbf{q}} \rangle_2 = ||F\tilde{\mathbf{q}}||_2^2. \tag{4.14}$$

The energy weight matrix is defined in (4.13). This matrix is positive definite since it contains positive quantities (energy norm). Thus, it can be decomposed via a Cholesky decomposition, generating F and F^H. The energy norm of the disturbance is then equivalent to take the Euclidean L_2 norm of the vector $F\tilde{\mathbf{q}}$. For matrices, using the definition of a vector-induced norm

$$||\mathcal{L}||_E = \max_{\tilde{\mathbf{q}}} \frac{||\mathcal{L}\tilde{\mathbf{q}}||_E}{||\tilde{\mathbf{q}}||_E} = \max_{\tilde{\mathbf{q}}} \frac{||F\mathcal{L}F^{-1}F\tilde{\mathbf{q}}||_2}{||F\tilde{\mathbf{q}}||_2} = ||F\mathcal{L}F^{-1}||_2. \tag{4.15}$$

Therefore, for matrices, a simple similarity transformation using the Cholesky decomposition relates the energy norm to the Euclidean L_2 norm.

4.4 Transient growth calculation

In order to make further simplification of the linearized governing equations presented before (4.3), an expansion of the vector quantities $\tilde{\mathbf{q}}$ in the vector eigenfunctions of the linear initial value problem is necessary. Considering that the flow analyzed is inhomogeneous in two spatial directions (x,y) and homogeneous in the third (z), a Fourier transformation can be used to write:

$$\tilde{\mathbf{q}}(x,y,z,t) = \hat{\mathbf{q}}(x,y)\ \exp(i(\beta z - \omega t)) \tag{4.16}$$

where β is the wavenumber in the streamwise direction and ω is a complex number. Introducing this decomposition into the IVP (4.3) give rise to a generalized eigenvalue problem of the form

$$\mathcal{L}\hat{\mathbf{q}} = i\omega\hat{\mathbf{q}} \tag{4.17}$$

where the entries of the matrix $\mathcal{L}$ can be easily recovered from the linearized equations after introducing (4.16). In this case, a temporal analysis is chosen and the flow is classified as linearly unstable if the imaginary part of the eigenvalue ω is positive. Since a decision about the scalar product and norm has already been made, the transient growth analysis can be further investigated. Restricting the analysis to the space spanned by the first N eigenfunctions of (4.17)

$$span\{\hat{\mathbf{q}}_1, \hat{\mathbf{q}}_2, \hat{\mathbf{q}}_3, ..., \hat{\mathbf{q}}_N\} \tag{4.18}$$

the state vector $\tilde{\mathbf{q}}$ can be expressed in terms of this basis:

$$\tilde{\mathbf{q}} = \sum_{k=1}^{N} \mathcal{K}_k(t)\hat{\mathbf{q}}_k, \tag{4.19}$$

where

$$\mathcal{K}_k(t) = \mathcal{K}_k(0)\ \exp(-i\omega_k t) \tag{4.20}$$

with $\mathcal{K}_k$ as the time-dependent expansion coefficients. Thus, the eigenvalues represent the linear evolution operator projected onto the space spanned by the first N eigenvectors. Restricting the transient growth analysis to this space and applying the scalar product and the energy norm defined previously by equations (4.11 - 4.12) leads to

$$G(t) = G(\beta, Re, Ma, t) = \max_{\tilde{\mathbf{q}}_0} \frac{||\tilde{\mathbf{q}}(t)||_E^2}{||\tilde{\mathbf{q}}(0)||_E^2} = ||\exp(-it\mathcal{L})||_E^2 = ||F\Lambda F^{-1}||_2^2. \tag{4.21}$$

where

$$\Lambda = diag(\exp(-it\omega_1), \exp(-it\omega_2), ..., \exp(-it\omega_N)) \qquad \mathcal{A} = F^H F \tag{4.22}$$

and $\mathcal{A}$ defined as the scalar product presented in (4.11). The maximum gain is thus the square of the largest single value.

4.5 Linear optimal disturbances

As discussed before, for non-normal systems exhibiting substantial potential to transient growth ,it is important to calculate the initial condition that optimizes the energy amplification factor G_{max}. This initial condition can be different for different times and the resulting curve G(t) should be thought of as the envelope of the energy evolution of individual initial conditions. Nevertheless, to determine the initial condition that reach the maximum possible amplification at a given time t^* a singular value decomposition (SVD) of the expression in (4.21) can be performed:

$$\mathcal{B}V = U\Sigma \tag{4.23}$$

where $\mathcal{B} = F\Lambda F^{-1}$ and V and U are unitary matrices with ortho-normalized columns and Σ is a diagonal matrix consisting of the singular values, ordered in size, i.e. $\sigma_1 \geq \sigma_2 \geq ...\sigma_N$. The dominant singular value is equivalent to the energy norm of $\exp(-t\omega_k)$. Thus, extracting the principal column vectors of V and U leads to

$$\mathcal{B}v_1 = \sigma_1 u_1. \tag{4.24}$$

As pointed out by Schmid and Henningson (1994), this equation can be interpreted as a mapping $\mathcal{B}$ of an input vector v_1 onto an output vector u_1 stretched by a factor of the largest single value. Therefore, it is straightforward to identify the optimal initial condition as the principal right singular value vector and the principal left singular vector as the resulting state-vector. Furthermore, since equation (4.21) is advanced in time, it is clear that every step will produce it own optimal disturbance. Finally, to recover the initial expansion coefficients of equation (4.19), which give the optimal disturbances associated with a particular amplification, it is necessary to write v_1 in the basis $\{\hat{\mathbf{q}}_1, ..., \hat{\mathbf{q}}_N\}$ as:

$$v_1 = F\mathcal{K}_0. \tag{4.25}$$

Thus, the computational steps required to recover the optimal initial condition is a singular value decomposition (SVD) of the matrix exponential evaluated at different specified time t^*.

4.6 Iterative eigenvalue problem computation

The iterative numerical solution of the large-scale eigenvalue problems encountered in this analysis implements Krylov subspace iteration based on serial and parallel versions of the Arnoldi algorithm. This approach delivers a number of eigenvalues in the vicinity of a specific target eigenvalue and is substantially less expensive than the classic QZ method (Arnoldi 1951, Saad 1980). The number of eigenvalues delivered is determined by the Krylov subspace dimension, a free parameter in the analysis, whose limit is the leading dimension of matrices $\mathbf{A}$ and $\mathbf{B}$. In this eigenvalue problem, a so-called shift-an-invert strategy is also implemented, in which the problem solve is (Theofilis 2003)

$$\mathbf{CX} = \mu\mathbf{X}, \qquad C = (\mathbf{A} - \sigma\mathbf{B})^{-1}\mathbf{B}, \qquad \mu = \frac{1}{\omega - \sigma} \tag{4.26}$$

where μ is the new eigenvalue searched, ω is the shift parameter and the Krylov subspace is constructed by

$$K_m = span(\mathbf{v}, C.\mathbf{v}, C^2.\mathbf{v}, ..., C^{m-1}.\mathbf{v}) \tag{4.27}$$

where m is the dimension of the subspace.
The vectors $\mathbf{v}$ forming the basis are ordered by columns into the matrix $\mathbf{V}_m$. The projection of the linear operator on that basis yields the relation

$$\mathbf{V}_m^H C \mathbf{V}_m = \mathbf{H}_m \tag{4.28}$$

where $\mathbf{H}_m$ is an upper triangular Hessenberg matrix. The restrictions of the eigenvalue problem to the Krylov subspace K_m is

$$\mathbf{H}_m \mathbf{V}_m^H . \hat{\mathbf{q}} = \mu \mathbf{V}_m^H . \hat{\mathbf{q}} \tag{4.29}$$

The eigenvalues of the Hessenberg matrix $\mathbf{H}_m$ are approximations to the m largest eigenvalues of the original problem.
With regard to the eigenvector, if $y_i^{(m)}$ is the eigenvector corresponding to the i-th eigenvalue of the $\mathbf{H}_m$ the corresponding approximation to the eigenvector of the original problem, known as Ritz vector, is

$$\hat{\mathbf{q}}_i = \mathbf{V}_m . \mathbf{y}^{(m)} \tag{4.30}$$

4.7 Singular Value Decomposition

The singular-value decomposition (SVD) is a generalization of the eigenvalue decomposition for positive semi-definite normal rectangular matrices of dimension. Its relevance to the problem at hand is that for any complex matrix **C**, as defined in (4.26) a matrix **M** can be constructed using the adjoint (complex conjugate, transposed) matrix $\mathbf{C}^*$ as

$$\mathbf{M} = \mathbf{C}^*\mathbf{C}. \tag{4.31}$$

The SVD of a general $m \times n$ matrix **M** takes the form (Taira et al. 2017)

$$\mathbf{M} = \mathbf{U}\Sigma\mathbf{V}^*, \tag{4.32}$$

where U is an $m \times m$ unitary matrix, Σ is a diagonal $m \times n$ matrix with non-negative real numbers on the diagonal, V is an $n \times n$ unitary matrix and V^* is the conjugate transpose of V. The diagonal entries σ_i of Σ are known as the singular values of M and they are ordered in size, i.e. $\sigma_1 \geq \sigma_2 \geq ... \geq \sigma_n$. Also, is important to notice that singular value decomposition is defined for all matrices (rectangular or square) unlike the more commonly used spectral decomposition in Linear Algebra. In contrast to the eigenvalue decomposition, the columns of V in the singular value decomposition, called the right singular vectors, always form an orthogonal set with no assumptions on the matrix **M**. The columns of U are called the left singular vectors and they also form an orthogonal set.
The Singular Value Decomposition can be understood in a simple geometrical two-dimensional example. If $\mathbf{M} = \mathbf{U}\Sigma\mathbf{V}^*$, then:

$$\begin{aligned} \mathbf{MV} &= (\mathbf{U}\Sigma\mathbf{V}^*)\mathbf{V} \\ \mathbf{MV} &= \mathbf{U}\Sigma I \\ \mathbf{MV} &= \mathbf{U}\Sigma \end{aligned} \tag{4.33}$$

where I is the identity matrix. Figure 4.2 shows an example of an unit circle linearly transformed by the matrix **M** to an ellipse. The entries of the pre-factor **U** correspond to the minor and major axis of the ellipse. In the other hand, $\mathbf{V}^*$ are the the radius that get mapped by the transformation to the ellipse axis.

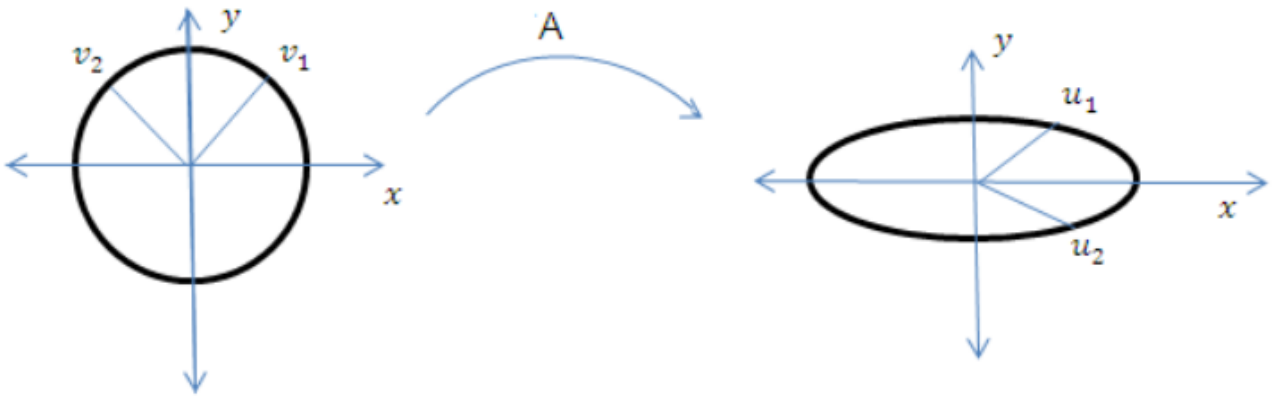

Figure 4.2: Geometric interpretation of the Singular Value Decomposition (Taira et al. 2017, Raghavendar and Dharmaiah 2017).

Chapter 5

Further Development of Nonlinear PSE-3D

A new global instability analysis methodology has been developed in recent years in the PI's group has been denominated PSE-3D (or "plane-marching PSE"); elements of the theory were presented by Theofilis (2011b). PSE-3D permits following linear BiGlobal instability analysis results through transition to turbulence since, unlike BiGlobal theory, PSE-3D can be formulated in a nonlinear context. Nonlinear PSE-3D (NL-PSE3D) analysis is initialized using results of the spatial BiGlobal eigenvalue problem, obtained at a given streamwise location on the cone. NL-PSE3D then advances the modes downstream, permitting their nonlinear interaction and the (nonlinear) generation and growth of new modes. The energy of the growing modes is extracted from that of the base flow and laminar-turbulent transition occurs when the level of nonlinear oscillations of the perturbation energy (square root of sum of squares of amplitudes of all nonlinearly generated modes) reaches $O(1)$ levels. In the present reporting period, development of the nonlinear PSE-3D was completed and a number of validation cases were performed; details follow.

The development in time and space of small-amplitude perturbations superposed upon a given flow can be described by the Linearized Navier-Stokes equations (LNSE). Linearization of the equations of motion is performed around a steady laminar flow, here denoted as $\bar{\mathbf{q}} = (\bar{\rho}, \bar{u}, \bar{v}, \bar{w}, \bar{T})^T$. The components of the state vector are density, streamwise-, normal- and spanwise velocities, and temperature, respectively. We denote the small-amplitude perturbations superimposed on the mean flow as $\tilde{\mathbf{q}} = (\rho, \tilde{u}, \tilde{v}, \tilde{w}, \tilde{T})^T$. In general, mean and perturbation fields are functions of time t, streamwise-, normal- and spanwise coordinates $x,\ y$ and z. Now, let us expand the perturbation field in terms of its truncated Fourier series as

$$\tilde{\mathbf{q}}(x,y,z,t) = \sum_{n=-N}^{N} \breve{\mathbf{q}}_n(x,y,z) \exp\left[-\mathrm{i}n\omega t\right], \tag{5.1}$$

where the term $\breve{\mathbf{q}}_n$ can be a fast varying wavy function and ω denotes the real angular frequency of the perturbations. Note that since the perturbations are real quantities, $\breve{\mathbf{q}}_{-n}$ is equal to the complex conjugate of $\breve{\mathbf{q}}_n$. By applying a WKB type of approximation, we can write the Fourier amplitudes as

$$\breve{\mathbf{q}}_n(x,y,z) = \hat{\mathbf{q}}_n(x,y,z) \exp\left[\mathrm{i}\int_x \alpha_n(x')dx'\right], \tag{5.2}$$

where $\hat{\mathbf{q}}_n$ is the shape function of perturbation and α_n its corresponding wavenumber, both with slow variation in streamwise direction. Thus, we assume $\partial/\partial x \sim \mathcal{O}(Re^{-1})$. Substituting the decomposition of flow variables along with definitions (5.1) and (5.2) into the NS equations, and neglecting terms of $\mathcal{O}(Re^{-2})$ and higher, the compressible nonlinear PSE-3D equations can be written in a compact form as

$$\left(\mathbf{L}_n + \mathbf{M}_n \frac{\partial}{\partial x}\right) \hat{\mathbf{q}}_n(x,y,z) = \mathbf{F}_n(x,y,z) \exp\left[-\mathrm{i}\int_x \alpha_n(x')dx'\right], \tag{5.3}$$

where $\mathbf{F}_n$ is the Fourier component of the total forcing $\mathbf{F}$, arising in the nonlinear terms. The entries of the matrix coefficients $\mathbf{L}_n$ and $\mathbf{M}_n$ and vector $\mathbf{F}$ are found in Paredes (2014).

5.1 Normalization condition

An ambiguity exists in the PSE formulation, since both the shape function $\hat{\mathbf{q}}$ and the wavenumber α depend on the streamwise coordinate, x. Therefore, the changes in amplitude along the slow spatial direction can be contained both in the amplitude function $\hat{\mathbf{q}}$ or in the wavenumber α. A normalization condition is required in order to close the formulation of the problem (see Herbert (1997, 1994) for a review). In this work, the following normalization condition is used:

$$\int_{\Omega} \hat{\mathbf{q}}^{\dagger} \frac{\partial \hat{\mathbf{q}}}{\partial x} \, d\Omega = 0. \tag{5.4}$$

where Ω denotes the extend of the computational domain in cross-stream directions. This normalization imposes that the variation of shape functions with respect to x remains small. Thus, the amplitude growth is mostly absorbed into the phase function.

5.2 Numerical stability

The nature of the obtained stability equations is parabolic and numerical instabilities can occur when the streamwise step of integration is too small. The studies of Li and Malik (1994, 1997) and Andersson et al. (1999) for PSE and the generalization to PSE-3D of Broadhurst and Sherwin (2008) show that these formulations contain some residual ellipticity that makes them ill-posed. It can be shown (Li and Malik 1997) that when using an implicit scheme along with sufficiently large streamwise steps, the upstream propagating modes are not captured in the numerical integration, thus permitting the stable integration of downstream propagating instabilities. For a first order backward difference scheme in the marching direction, a limit of $\Delta x > 1/|\alpha|$, needs to be imposed on the marching step size for stability purposes.

5.3 Initial condition: Spatial BiGlobal analysis

Spatial BiGlobal analysis is the analog of classic local spatial LST if two inhomogeneous spatial directions are resolved simultaneously while the third direction is considered locally homogeneous. The results offered by spatial BiGlobal analysis is necessary to obtain the shape function, wavenumber, and damping/growth-rate, required as initial conditions of the PSE-3D marching integration. In order to proceed, the base flow is assumed to be locally independent of one spatial coordinate x (but depending on the other two spatial directions, y and z, in a coupled inhomogeneous manner). Flow quantities are then decomposed according to

$$\mathbf{q}(x, y, z, t) = \bar{\mathbf{q}}(y, z) + \tilde{\mathbf{q}}(x, y, z, t), \quad \varepsilon \ll 1, \tag{5.5}$$

where $\varepsilon\tilde{\mathbf{q}}$ represents the unsteady three-dimensional infinitesimal perturbations, being inhomogeneous in y and z and periodic in x. Thus, one may write

$$\tilde{\mathbf{q}}(x, y, z, t) = \hat{\mathbf{q}}(y, z)\Theta(x, t) + \text{c.c.}, \tag{5.6}$$

with $\hat{\mathbf{q}}$ representing the vector of two-dimensional complex amplitude functions and

$$\Theta = \exp[\mathrm{i}(\alpha x - \omega t)], \tag{5.7}$$

a complex phase function. The linear disturbance equations of spatial BiGlobal stability analysis are obtained at $\mathcal{O}(\varepsilon)$ by substituting (5.5) into the governing equations, subtracting out the $\mathcal{O}(1)$ base flow terms and neglecting terms at $\mathcal{O}(\varepsilon^2)$. In the present spatial framework, ω is taken to be a real angular frequency parameter, while

the complex eigenvalue α, and the associated eigenvectors $\hat{\mathbf{q}}$ are sought. The real part of the eigenvalue α_r is related with the wavenumber of the eigenmode along the homogeneous spatial direction x, $\alpha_r = 2\pi/L_x$, while the imaginary part is its growth/damping rate; a negative value of α_i indicates exponential growth of $\tilde{\mathbf{q}}$ in space, while $\alpha_i > 0$ denotes decay of $\tilde{\mathbf{q}}$ in space. The resulting two-dimensional PDE-based EVP is nonlinear on eigenvalue α, but it is converted into a linear eigenvalue problem, which is larger in size by a factor equal to the degree of non-linearity (Theofilis 1995), using the companion matrix method (Bridges and Morris 1984b), in which an auxiliary vector is defined, $\hat{\mathbf{q}}_{ext} = [\hat{\rho}, \hat{u}, \hat{v}, \hat{w}, \hat{T}, \alpha\hat{u}, \alpha\hat{v}, \alpha\hat{w}, \alpha\hat{T}]^T$, and the resulting EVP is

$$\mathbf{A}\hat{\mathbf{q}}_{ext} = \alpha\mathbf{B}\hat{\mathbf{q}}_{ext}, \tag{5.8}$$

or, explicitly,

$$\begin{pmatrix} \mathcal{A}_{11} & \mathcal{A}_{12} & \mathcal{A}_{13} & \mathcal{A}_{14} & 0 & 0 & 0 & 0 & 0 \\ \mathcal{A}_{21} & \mathcal{A}_{22} & \mathcal{A}_{23} & \mathcal{A}_{24} & \mathcal{A}_{25} & 0 & 0 & 0 & 0 \\ \mathcal{A}_{31} & \mathcal{A}_{32} & \mathcal{A}_{33} & \mathcal{A}_{34} & \mathcal{A}_{35} & 0 & 0 & 0 & 0 \\ \mathcal{A}_{41} & \mathcal{A}_{42} & \mathcal{A}_{43} & \mathcal{A}_{44} & \mathcal{A}_{45} & 0 & 0 & 0 & 0 \\ \mathcal{A}_{51} & \mathcal{A}_{52} & \mathcal{A}_{53} & \mathcal{A}_{54} & \mathcal{A}_{55} & 0 & 0 & 0 & 0 \\ 0 & 0 & 0 & 0 & 0 & \mathcal{I} & 0 & 0 & 0 \\ 0 & 0 & 0 & 0 & 0 & 0 & \mathcal{I} & 0 & 0 \\ 0 & 0 & 0 & 0 & 0 & 0 & 0 & \mathcal{I} & 0 \\ 0 & 0 & 0 & 0 & 0 & 0 & 0 & 0 & \mathcal{I} \end{pmatrix} \begin{pmatrix} \hat{\rho} \\ \hat{u} \\ \hat{v} \\ \hat{w} \\ \hat{T} \\ \alpha\hat{u} \\ \alpha\hat{v} \\ \alpha\hat{w} \\ \alpha\hat{T} \end{pmatrix} =$$

$$= \alpha \begin{pmatrix} \mathcal{B}_{11} & \mathcal{B}_{12} & 0 & 0 & 0 & 0 & 0 & 0 & 0 \\ \mathcal{B}_{21} & \mathcal{B}_{22} & \mathcal{B}_{23} & \mathcal{B}_{24} & \mathcal{B}_{25} & \mathcal{B}_{26} & 0 & 0 & 0 \\ 0 & \mathcal{B}_{32} & \mathcal{B}_{33} & 0 & \mathcal{B}_{35} & 0 & \mathcal{B}_{37} & 0 & 0 \\ 0 & \mathcal{B}_{42} & 0 & \mathcal{B}_{44} & \mathcal{B}_{45} & 0 & 0 & \mathcal{B}_{48} & 0 \\ \mathcal{B}_{51} & \mathcal{B}_{52} & \mathcal{B}_{53} & \mathcal{B}_{54} & \mathcal{B}_{55} & 0 & 0 & 0 & \mathcal{B}_{59} \\ 0 & \mathcal{I} & 0 & 0 & 0 & 0 & 0 & 0 & 0 \\ 0 & 0 & \mathcal{I} & 0 & 0 & 0 & 0 & 0 & 0 \\ 0 & 0 & 0 & \mathcal{I} & 0 & 0 & 0 & 0 & 0 \\ 0 & 0 & 0 & 0 & \mathcal{I} & 0 & 0 & 0 & 0 \end{pmatrix} \begin{pmatrix} \hat{\rho} \\ \hat{u} \\ \hat{v} \\ \hat{w} \\ \hat{T} \\ \alpha\hat{u} \\ \alpha\hat{v} \\ \alpha\hat{w} \\ \alpha\hat{T} \end{pmatrix} \tag{5.9}$$

The entries of matrices $\mathbf{A}$ and $\mathbf{B}$ are found in Paredes (2014).

5.4 NPSE3D Results

Three different flow problems have been used to verify the newly developed nonlinear PSE-3D methodology. Firstly, the linear and nonlinear evolution of TS waves in the Blasius boundary layer is computed and compared with those obtained from NOLOT/PSE codeHein et al. (1994), Hanifi et al. (1994), Hein (2005); results were presented in the closing section of our previous work (Theofilis 2011b). Here, two additional validation cases are discussed: using again the Blasius boundary layer as the base flow, the optimal initial perturbation computed by Andersson et al. (1999) is introduced as initial condition of the steady nonlinear PSE-3D equations. The resulting three-dimensional streaky boundary layer is compared with DNS results of Cossu and Brandt (2002). This result is of interest since, in the elliptic cone case too, streamwise-aligned streaky structures have been found experimentally Borg et al. (2011). Finally, the nonlinear evolution of steady fundamental crossflow instabilities on an accelerated three-dimensional boundary layer over a flat plate in crossflow are computed marching along different trajectories and compared with NOLOT/PSE results. The relevance of crossflow instabilities to the elliptic cone flow has been recently documented by Paredes et al. (2016b).

5.4.1 Streaks in the Blasius boundary layer

The nonlinear evolution of the streak is simulated solving the nonlinear PSE-3D for zero frequency $\omega = 0$ perturbations. The streamwise integration is initialized with the optimal disturbanceAndersson et al. (1999). at $Re_0 = 272$. The perturbation is optimized for maximum growth at $Re = 707$ and is computed with a spectral code used in Levin and Henningson (2003) based on an adjoint optimization technique described in Andersson et al. (1999).

Since the direction of the streak is aligned with the marching trajectory, which results in having $\alpha = 0$, no normalization condition is imposed. The spanwise length of the computational domain is set to $L_z = 22.0676$ corresponding to a wavelength of $\beta = 0.284724$, and the wall-normal extension is truncated at $y_{max} = 150$. The domain is discretized using $N_z = 16$ Fourier collocation points in spanwise direction, $N_y = 161$ in wall-normal direction using FD-q8 scheme.

The streak amplitude is defined as

$$A_s = \frac{1}{2}\left[\max_{y,z}(\tilde{u}_s) - \min_{y,z}(\tilde{u}_s)\right], \tag{5.10}$$

where $\tilde{u}_s$ refers to the stationary Fourier mode or MFD. The simulations are initialized with the optimal perturbation having the amplitudes given in Table 5.1. Excellent agreement is observed when comparing the streak evolution with the DNS results of Cossu and Brandt (2002), see Figure 5.1a. Further, the evolution of the TS-wave have been simulated using linear PSE-3D for the streaky boundary layers obtained with nonlinear PSE-3D reported above.The frequency of the TS wave is $\omega = 0.0358$. Here, the kinetic energy of the disturbance $E = \int_\Omega \tilde{u}^\dagger \cdot \tilde{u}\, d\Omega$ is chosen as measure of the TS wave amplitude. Similar to results reported in previous computationalCossu and Brandt (2002), Bagheri and Hanifi (2007) and experimental Fransson et al. (2005) studies, the stabilizing effect of streaks on the two-dimensional TS waves is observed for all streak amplitudes, see Figure 5.1b.

5.4.2 Crossflow perturbations in a three-dimensional boundary layer

Here, the base flow model an experiment made by Bippes (1991) at DLR in Göttingen, where the flow over a swept flat plate was designed to approximate a Falker-Skan-Cooke velocity profile. The same model was used by Högberg and Henningson (1998) to study the secondary instability of crossflow vortices by means of DNS.

In three-dimensional boundary-layers with crossflow Reed and Saric (1989), the direction of the instability waves is not parallel to the direction of the inviscid freestream flow. Because of this, the streamwise wavenumber α is not zero and the direction of the wave is represented as $\tan\phi = \beta/\alpha$ in a local framework. In contrast to the simulations of streaks, the normalization condition needs to be imposed when the PSE (or PSE-3D) is marched along the streamwise direction.

Using the Cartesian coordinate system, the following procedure needs to be considered to compute the nonlinear terms in a satisfactory manner. The amplitude functions are divided into

$$\hat{\mathbf{q}} = \hat{\mathbf{q}}^0 + \hat{\mathbf{q}} + \hat{\mathbf{q}}^+, \tag{5.11}$$

where $\hat{\mathbf{q}}^0$ refers to the zero Fourier mode in z-direction, equivalent to the $\beta_0 = 0$ mode in PSE, and $\hat{\mathbf{q}}^+$ to the complex conjugate, equivalent to the $\beta < 0$ modes in PSE. Then, a nonlinear term, e.g. $\hat{u}\hat{v}$, can be written as

$$\begin{aligned}\hat{u}\hat{v} &= \hat{u}^0\hat{v}^0 + \hat{u}^0\hat{v} + \hat{u}^0\hat{v}^+ + \hat{u}\hat{v}^0 + \hat{u}^+\hat{v}^0 + \hat{u}\hat{v} + \hat{u}\hat{v}^+ + \hat{u}^+\hat{v} \\ &= \hat{u}^0\hat{v}^0 + (\hat{u}^0\hat{v} + \hat{u}\hat{v}^0) + (\hat{u}^0\hat{v} + \hat{u}\hat{v}^0)^+ + \hat{u}\hat{v} + (\hat{u}\hat{v})^+ + \hat{u}\hat{v}^+ + (\hat{u}\hat{v}^+)^+. \end{aligned} \tag{5.12}$$

Table 5.1: Values of initial streak amplitude, $A_{s,0}$ for the computed streaky boundary-layers as in Cossu and Brandt (2002). Note that $A_{s,0} = 0$ refers to the Blasius boundary layer.

Case	A	B	C	D
$A_{s,0}$	0.0000	0.0618	0.0927	0.1235

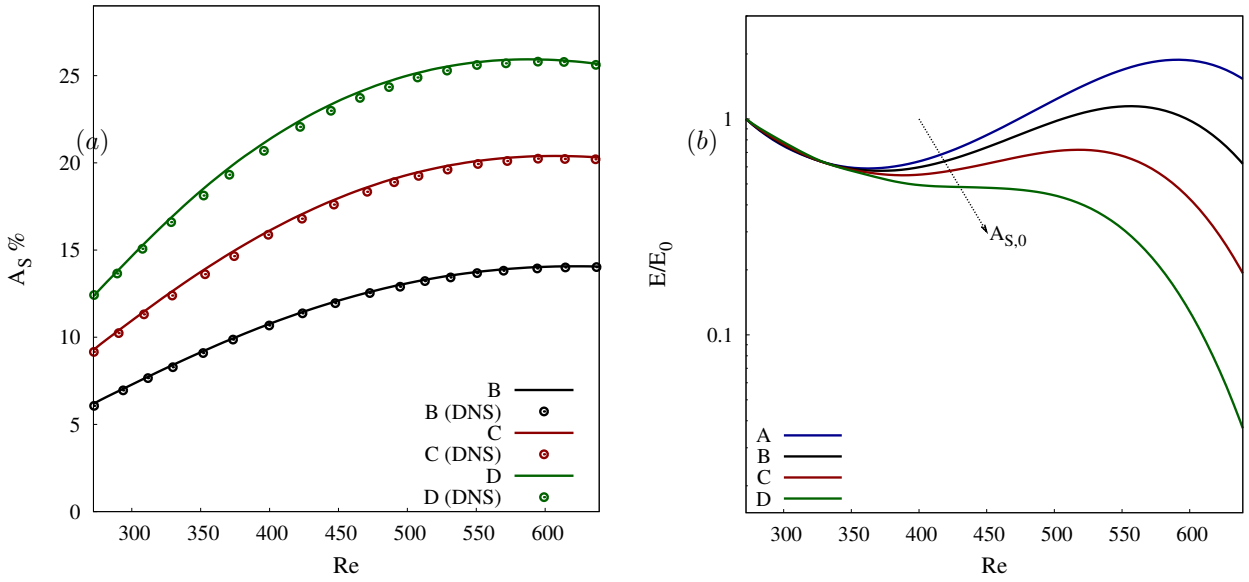

Figure 5.1: Evolution of streak amplitude (a) along streamwise direction computed with nonlinear PSE-3D and kinetic energy evolution of a TS wave (b) computed with linear PSE-3D for $\omega = 0.0358$ using the streaky boundary layers as base flow.

Then, the different terms in equation (5.12) are designated to the nonlinear equations for $\hat{\mathbf{q}}^0$, $\hat{\mathbf{q}}$ and $\hat{\mathbf{q}}^+$ as follows

$$\hat{\mathbf{q}}^0 \quad : \quad \hat{u}^0\hat{v}^0 + \hat{u}\hat{v}^+ + (\hat{u}\hat{v}^+)^+, \tag{5.13}$$

$$\hat{\mathbf{q}} \quad : \quad \hat{u}\hat{v} + \hat{u}^0\hat{v} + \hat{u}\hat{v}^0, \tag{5.14}$$

$$\hat{\mathbf{q}}^+ \quad : \quad (\hat{u}\hat{v})^+ + (\hat{u}^0\hat{v} + \hat{u}\hat{v}^0)^+. \tag{5.15}$$

The evolution of the Fourier modes with $\beta > 0$ is compared between PSE and PSE-3D. For the results presented here, the spanwise length is set to $L_z = 0.012\ m$ and the marching integration is begun at $x = 0.05094\ m$. The simulation is started with 5 linear PSE-3D steps before computing nonlinear interactions, replicating the same procedure followed with the NOLOT/PSE code. The marching step is constant and equal to $\Delta x = 0.001\ m$. The domain is discretized using $N_z = 16$ Fourier collocation points in the spanwise direction and $N_y = 121$ points in the wall-normal direction using FD-q8 scheme. Periodic boundary conditions are imposed in the spanwise direction, and the computed two-dimensional amplitude functions are Fourier transformed in spanwise direction to make detailed comparison possible.

Figure 5.2 shows comparison of nonlinear PSE-3D results using the relations (5.13)-(5.15) and those given by the NOLOT/PSE code. Discrepancies are observed mainly for the spanwise Fourier harmonics. The difference between Figures 5.2a and 5.2b is the number of modes considered for the marching integration. While in Figure 5.2a the decomposition of equation (5.11) is used, results in Figure 5.2b are computed with an additional mode, $\hat{\mathbf{q}}^h$, which is fed by the harmonic nonlinear terms following the same idea of equations (5.13)-(5.15). This mode is initialized by local 2β-mode. Thanks to this, an additional normalization condition is used for the harmonics, instead of imposing the α of the fundamental mode for all the harmonics. The results were further improved by using a larger number of spanwise modes, but it drastically increased the computational cost making the method inefficient.

A solution to this problem is found using a non-orthogonal coordinate system, which makes it possible to integrate the equations along the trajectory of the instability wave. The procedure implies a translation of the axis

$$x = \xi, \quad y = \eta, \quad z = \zeta + \xi \tan(\theta(\xi)), \tag{5.16}$$

where ξ, η and ζ are the computational coordinates, and $\theta = -\tan^{-1}(\alpha_{lin}(\xi)/\beta)$, being $\alpha_{lin}(\xi)$ the streamwise wavenumber resulting from running the linear PSE or PSE-3D.

(*a*) (*b*)

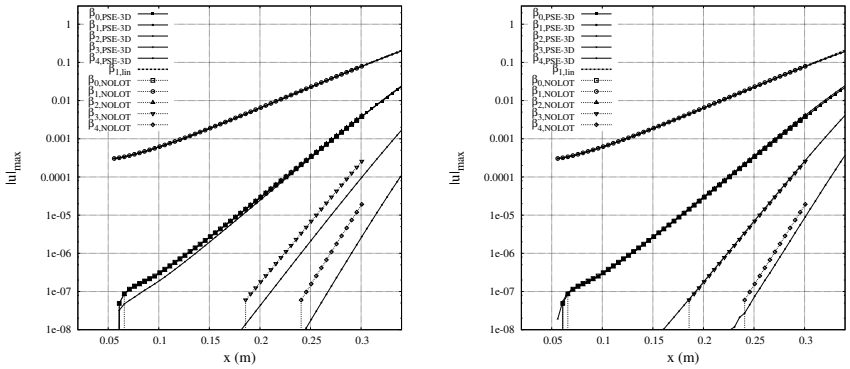

Figure 5.2: Evolution of spanwise Fourier modes using linear and nonlinear PSE-3D, in which a different number of modes are integrated along the streamwise direction, and nonlinear PSE (NOLOT) codes. (a) Using $\hat{\mathbf{q}}^0$, $\hat{\mathbf{q}}$ and $\hat{\mathbf{q}}^+$. (b) Using $\hat{\mathbf{q}}^0$, $\hat{\mathbf{q}}$, $\hat{\mathbf{q}}^+$, $\hat{\mathbf{q}}^h$ and $\hat{\mathbf{q}}^{h+}$.

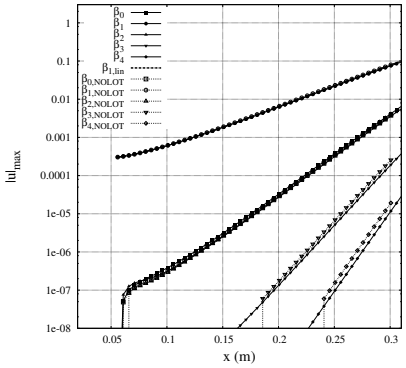

Figure 5.3: Evolution of different spanwise Fourier modes obtained by integration of only one mode along the trajectory of fundamental linear crossflow vortices. Nonlinear PSE (NOLOT code) results are also plotted for comparison

Using this coordinate transformation, the direction of the wave is aligned with the marching integration and no normalization condition needs to be imposed. Therefore, only a single stationary mode is integrated in a similar manner as in the streak problem described earlier. A very good agreement with nonlinear PSE results is found. This is shown in Figure 5.3, where the evolution of the maximum amplitude of streamwise velocity is plotted for the spanwise Fourier modes, $\beta_m = m\beta$ with $m = 1$, 2, 3 and 4.

Chapter 6

The LiGHT Code

The *Li*near *G*lobal instability for *H*ypersonic *T*ransition (*LiGHT*) code is an in-house Fortran suite of subroutines for the massively parallel solution of multi-dimensional complex non-symmetric eigenvalue problems (EVP) and Singular Value Decomposition (SVD) problems arising in global linear fluid flow instability. In the high supersonic and hypersonic regimes of interest, these eigenvalue problems result in dense matrices. The ScaLAPACK library (Blackford et al. 1997), available as part of vendor-optimized libraries on most modern supercomputers, including the DoD Open Research facility *Copper* (n.d.) and the UK open research supercomputer *Archer* (n.d.) is used to perform a full distributed LU-decomposition, as required by the shift-and-invert strategy implemented in equation (4.26) which promote physically-interesting and suppress spurious eigenmodes. The distribution of the matrices, the iterative generation of Krylov subspaces, the computation of the Ritz vectors and the Singular Value Decomposition are all performed by linear algebra operations distributed over the available processors, in either real or complex arithmetic. The computation of the Ritz values, which represents a negligible part of the overall computing effort, is performed serially in a post-processing step. Implementational details follow.

6.1 Spatial discretization using spectral collocation

Spatial discretization of the linearized Navier-Stokes operators have been demonstrated in the literature using low- or high-order finite-differences, finite-volume, finite element, spectral collocation or spectral element methods. Invariably, low-order methods require high-resolution grids to obtain reliable results. In a matrix-forming context, such as that used presently, unless sparse matrix storage is used, a high-order method is preferable. On the other hand, sparse storage is not exploited presently since the matrix multiplication (4.31) on which the formation of the SVD matrix is based would destroy any sparsity pattern that matrix $\mathbf{C}$ or its adjoint $\mathbf{C}^*$ may have. On account of these considerations, spatial discretization is performed by spectral collocation methods based on the standard Chebyshev Gauss-Lobatto (CGL) points (Canuto et al. 1988, Boyd 1989)

$$y_j = \cos\left(\frac{\pi j}{N}\right), \qquad j = 0, .., N, \tag{6.1}$$

defined on the standard interval [-1,1]. This numerical discretization method is known to offer highest resolution power on the lowest number of discretization nodes compared with any alternative (e.g. Paredes, Hermanns, Clainche and Theofilis 2013).

A variety of mappings are used to transfer data from the standard CGL domain to the physical domain of interest. Examples include a simple linear mapping or boundary-layer types of mappings which cluster points near a wall, such as the well-tested analytical transformation

$$\eta_j = a\frac{1+y_j}{b-y_j}, \tag{6.2}$$

where

$$a = \frac{\eta_j \eta_{max}}{\eta_{max} - 2\eta_j} \qquad \text{and} \qquad b = 1 + \frac{2a}{\eta_{max}}.$$

An arbitrary function defined in the CGL grid can be approximated by its Chebyshev expansion:

$$f(y) = \sum_{n=0}^{N} a_n \mathcal{T}_n(y) \tag{6.3}$$

with $\mathcal{T}_n(y) = \cos(n\ \cos^{-1}(y))$.

Differentiation on the CGL grid can be performed by application of the collocation differentiation matrix, $\mathcal{D}$

$$\left(\frac{df}{dy}\right)_i = \sum_{j=0}^{N} \mathcal{D}_{ij} f_j, \tag{6.4}$$

where

$$\mathcal{D}_{i,j} = \begin{cases} \frac{2N^2+1}{6}, & i = j = 0, \\ -\frac{y_j}{2(1-y_j^2)}, & i = j \neq 0, N \\ \frac{\overline{c}_i}{\overline{c}_j} \frac{(-1)^{i+j}}{y_i - y_j}, & i \neq j \\ -\frac{2N^2+1}{6}, & i = j = N \end{cases} \tag{6.5}$$

where

$$\overline{c}_j = \begin{cases} 2, & j = 0 \text{ or } j = N, \\ 1, & 1 \leq j \leq N-1 \end{cases} \tag{6.6}$$

Introducing the inner product

$$(f, g) = \sum_{i=0}^{N} b_i f(y_i)\ g(y_i), \tag{6.7}$$

with b_0=b_N=1/2, b_i=1 for the interval $0 < i < N$ and with y_i as the location of the extrema of the N^{th} Chebyshev polynomial

$$y_i = \cos\left(\frac{i\pi}{N}\right), \qquad i = 0, 1, ...N, \tag{6.8}$$

it can be shown that

$$(T_m(y), T_n(y)) = \begin{cases} 0, & \text{if } m \neq n, \\ N, & \text{if } m = n = 0 \text{ and } N, \\ \frac{N}{2}, & \text{if } m = n \neq 0 \text{ and } N. \end{cases} \tag{6.9}$$

Thereby, the coefficients a_n are defined as

$$a_n = \frac{c_n}{N} \sum_{i=0}^{N} b_i f(y_i) T_n(y_i) \tag{6.10}$$

where c_0=c_N=1 and c_n=2 for the interval $0 < n < N$. The function can thus be integrated with spectral accuracy using the relation

$$\int_{-1}^{1} f(y)dy = \sum_{i=0}^{N} f(y_i)\mathcal{W}(y_i), \tag{6.11}$$

where $\mathcal{W}$ is the Chebyshev integral weight function and it can be found as

$$f(y) = \sum_{n=0}^{N} a_n T_n(y) = \sum_{n=0}^{N} c_n T_n(y) \sum_{i=0}^{N} \frac{b_i}{N}\ f(y_i)T_n(y_i). \tag{6.12}$$

Integrating the above expression over y leads to

$$\int_{-1}^{1} f(y)dy = \frac{1}{N}\ \sum_{i=0}^{N} b_i f(y_i) \sum_{n=0}^{N} c_n T_n(y_i) \int_{-1}^{1} T_n(y)dy. \tag{6.13}$$

Finally, one can write

$$\int_{-1}^{1} T_n(y)dy = \begin{cases} 0, & \text{if } n \text{ is odd,} \\ \frac{2}{(1-n^2)}, & \text{if } n \text{ is even .} \end{cases} \tag{6.14}$$

with

$$\mathcal{W}(y_i) = \frac{b_i}{N}\ \left\{ 2 + \sum_{n=2}^{N} c_n \frac{(1+(-1)^n)}{(1-n^2)} \cos\left(\frac{ni\pi}{N}\right) \right\}. \tag{6.15}$$

This leads to a expression $\mathcal{W}$ containing the integration weights to compute the integral on the interval [-1,1]. However, since a mapping is used to map the physical domain onto the CGL interval, equation (6.15) is replaced by

$$\mathcal{W}(y_i) = \frac{b_i}{N} \sum_{n=0}^{N} c_n \cos\left(\frac{ni\pi}{N}\right) \int_{-1}^{1} T_n(y) \frac{d\eta}{dy} dy. \tag{6.16}$$

6.2 Formation of the discretized LNSE using the Kronecker product and Kronecker addition

The Kronecker product plays a key role in forming the matrix eigenvalue problem in multiple spatial dimensions. Its associative multiplication property makes the extension of the Kronecker product to higher dimensions straightforward. It also permits a simple construction of the linearized Navier-Stokes operator, or indeed the spatial discretization of any linear system of the form

$$\sum_{j=1}^{N_{\text{eq}}} \sum A_{ij} = \sum_{j=1}^{N_{\text{eq}}} \sum A_{ij} \tag{6.17}$$

including introduction of the base flow and its derivatives, as will be discussed shortly.

Formation of the linearized operator is also transparent to the details of the differentiation matrix used, making a Kronecker-product based strategy both flexible and general: distinct spatial differentiation schemes and the corresponding differentiation matrices may be defined independently along each direction, using the Kronecker product to construct tensor product grids in two or three spatial dimensions. In case a spatial direction is inhomogeneous,

it may be discretized by typical (Chebyshev or Legendre) spectral collocation differentiation matrices based on Jacobi polynomials, although any differentiation operator that can be written in matrix form, such as low- or high order standard or compact finite-differences, may be used. If the spatial direction in question is homogeneous, Fourier collocation derivative matrices may be used to discretize it, although a flow instability problem in which homogeneous spatial directions exist can be reduced to one described by differential equations of lower order.
In general, if $\mathbf{A} \in \mathbb{C}^{P\times Q}$, $\mathbf{B} \in \mathbb{C}^{R\times S}$, the Kronecker product $\mathbf{A}\otimes\mathbf{B}$ is defined as the rectangular matrix $\mathbf{C} \in \mathbb{C}^{PR\times QS}$

$$\mathbf{C} \equiv \mathbf{A}\otimes\mathbf{B} = \begin{pmatrix} a_{11}\mathbf{B} & a_{12}\mathbf{B} & \cdots & a_{1q}\mathbf{B} \\ a_{21}\mathbf{B} & a_{22}\mathbf{B} & \cdots & a_{2q}\mathbf{B} \\ \vdots & \vdots & \ddots & \vdots \\ a_{p1}\mathbf{B} & a_{p2}\mathbf{B} & \cdots & a_{pq}\mathbf{B} \end{pmatrix}.$$

In compact form, the elements $a_{p,q}$, $b_{r,s}$ and $c_{\mu,\nu}$ of matrices $\mathbf{A},\mathbf{B}$ and $\mathbf{C}$ are related by the identity

$$c_{\mu,\nu} = c_{\{(p,q);(r,s)\}} = c_{R(p-1)+r,S(q-1)+s} = a_{p,q}b_{r,s}. \tag{6.18}$$

indicating that element (μ,ν) is found at position (r,s) of block (p,q). The following properties are of interest, where $+$ is the common addition:

$$\mathbf{A}\otimes(\mathbf{B}+\mathbf{C}) = \mathbf{A}\otimes\mathbf{B} + \mathbf{A}\otimes\mathbf{C}, \tag{6.19}$$
$$(\mathbf{A}+\mathbf{B})\otimes\mathbf{C} = \mathbf{A}\otimes\mathbf{C} + \mathbf{B}\otimes\mathbf{C}, \tag{6.20}$$
$$(k\mathbf{A})\otimes\mathbf{B} = \mathbf{A}\otimes(k\mathbf{B}) = k(\mathbf{A}\otimes\mathbf{B}), \tag{6.21}$$
$$(\mathbf{A}\otimes\mathbf{B})\otimes\mathbf{C} = \mathbf{A}\otimes(\mathbf{B}\otimes\mathbf{C}) \tag{6.22}$$

In the particular case of square matrices $\mathbf{A}$ and $\mathbf{B}$ with leading dimensions P and R respectively, Kronecker addition, $\oplus$, is defined as

$$\mathbf{A}\oplus\mathbf{B} = \mathbf{A}\otimes\mathbf{I}_R + \mathbf{I}_P\otimes\mathbf{B}. \tag{6.23}$$

6.3 Distributed matrix construction

Spectral collocation can be used to discretize the multi-dimensional multi-dimensional EVP or SVD. A key element in a matrix forming framework is use of the Kronecker product. If (Nx, Ny, Nz) nodes discretize the (x, y, z) spatial directions and differentiation along these directions is performed by matrices $D_x \in C^{Nx\times Nx}$, $D_y \in C^{Ny\times Ny}$ and $D_z \in C^{Nz\times Nz}$, then coupled discretization of $\mathcal{L}_{1d}, \mathcal{L}_{2d}$ and $\mathcal{L}_{3d}$ may be represented by a matrix $\mathbf{A} \in C^{Ny\times Ny}$, $C^{(Nx\times Ny)\times(Nx\times Ny)}$, and $C^{(Nx\times Ny\times Nz)\times(Nx\times Ny\times Nz)}$, respectively. The building block for $\mathcal{L}_{1d}$ is D_y itself, while those for $\mathcal{L}_{2d}$ and $\mathcal{L}_{3D}$ are the Kronecker products $D_x\otimes D_y$ and $D_x\otimes D_y\otimes D_z$, respectively. In other words, the size of $\mathbf{A}$ pertinent to one-dimensional eigenvalue problem is $16\times(Ny)^2$, while that of two- and three-dimensional are $16(Nx\times Ny)^2$ and $16(Nx\times Ny\times Nz)^2$, respectively. The pre-multiplying factor 4^2 arises from the number of equations solved in incompressible flow and becomes 5^2 if instability of compressible flow is addressed and $(5+m)^2$ in hypersonic flow in which m equations are used to describe chemistry.

6.4 Parallelization strategy

The preceding discussion highlights the need for a distributed solution of large-scale global eigenvalue problems. Simple calculations of the size of the matrices involved in temporal and especially spatial BiGlobal analysis as well as that discretizing the TriGlobal EVP suggest that *off-the-shelf* parallelization of the formed matrix using

OpenMP libraries and multithreading (Paredes, Hermanns, Le Clainche and Theofilis 2013, Paredes et al. 2016a) is not a viable approach.

In the *LiGHT* code an alternative path has been chosen, namely dense treatment of the matrix and its distribution over a large number of processors, using the well-tested ScaLAPACK library (Blackford et al. 1997), which is optimized on native libraries available on supercomputers of the Cray XE6m family, such as Copper *Copper* (n.d.) and Archer *Archer* (n.d.). Schematically, the process of distributing the matrices over n available processors and the implemented solution of the EVP is shown in figure 6.1. The master (green) is responsible to initialize and distribute the matrices A and B. The slaves (red) are responsible to run the Arnoldi algorithm and send the results back to the master, where a serial eigenvalue routine from Lapack is used to recover the final results.

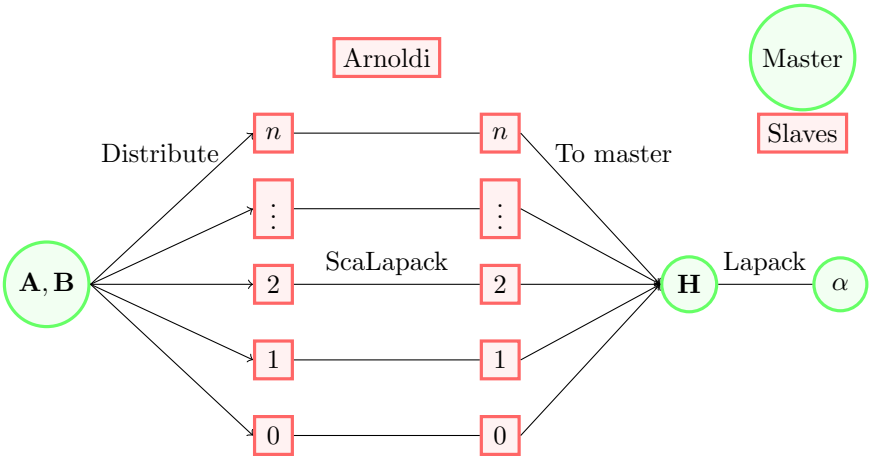

Figure 6.1: Distribution of the matrices in order to apply Arnoldi algorithm with ScaLapack and solve the Hessenberg matrix in a single node using Lapack.

In ScaLAPACK, the discretized block matrix generated is stored over several processors of a cluster, and, using distributed memory parallel computers, the maximum dimension of the problem is determined by the number of available processors. The two common issues in the matrix forming approach are expected to be alleviated with parallelization. The first is the memory restriction due to the storage of the matrix. The second is the CPU time limitations imposed by a serial solution of the EVP. ScaLAPACK and PBLAS are used to perform linear algebra operations in parallel while BLACS is used to set the communication (Blackford et al. 1997). These libraries have been documented to work scalable with dense matrices of leading dimension $O(10^5)$ on clusters featuring $O(10^4)$ processors (Borrill 1999).

ScaLAPACK is based on the BLACS layers, which handles MPI or PVM parallel communication and uses BLAS for linear algebra operations (PBLAS in the parallel form) (Theofilis 2007). Parallelization consists of three major steps. First, the BLACS library is initialized to be used in subsequent operations. Second, a rectangular processor grid is built using all available processors available. ScaLAPACK then creates an array descriptor vector for each global array and maps the global array elements among the processors following a two-dimensional block-cyclic distribution that gives the best load balance and maximum data locality for most of the ScaLAPACK algorithms (Blackford et al. 1997). The two-dimensional block cyclic distribution is accomplished by dividing the global array into blocks with a specific number of rows and columns, given by a parameter so called blocking factor (r), to be discussed shortly. This parameter can be different for rows and columns of an array, but normally an unique value is used due to the square property of the matrix. The distribution algorithm works independently on rows and columns.

6.5 Block-cyclic element distribution

Let the (row, column) coordinates of an element of the (global) matrix be described by the pair of indices $(i_{\text{glob}}, j_{\text{glob}})$, with $0 \leq i_{\text{glob}} \leq M-1$ and $0 \leq j_{\text{glob}} \leq N-1$. The block-cyclic distribution scheme is discussed for a rectangular global matrix, $M \neq N$, although the eigenvalue problem is subsequently solved for square matrices, $M = N$. However, the ability to distribute rectangular matrices will be useful in future extensions of the present work, dealing with the singular value decomposition of matrices arising in non-modal global linear instability analysis (Theofilis 2011a).

Let the number of available processes be arranged into a two-dimensional grid, $P \times Q$, and let (p, q) describe the coordinates of the processor within which global element $(i_{\text{glob}}, j_{\text{glob}})$ is found, with $0 \leq p < P-1$ and $0 \leq q < Q-1$. Again, the discussion of block-cyclic distribution is offered for $P \neq Q$, although solution of the eigenvalue problem in ScaLAPACK will require $P = Q$.

Finally, let $r \times c$ be the row and column blocking factors, respectively, which determine the size of the blocks within each process, and let (b, d) be the local block coordinates within process identified by the indices (p, q).

The local coordinates $(i_{\text{loc}}, j_{\text{loc}})$ of global element $(i_{\text{glob}}, j_{\text{glob}})$ within process (p, q) and block (b, d) are determined by the following mapping of the global index i_{glob} to a triplet $\langle p, b, i_{\text{loc}} \rangle$ and of global index j_{glob} to a triplet $\langle q, d, j_{\text{loc}} \rangle$, i.e.

$$(i_{\text{glob}}, j_{\text{glob}}) \quad \mapsto \quad \langle (p, q), (b, d), (i_{\text{loc}}, j_{\text{loc}}) \rangle. \tag{6.24}$$

Here

$$(p, q) = \left(\left\lfloor \frac{i_{\text{glob}}}{r} \right\rfloor \bmod (P), \left\lfloor \frac{j_{\text{glob}}}{c} \right\rfloor \bmod (Q) \right), \tag{6.25}$$

$$(b, d) = \left(\left\lfloor \frac{i_{\text{glob}}}{rP} \right\rfloor, \left\lfloor \frac{j_{\text{glob}}}{cQ} \right\rfloor \right), \tag{6.26}$$

$$(i_{\text{loc}}, j_{\text{loc}}) = (i_{\text{glob}} \bmod (r), j_{\text{glob}} \bmod (c)), \tag{6.27}$$

$m \bmod (n)$ is the `modulo` function and $\lfloor m \rfloor$ is the integer `floor` function.
The inverse mapping of the triplet $\langle (p, q) i, (b, d), (i_{\text{loc}}, j_{\text{loc}}) \rangle$ to the global indices $(i_{\text{glob}}, j_{\text{glob}})$ is defined by

$$\langle (p, q), (b, d), (i_{\text{loc}}, j_{\text{loc}}) \rangle \quad \mapsto \quad (r(p + bP) + i_{\text{loc}}, c(q + dQ) + j_{\text{loc}}) \tag{6.28}$$

$$\equiv \quad (i_{\text{glob}}, j_{\text{glob}}) \tag{6.29}$$

An element $(i_{\text{glob}}, j_{\text{glob}})$ in a global rectangular matrix of dimension (M, N) acquires local coordinates $(i_{\text{loc}}, j_{\text{loc}})$ which depend on the number of processes, (P, Q), used to distribute the global matrix and on the (row, column) blocking factor values (r, c). Knowledge of these data permits computation of the local indices using equations (6.25-6.27). Conversely, if the local indices, as well as (P, Q) and (r, c) are known, equations (6.25-6.26) and (6.28) can be used to identify the global array indices pertinent to the element in question.

An example of block-cyclic distribution of a square array with leading dimension $M = N = 16$ over four processes arranged in a $(P, Q) = (2 \times 2)$ process grid and using a blocking factor $r = c = 5$ is shown in Fig. 6.2. The left figure shows the matrix elements as seen from a global perspective, while the right figure shows the elements held by each process, identified by a unique color for each process.

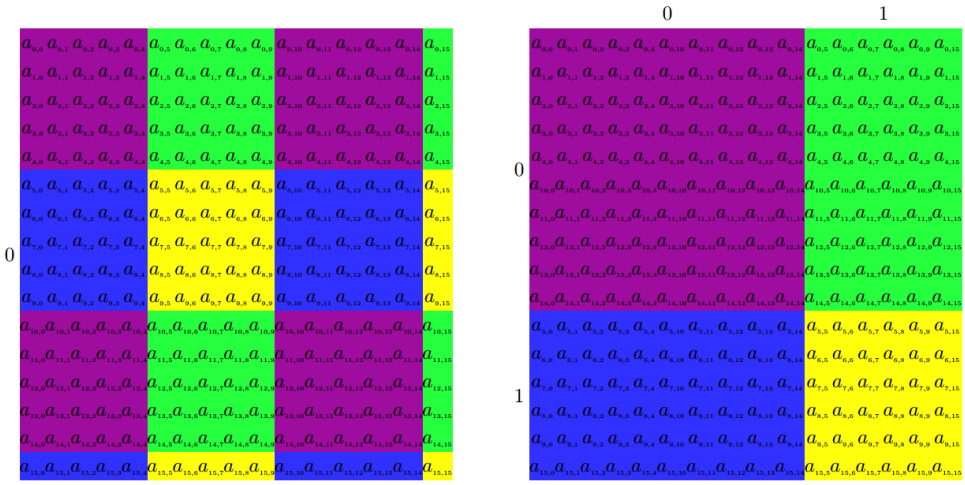

Figure 6.2: Distribution of a 16×16 array over a 2×2 processor grid using a block-cyclic scheme with a 5×5 blocking factor.

6.6 Scalability study

The following results were computed on two different machines: a "small" cluster with 64 cores featuring a AMD Opteron 6366 HE processor with 1.8 GHz and 16 Mb Cache L3, 512 Gb RAM with maximum memory bandwidth 51.2 GB/s and a "large" cluster namely the Copper Cray XE6m *Copper* (n.d.), with 460 nodes and 32 cores per node featuring a AMD Interlagos Opteron processor with 2.3 GHz and 16 Mb Cache L3, 60 GB of accessible memory per node and 51.2 GB/s of maximum memory bandwidth. The compiler used was GNU Fortran 4.8.3 (Red Hat 4.8.3-9).

The first task was to use the BLACS library in order to set the rectangular processor grid for instability analysis in a manner that is transparent to the cluster on which the code is running. The objective here was to distribute pieces of each matrices over the processors in the grid in an adequate manner, such that each process will always be busy doing roughly an equal number of calculations, meaning that load balancing is achieved (Blackford et al. 1997).

The local linear stability of the mixing layer/wake interaction problem was first performed in the small cluster. The number of processors used was based on the processor grid (2x2, 3x3, 4x4, 5x5, 6x6, 7x7 and 8x8). Figure 6.3 shows the comparison between the number of processors by matrix length. As can be observed, the speedup increases increasing the matrix order for all processors grid. This can be justified by the compensation between each process work and MPI communication. Different blocking factors were tested varying between 2 and 20. The blocking factor which gives the better CPU-time was 8 in all cases.

Finally, the Laplace equation was solved in the Cooper Cray XE6m machine, as a first step toward discretizing the viscous terms in the incompressible Navier-Stokes equations, while ensuring correct computation of the analytically-known eigenvalues.

Spectral collocation methods are used to discretize the square domain $x \in [-1, 1] \times y \in [-1, 1]$ using Nx = Ny = 401 Chebyshev Gauss Lobatto (CGL) nodes in each spatial direction. This results in a matrix with dim(A) = 160801, which occupies $\approx$ 413GB of memory in double precision real arithmetic. The matrix is distributed using 1282 blocks over processor grids of different sizes, as shown in fig. 6.4. Once the matrix is LU-decomposed by ScaLAPACK, the distributed Arnoldi algorithm is used to construct a Krylov subspace of dimension $m_{\text{Kryl}} = 200$ and compute the leading Ritz values.

In the same Figure 6.4 the linear scaling of the numerical solution of the Laplace EVP is shown, for the three different matrix sizes with the associated wall-clock time in seconds. Besides near-perfect linear scaling achieved

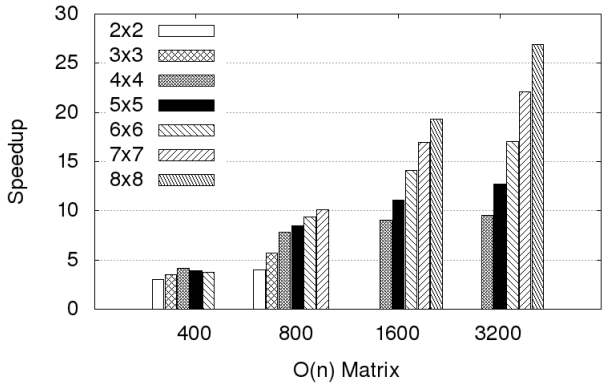

Figure 6.3: Speedup as function of the matrix order. The processors grid used are show in the graphic.

	Processor Grid	# CPUs	Element Distribution (s)	LU Decomposition (s)	Arnoldi Iteration (s)
201^2	8×8	64	182	140	80
	12×12	144	178	62	57
	16×16	256	172	47	50
	20×20	400	171	34	47
401^2	16×16	256	2800	1722	331
	20×20	400	2761	1142	256
	24×24	576	2735	956	229
	28×28	784	2710	698	206
	32×32	1024	2703	572	195
	36×36	1296	2690	431	195
	40×40	1600	2681	418	192
601^2	36×36	1296	13878	3985	514
	44×44	1936	13802	3421	505
	48×48	2304	13767	2389	435
	52×52	2704	13740	2144	433
	56×56	3136	13721	1885	416
	60×60	3600	13703	1814	409

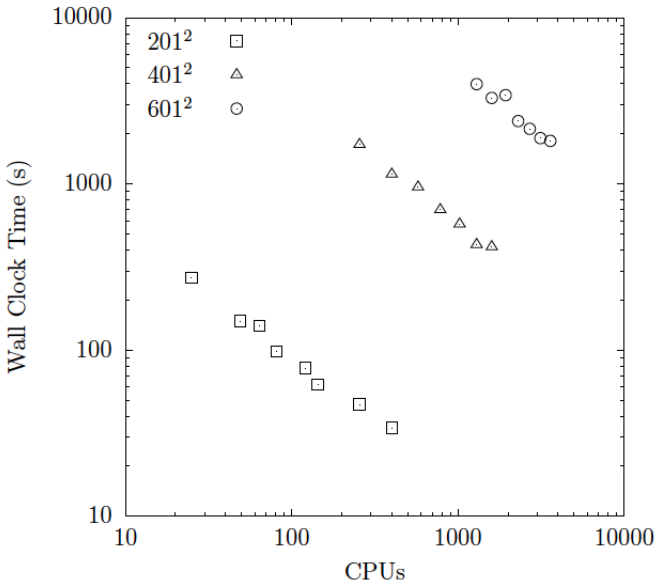

Figure 6.4: Scaling results for the solution of the two-dimensional Laplace EVP, discretized by $201^2, 401^2$ and 601^2 spectral collocation nodes and 128^2 blocks for the block cyclic distribution of matrix $\mathbf{A}$. *Resolution* 201^2: dim($\mathbf{A}$)=40401, size($\mathbf{A}$)=26.12 GB, min(#CPUs)= 14. *Resolution* 401^2: dim($\mathbf{A}$)=160801, size($\mathbf{A}$)=413.71 GB, min(#CPUs)= 220. *Resolution* 601^2:, dim($\mathbf{A}$)=361201, size($\mathbf{A}$)=2.087 TB, min(#CPUs)=1115.

for all resolutions when the number of CPUs is varied, the wall-clock time for the parallel numerical solution of the Laplace EVP (or a multi-dimensional flow stability EVP at analogous resolutions) is well acceptable, falling below 15 mins when O(1000) CPUs are used.

Chapter 7

Validations and Verifications

7.1 LiGHT code

7.1.1 Parallel solutions of two-dimensional eigenvalue problems

The 2D Laplace EVP

The two-dimensional Laplace eigenvalue problem

$$\nabla^2_{2\mathrm{D}} f + \lambda f = 0, \tag{7.1}$$

where $\nabla^2_{2\mathrm{D}} = \partial_{xx} + \partial_{yy}$, subject to homogeneous Dirichlet boundary conditions, is discretized as

$$\delta_{xx} \oplus \delta_{yy} \equiv \mathcal{D}^2_{xx} \otimes \mathbf{I_y} + \mathbf{I_x} \otimes \mathcal{D}^2_{yy} + \lambda \mathbf{I_x} \otimes \mathbf{I_y} = 0. \tag{7.2}$$

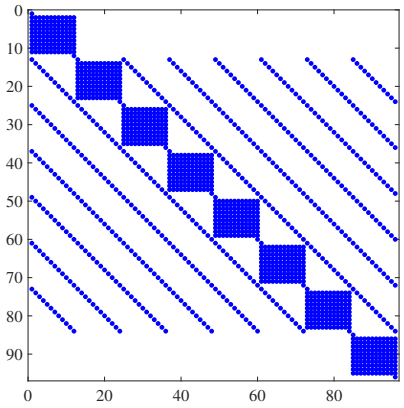

Figure 7.1: Sparsity pattern of the discrete two-dimensional Laplacian operator in (7.2)

Here $\mathcal{D}^2_{xx}$ and $\mathcal{D}^2_{yy}$ represent second-order differentiation matrices along the spatial directions x and y, respectively, while $\mathbf{I_x}$ and $\mathbf{I_y}$ are the corresponding identity matrices of appropriate dimensions. Rows are modified in the matrices in order to impose the boundary conditions prior to forming the Kronecker product. An example of the sparsity pattern of the discrete Laplacian resulting from discretization of (7.2) by dense differentiation matrices as well as 8 and 12 points along the x and y spatial directions, respectively, is shown in Figure 7.1.

The analytic eigenvalues of the two-dimensional Laplace eigenvalue problem (7.1), found by separation of variables, are

$$\lambda_{ij} = \left(\frac{i\pi}{a}\right)^2 + \left(\frac{j\pi}{b}\right)^2 \quad i,j = 1,2,\cdots \tag{7.3}$$

and have been recovered to machine precision by the LiGHT code. A randomly chosen eigenvector is shown in Figure 7.2.

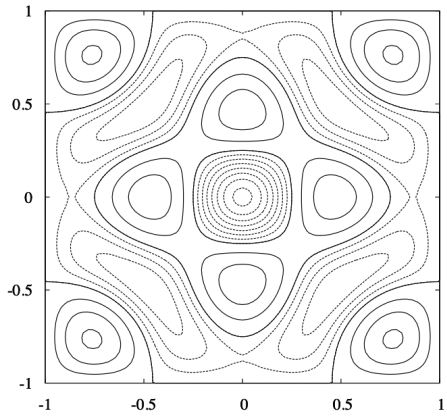

Figure 7.2: Two-dimensional eigenfunction in the numerical solution of (7.1)

The 2D Helmholtz EVP in elliptic confocal coordinates

In preparation for the numerical solution of the BiGlobal eigenvalue problem in elliptic confocal coordinates, the two-dimensional Helmholtz eigenvalue problem

$$\nabla^2 f = -\lambda^2 f, \tag{7.4}$$

is solved on these coordinate system. The orthogonal elliptic confocal transformation

$$x = c\ \cosh\eta\ \cos\xi, \qquad y = c\ \sinh\eta\ \sin\xi, \tag{7.5}$$

is used to transform a two-dimensional (ξ,η) plane at a given axial location on the elliptic cone onto a Cartesian domain (x,y). The parameters selected are for an ellipse of aspect ratio AR = 2, $\eta_0 = \text{atanh}(1/\text{AR}), \text{c} = \text{AR}/\sinh(\eta_0)$ and $\eta_R = \text{acosh}(10/\text{c})$. The domain is discretized using $N_\xi = 50$ Fourier collocation points along the azimuthal ξ direction and $N_\eta = 50$ Chebyshev Gauss Lobatto (CGL) points along the wall-normal direction η. Figure 7.3 shows results obtained, plotting, in the left part of the figure the relative error in the exact value of a randomly chosen eigenvalue using nine successive levels of grid refinement and $N = N_\xi = N_\eta$. The corresponding eigenvector is shown in the the right-hand-side of the same figure.

The 2D square lid-driven cavity

While the matrices discretizing the Laplace and Helmholtz eigenvalue problems were programmed and solved in parallel, the remaining part of validation work used matrices generated independently, read in LiGHT in parallel and their eigenvalues and eigenvectors were computed in parallel. Dr. Matthew Tufts (AFRL) is acknowledged for his contribution of subroutines reading matrices in parallel, which has significantly reduced the matrix generation time shown in the third column of the table contained in Fig. 6.4.

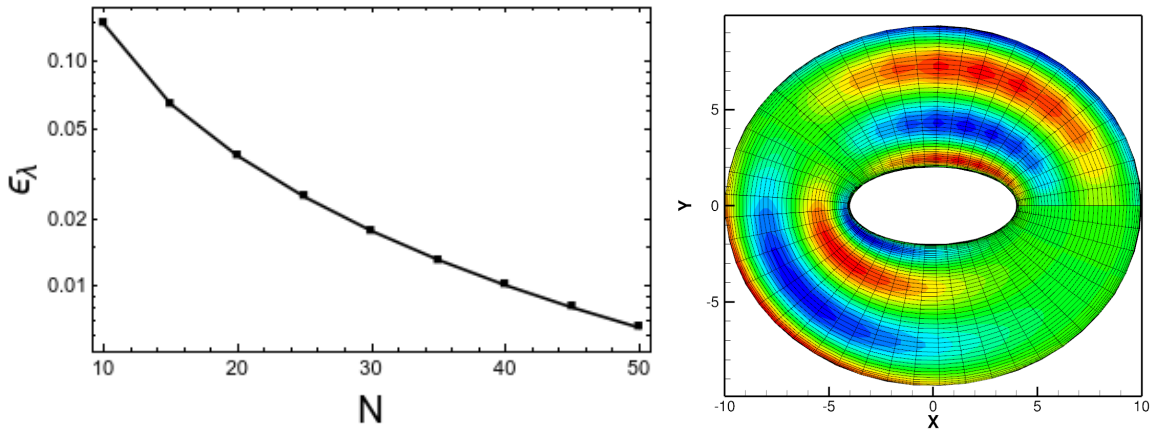

Figure 7.3: Convergence history and iso-contours of normalized eigenfunction of parallel numerical solution of (7.4) on the elliptic confocal grid (7.5)

The two-dimensional square lid-driven cavity was solved after regularizing the lid motion (Theofilis 2000, Albensoeder et al. 2001), which permits obtaining highly-accurate base flow solutions. The wavenumber vector in the stability analysis is normal to the plane on which the base flow develops and a transformation as performed by Theofilis (2003) reduces the two-dimensional EVP into one with real coefficients. The square domain is taken to be $\Omega = \{\{x \in [0,1]\} \times \{y \in [0,1]\}\}$. The base flow has two velocity components in these directions and is obtained by solving the vorticity equation (Theofilis 2003) . The boundary conditions are no-slip for all the stationary walls, while on the lid

$$\bar{u} = [1 - (2x-1)^{16}]^2, \quad x \in [0,1] \tag{7.6}$$

is imposed. All eigenvalues known from previous analyses using serial solvers are recovered in the parallel solution; Fig. 7.4 shows the leading eigenfunction at $Re = 1000$ and spanwise wavenumber $\beta = 15$.

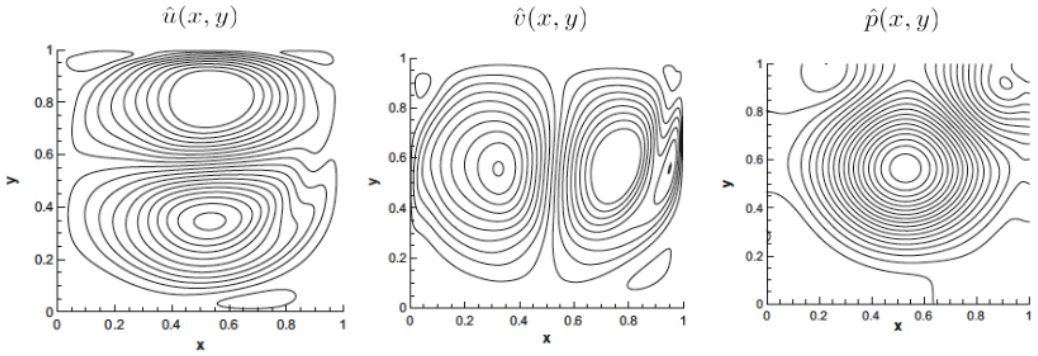

Figure 7.4: Eigenfunctions at $Re = 1000, \beta = 15$ corresponding to the leading eigenmode. Contour of both velocities $\hat{u}$ and $\hat{v}$ as well as the pressure $\hat{p}$ are presented.

7.1.2 Massively parallel 3D EVP solutions

The 3D Laplace EVP

The three-dimensional Laplace eigenvalue problem

$$\nabla^2_{3\mathrm{D}} f + \lambda f = 0, \tag{7.7}$$

where $\nabla^2 = \partial_{xx} + \partial_{yy} + \partial_{zz}$ is discretized as

$$\mathcal{D}^2_{xx} \otimes \mathbf{I_y} \otimes \mathbf{I_z} + \mathbf{I_x} \otimes \mathcal{D}^2_{yy} \otimes \mathbf{I_z} + \mathbf{I_x} \otimes \mathbf{I_y} \otimes \mathcal{D}^2_{zz} + \lambda \mathbf{I_x} \otimes \mathbf{I_y} \otimes \mathbf{I_z} = 0. \tag{7.8}$$

For the three-dimensional case, the Laplace eigenvalue problem (7.7) is solved in a parallelepiped $\Omega = \{\{x \in [0, a]\} \times \{y \in [0, b]\} \times \{z \in [0, a]\}\}$. The analytical solution can also be found using separation of variables; the eigenvalues of (7.7) are

$$\lambda_{ijk} = \left(\frac{i\pi}{a}\right)^2 + \left(\frac{j\pi}{b}\right)^2 + \left(\frac{k\pi}{c}\right)^2, \quad i, j, k = 1, 2, \cdots \tag{7.9}$$

while the corresponding eigenfunctions are

$$\Phi_{ijk}(x, y, z) = \frac{2^{\frac{3}{2}}}{\sqrt{abc}} \sin\left(\frac{i\pi x}{a}\right) \sin\left(\frac{j\pi y}{b}\right) \sin\left(\frac{k\pi z}{c}\right), \tag{7.10}$$

the constant in (7.10) ensuring mutual orthogonality of the eigenfunctions.
Equation (7.8) has been solved numerically and the analytical results have also been recovered to machine precision. This three-dimensional eigenvalue problem has been used to perform the scalability tests discussed in section 6.6 using the resolutions and processor grids discussed in Fig. 6.4. A randomly chosen three-dimensional eigenvector is shown in Fig. 7.5.

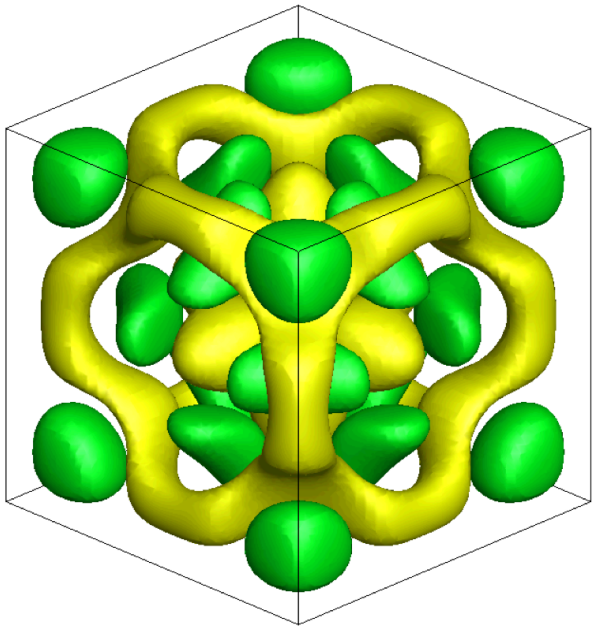

Figure 7.5: Three-dimensional eigenfunction in the numerical solution of (7.7)

The 3D cubic lid-driven cavity

In this well-studied fluid flow instability example (Gómez et al. 2012) the incompressible TriGlobal eigenvalue problem is solved for flow in a cubic regularized lid-driven cavity flow. The base flow has been computed with a DNS

solver by Theofilis (2017) in the domain $\Omega = \{\{x \in [0,1]\} \times \{y \in [0,1]\} \times \{z \in [0,1]\}\}$ at a stable Reynolds number value, $Re = 1000$. Once again, the well known eigenvalues are recovered and fig. 7.6 shows the eigenfunctions of the three velocity components and pressure for the leading eigenmode ($\omega = 0.461 + i\ 0.131$).

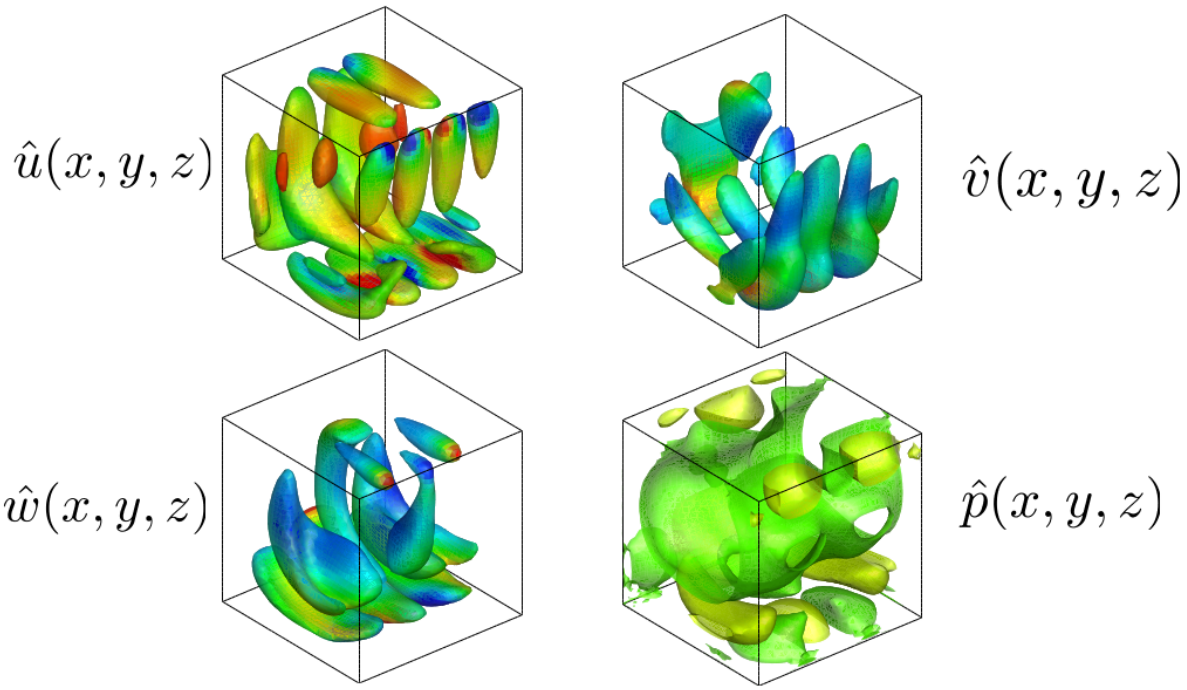

Figure 7.6: Eigenfunctions at Re = 1000 corresponding to the leading eigenmode.

7.1.3 Aeroelastic instability eigenvalue problem

Fluid-structure interaction can be studied by solving the eigenvalue problem (Timme et al. 2012, Timme and Badcock 2011)

$$\left[\mathcal{A}_{ss} - \mathcal{A}_{sf}\left(\mathcal{A}_{ff} - \mu\mathcal{I}\right)^{-1}\mathcal{A}_{fs}\right]\mathbf{x} = \mu\mathbf{x}, \tag{7.11}$$

in which the operators $\mathcal{A}_{ss}$ and $\mathcal{A}_{ff}$ respectively describe structure and fluid self-interaction, while operators $\mathcal{A}_{sf}$ and $\mathcal{A}_{fs}$ describe flow-structure coupling. Analytic transformations convert this problem into the real three-dimensional generalized eigenvalue problem

$$(\mathcal{A} + \sigma\mathcal{B})\mathbf{x} = \lambda\mathcal{M}\mathbf{x}, \tag{7.12}$$

which has been solved by Timme and Badcock (2011). At a given resolution, the matrix which discretizes the operator $\mathcal{A}$ in (7.12) has a leading dimension $dim((A)) = 16390$, the number of its non-zero elements is $nz = 627979$ and the sparsity pattern is shown in the left part of Figure 7.7. The solution obtained using a modest Krylov subspace dimension of $m_{\text{Kryl}} = 100$ in the LiGHT code, which does not exploit the sparsity pattern of the matrix, but treats it as dense, as well as the comparison of the present parallel EVP solution with the reference solution of Timme and Badcock (2011) is shown in the right part of the same figure. The excellent agreement between the two sets of results for the least damped eigenmode having frequency $\lambda_r \approx 0.3$ as well as all significant eigenvalues in the vicinity of the right-half plane is clearly visible in these results. Increasing the subspace dimension permits capturing additional (strongly damped) eigenvalues in the parallel solution.

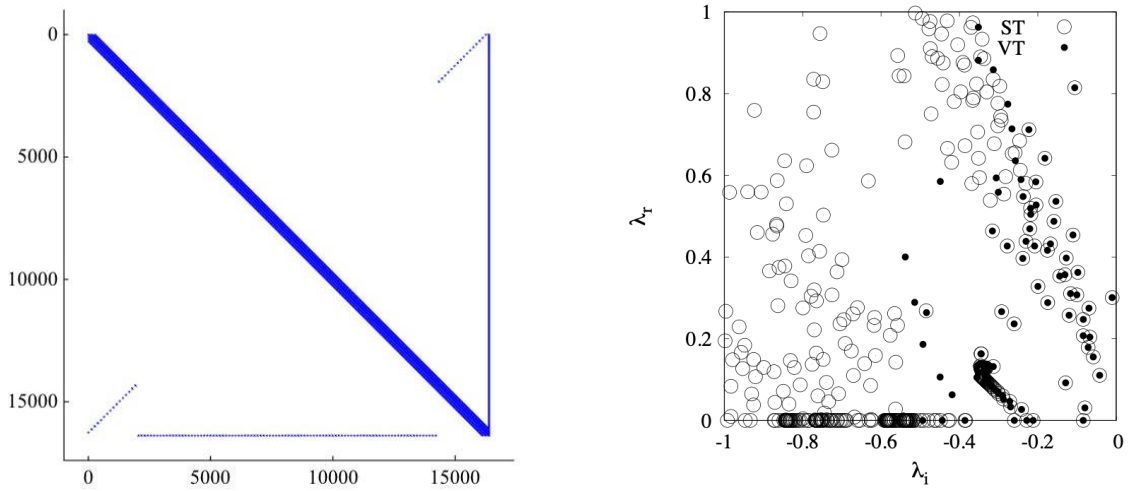

Figure 7.7: *Left:* Sparsity pattern of the aeroelasticity matrix (Timme and Badcock 2011). *Right:* Comparison of the iterative serial reference solution (open symbols) with the parallel solution obtained using LiGHT

7.1.4 Global instability on a three-dimensional wing

Collaborative work in progress, supported by AFOSR grant FA9550-17-1-0222 "Flow Physics and Control of 3-D Separation on 3-D Swept Wings", has provided an additional validation case for the LiGHT code, namely the matrix discretizing the incompressible three-dimensional global linear instability of flow around a three-dimensional wing presented by Taira and Colonius (2009). The leading dimension of the matrix is $dim((A)) = 276645$, the number of non-zero elements is $nz = 2291612$ and its sparsity pattern is shown in Figure 7.8. Work in this area is underway and first results will be reported as they become available.

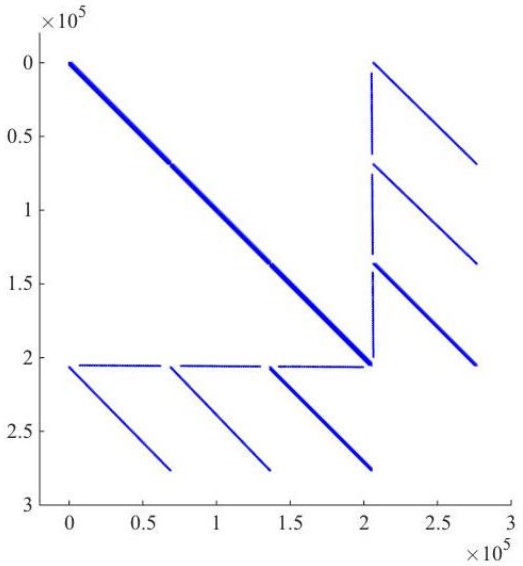

Figure 7.8: Sparsity pattern of the matrix discretizing the three-dimensional incompressible linearised Navier-Stokes equations (Taira and Colonius 2009)

7.2 Local transient growth

While transient growth ideas are well-developed in (in)compressible boundary layer type of flows, global transient growth work has only presently started appearing in the hypersonic flows literature (Paredes et al. 2017a,b, 2018). Here validations of the codes developed are shown in the classic flat-plate boundary layer at incompressible and compressible conditions.

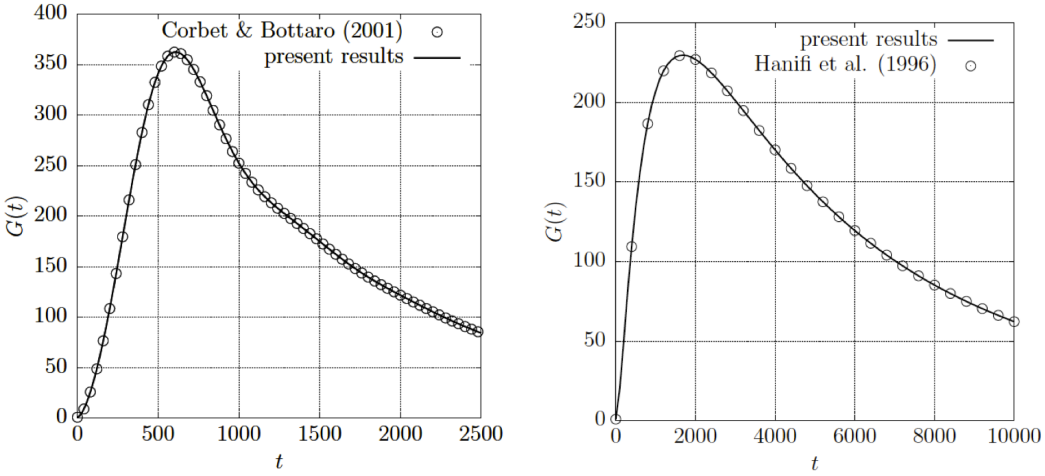

Figure 7.9: Gain as a function of time in the Blasius (left) and compressible (right) flat-plate boundary layer

Figure 7.9 shows the time-evolution of the gain function, $G(t)$, for the Blasius boundary layer at momentum-thickness Reynolds number $Re_\theta = 166$, streamwise wavenumber $\alpha = 0.0142$ and spanwise wavenumber $\beta = 0.2327$ (Corbett and Bottaro 2001b, Fig. 3) as well as for the compressible flat-plate boundary layer at $Ma = 2.5$, displacement-thickness based Reynolds number $Re_{\delta^*} = 300$ and streamwise aligned periodic waves with $\alpha = 0, \beta = 0.1$ (Hanifi et al. 1996b, Fig. 4). In both cases the agreement between the present results (full lines) and those of the respective reference works (symbols) is excellent. From a physical point of view it can be argued that both in the incompressible and in the supersonic boundary layer, the energy growth at the parameters chosen is too feeble for transient growth to be considered as a relevant laminar-turbulent transition scenario.

7.3 Compressible BiGlobal EVP

7.3.1 Instability of flow in the swept leading edge boundary layer

Instability in the vicinity of the swept leading edge in compressible flow has been studied in a global modal analysis context by Lin and Malik (1995), with a number of authors having contributed aspects of flow instability physics since (Theofilis et al. 2004, Mack et al. 2008, Gennaro et al. 2013). This problem is interesting as a validation case of the eigenvalue problem solver since, even within the limitations of the simplified base flow model used in analysis (Rosenhead 1963), all three base flow velocity components are present and no reductions of the Linearized Navier-Stokes equations are possible.

The compressible temporal BiGlobal stability analysis EVP has been solved at Mach number $Ma = 0.9$ and Reynolds number $Re = 800$ for a number of values of the spanwise wavenumber, β, indicating harmonic linear modal perturbations along the leading edge. A linear mapping of the chordwise direction has been used, while the boundary-layer mapping (6.2) has been used to discretize the wall-normal direction; all solutions were obtained on a mesh using $N = 70$ in both directions. The boundary conditions used are no-slip on the perturbation velocities and homogeneous Dirichlet for the temperature at the wall. A fast decay in the wall-normal direction is assumed here

for all disturbances at large enough distance from the wall (y_∞=100). Along the chordwise direction, at a large distance from the attachment-line (x=$\pm L_x$=100), a linear extrapolation from the interior of the computational domain is used.

For the wavenumber shown here, $\beta = 0.19$ delivers the most unstable Görtler-Hämmerlin (GH), first symmetric mode, the eigenvalue of which is found to be $\omega = 0.0765392 + i\ 0.00117793$; the corresponding result of Gennaro et al. (2013) is $\omega = 0.0764718 + i\ 0.00118942$, obtained using $N = 140$ to discretize either of the two spatial directions. Figure 7.10 shows the real and imaginary part of the amplitude functions $\hat{u}, \hat{w}$ and $\hat{T}$ of the GH mode.

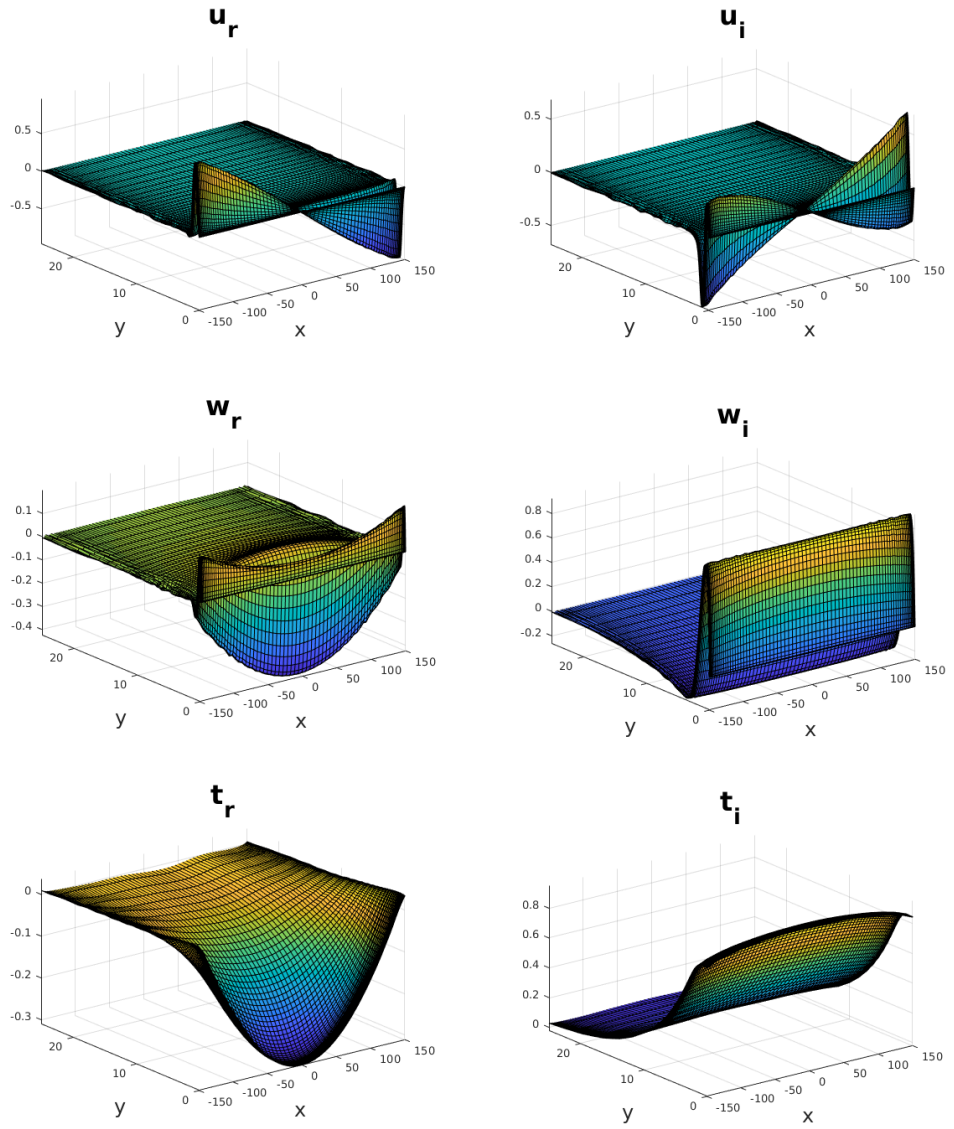

Figure 7.10: Amplitude functions at $Ma = 0.9, Re = 800$ and $\beta = 0.19$ corresponding to the most unstable (GH) mode. On the left-hand-side are the real and on the right-hand-side the imaginary part of $\hat{u}$, $\hat{w}$ and $\hat{T}$, respectively

Chapter 8

Transient Growth of Hypersonic Flow on the Elliptic Cone

8.1 Local non-modal stability analysis

Non-modal linear stability analysis results have first been obtained on the elliptic cone within a local analysis framework. The nomenclature of the geometry considered is shown in Figure 8.1, where the azimuth angle θ is defined such that $\theta = 0°$ refers to the attachment-line at the major semi-axis of the cone, $\theta = 90°$ is the centerline at the minor semi-axis, while $0° < \theta < 90°$ is the range in which crossflow instability may be encountered. Two fundamentally different flow situations were considered, both at the same free stream Mach number $Ma = 7$ but at different altitudes, $h = 33km$ and $h = 21km$, at which the unit Reynolds numbers are one order of magnitude different, $Re_1 = 1.89 \times 10^6$ m^{-1} and $Re_1 = 1.015 \times 10^7$ m^{-1}, respectively.

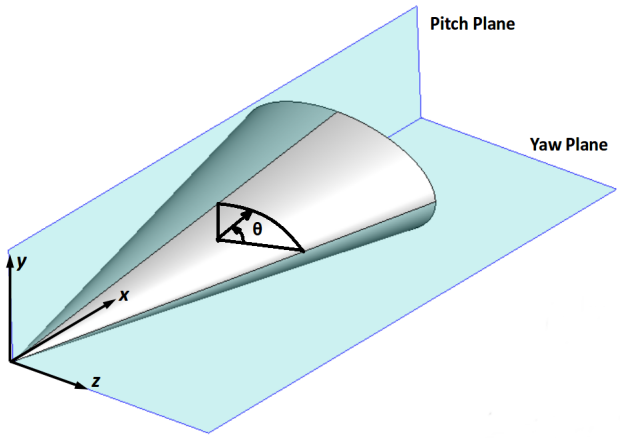

Figure 8.1: Geometry and coordinate system on the elliptic cone

Local non-modal analysis was carried out by extracting velocity, temperature, pressure and density profiles from the steady base flow, as schematically shown in Fig. 8.2, and performing $\epsilon-$pseudospectrum analysis of these profiles. Results representative of those obtained at all locations on the cone surface are shown at an arbitrarily chosen location $x = 0.4m, \theta = \pi/4$ in Figure 8.3. The eigenspectrum of two different cases is shown, in the first of which the wavenumber $\alpha \neq 0$ whereas in the second case $\alpha = 0$; in both cases the wavenumber a nonzero $\beta \neq 0$ is chosen. This implies that the analysis of the first case corresponds to oblique two-dimensional perturbations, while

in the second case the linear non-modal evolution of streamwise aligned structures of distinct spanwise spacing, $L_z = 2\pi/\beta$, is examined.

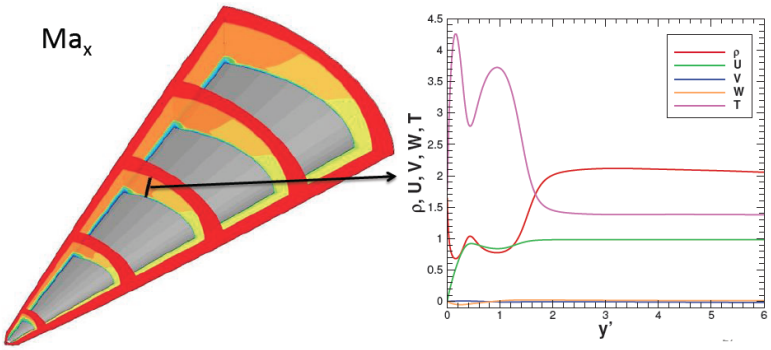

Figure 8.2: One-dimensional profiles extracted from the base flow at a given location on the cone surface, between the centerline and the attachment-line

In the case of oblique perturbations, shown in the leftmost two plots of Fig. 8.3, both amplified, $\omega_i > 0$, and damped, $\omega_i < 0$, eigenmodes are recovered, while the $\epsilon-$pseudospectrum shows that, for both β values examined, rather large levels of matrix perturbations are required to lead to zero crossing of the stable perturbations. In other words, the underlying linearized Navier-Stokes operator is normal and laminar-turbulent transition is to be expected on account of exponential amplification of unstable modal perturbations. By contrast, in the case of streamwise-aligned perturbations, shown in the rightmost two plots of Fig. 8.3, only stable eigenmodes $\omega_i < 0$ are found and, most significantly, matrix perturbations of very small amplitude suffice to lead to substantial excursions into the positive ω_i half-plane. The implication is that hypersonic flow over an elliptic cone at the conditions examined can be sensitive to strong algebraic growth of streamwise-aligned perturbations. This point will be examined in detail in what follows, and will be revisited in section 8.1.3, where qualitative comparisons will be made with the only ground experiment data available to-date that is amenable to such comparisons.

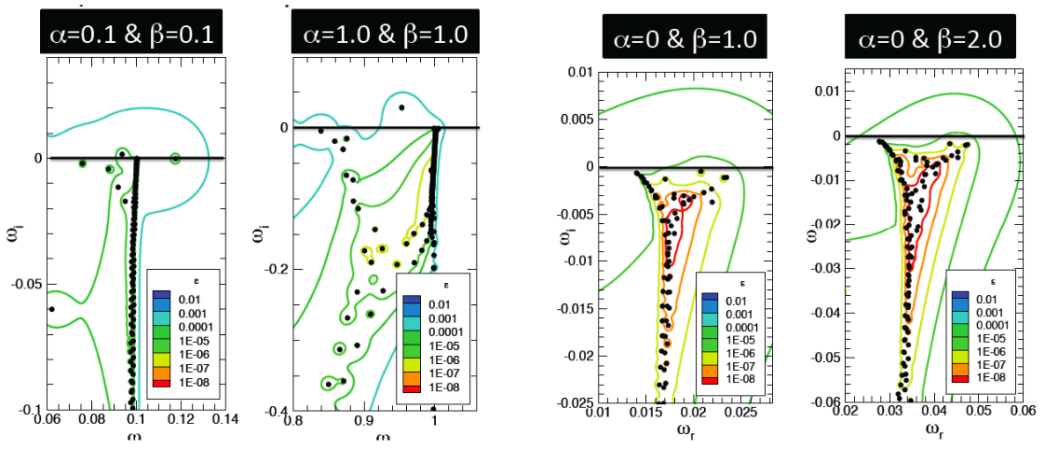

Figure 8.3: Eigenvalue spectrum and $\epsilon-$pseudospectrum corresponding to a base flow at $h = 33km$, $x = 0.4, \theta = \frac{\pi}{4}$. *Left two images:* oblique wave-like perturbations. *Right two images:* streamwise-aligned disturbances

In what follows, local transient growth analysis will be performed at two altitudes, $h = 33km$ and $h = 21km$,

Parameters	33km	21km
U_∞ [m/s]	2452.17	2207.18
ρ_∞ [kg/m^3]	0.01157	0.06581
T_∞ [K]	230.970	218.450
Re_1 [1/m]	1.89 x 10^6	1.015 x 10^7

Table 8.1: Parameters at which transient growth has been examined on the elliptic cone

at the set of parameters summarized in Table 8.1. At each of these altitudes the base flow at a large number of streamwise and azimuthal locations on the cone will be analyzed by first solving the eigenvalue and subsequently the pertinent singular value problem. Results of the latter will be used to solve the initial value problem, calculate the gain function $G(t)$ and its respective maximum, $G_{\max}$. The latter value, and the associated linear optimal conditions, will be reported as a function of the wavenumber parameters, α and β. Depending on the magnitude of the peaks of $G_{\max}$ conclusions will be drawn on the modal or non-modal nature of linear instability of the flow.

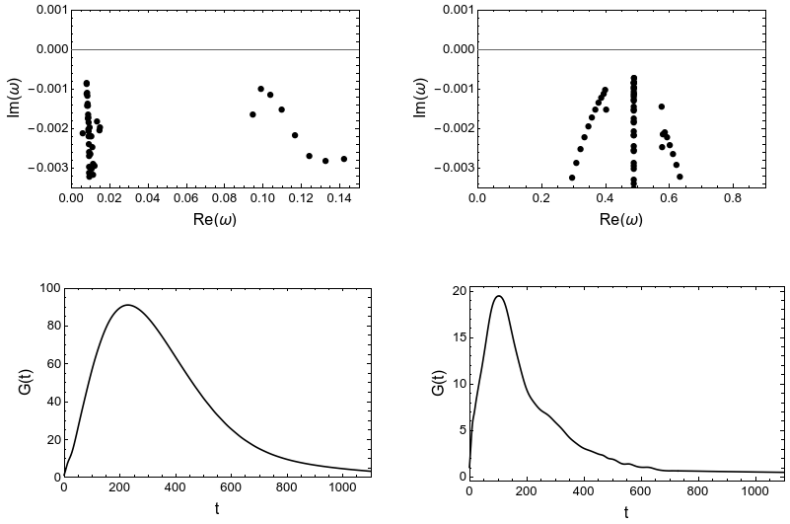

Figure 8.4: Eigenvalue Spectrum (upper row) and $G(t)$ (lower row) at $h = 33km, x = 0.62m, \theta = 60°$. Left column: streamwise aligned perturbations. Right column: two-dimensional perturbation

Figure 8.4 shows such results at $h = 33km$ altitude and $x = 0.4m$. In the upper row (stable) eigenspectra are shown at $(\alpha = 0, \beta = 0.5)$ and $(\alpha = 0.5, \beta = 0)$, while the lower row shows the evolution of the respective $G(t)$. Such results can be used to compute $G_{\max}$ as well as the (secondary in importance) time at which the maximum gain is reached. A representative result of the dependence of $G_{\max}$ on α and β at a different streamwise location on the cone surface can be found in Fig. 8.5. Starting close to the attachment line, $\theta = \frac{\pi}{4}$, it can be seen that the maximum transient energy growth is associated with a band of streamwise-aligned structures having spanwise wavenumbers that peak around $\beta = 0.6$, their streamwise wavenumber being $\alpha = 0$. The same phenomenon persists at $\theta = \frac{\pi}{3}$ and 75°, although in all three angles $G_{\max} \leq 100$ indicates that any initial perturbation will have its energy transiently amplified by maximally two orders of magnitude. It is also worth noting that at $\theta = \frac{\pi}{2}$ wave-like perturbations with $\alpha \approx 0.5$ and $\beta = 0$ are to be seen in the results, although their transient energy growth is lesser than that of the streamwise-aligned perturbations. The situation changes qualitatively at $\theta = \frac{\pi}{2}$, where $G(t)$ grows beyond bounds for two-dimensional wave-like perturbations having $\beta = 0$ and $0.0 \leq \alpha \leq 0.15$. This result clearly

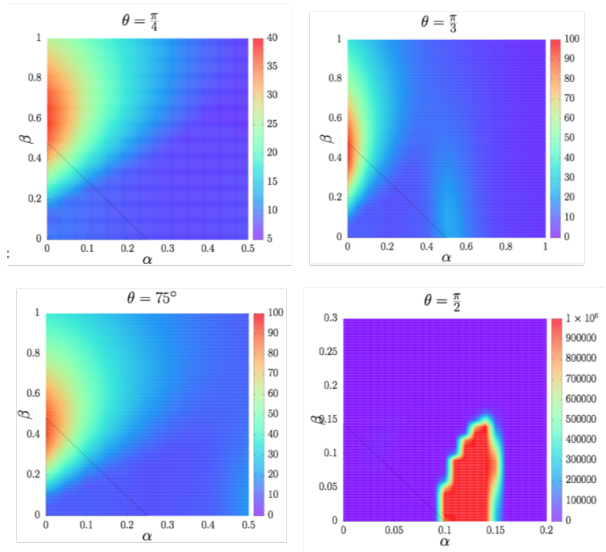

Figure 8.5: Contour plots of maximal transient energy growth $G_{\max}$ as a function of the wavenumbers α and β from local transient growth analysis of elliptic cone flow at $h = 33km$ altitude at $x = 0.4m$ on the cone surface

demonstrates that exponentially growing disturbances exist at the centerline and is consistent with the related findings of the modal analyses of Choudhari et al. (2009), Paredes and Theofilis (2015) and Paredes et al. (2016a).

8.1.1 Altitude: 33km

In order to obtain a complete picture of linear non-modal instability on the cone surface, a systematic analysis commenced at this altitude, at which the unit Reynolds number is the smallest of all available. The modal analysis of Paredes et al. (2016a) has also been performed at these conditions, such that comparison results are readily available. Taking advantage of the symmetry of the flow around an elliptic cone at zero angle of attack, only one quadrant of the cone was considered. Five axial locations along the streamwise direction have been monitored, at $x = 0.30, 0.40, 0.50, 0.6$m and $0.70m$. At each one of these locations, computations were performed for a relatively large number of azimuthal locations, discretizing the range $0 \leq \theta \leq \frac{\pi}{2}$ in 5° increments.

Figures 8.6-8.10 present contour plots of transient growth analysis at all axial locations examined. Out of the full set of azimuthal angles at which analysis was performed, in each figure results at six characteristic angles $\theta = 0^\circ$, 15°, 40°, 60°, 70° and 90° are shown. Consistently, the transient growth results deliver the largest $G_{\max}$ values at $\alpha = 90^\circ$, a location at which previous modal analyses (Choudhari et al. 2009, Paredes and Theofilis 2015, Paredes et al. 2016a) have predicted the largest amplified centerline global mode.

In the crossflow region of the results presented ($\theta = 15^\circ$-70°), different phenomena occur as x increases. At $x = 0.3m$, exponentially high values of $G_{\max}$ are obtained, peaking in the streamwise aligned direction $\beta \approx 0.3$ and $\alpha = 0$. Modal instability is prevalent practically at all azimuthal locations at this streamwise position. At $x = 0.4m$, modal instability is confined in the band $15^\circ \leq \theta \leq 40^\circ$, but disappears from the spectrum at higher angle values, $\theta = 60^\circ$ - 70°, where all eigenvalues are stable, only to reappear at the centerline. However, consistently with results shown in Fig. 8.5, streamwise-aligned structures having $\alpha = 0$ and $\beta \approx 0.6$ do exhibit transient energy growth, a result that hints at algebraic non-modal instabilities may indeed be present in hypersonic flow on the elliptic cone at this location.

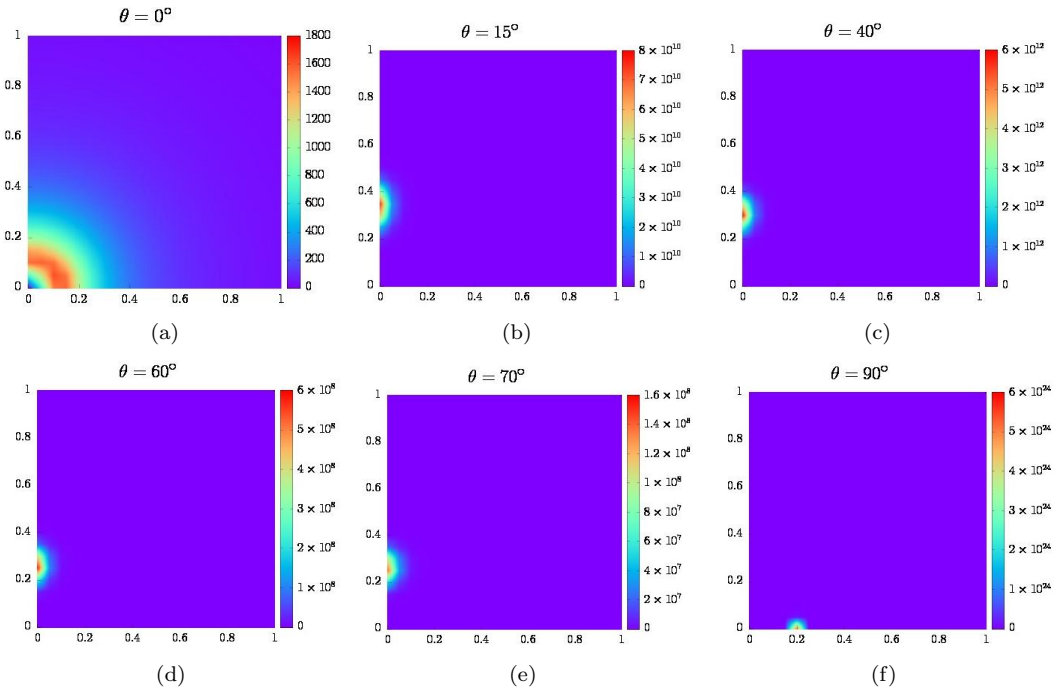

Figure 8.6: Contour plot of $G_{\max}$ at $h = 33km$ and $x = 0.3m$ as a function of the streamwise (α) and spanwise (β) wave numbers, at: (a) $\theta = 0°$; (b) $\theta = 15°$; (c) $\theta = 40°$; (d) $\theta = 60°$; (e) $\theta = 70°$; and, (f) $\theta = 90°$.

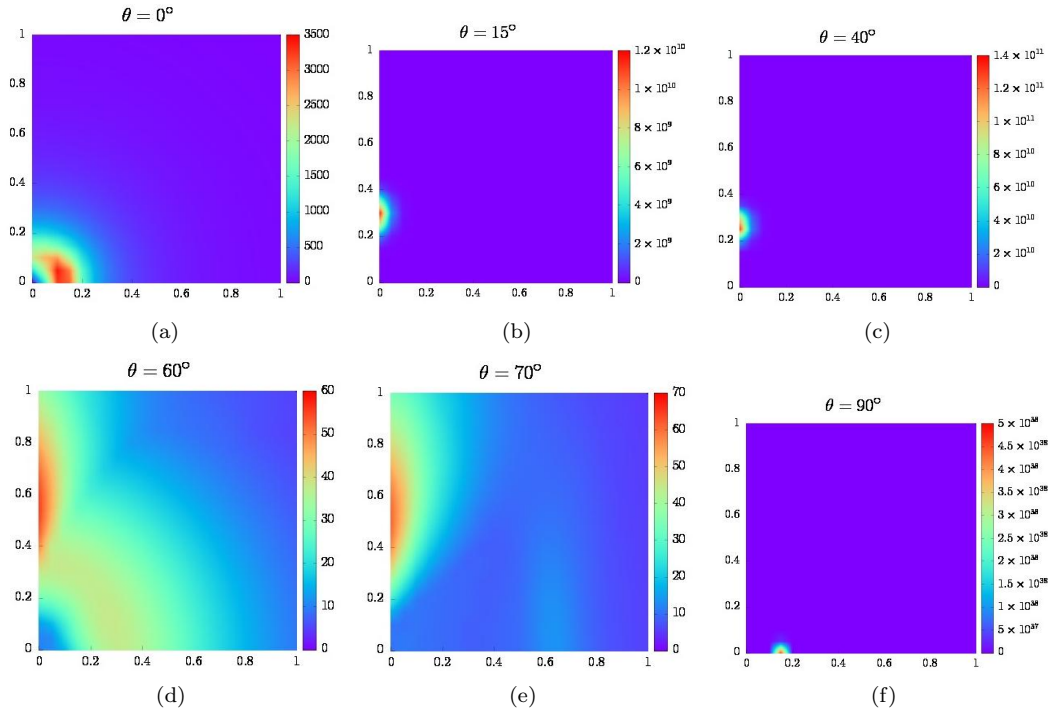

Figure 8.7: Contour plot of $G_{\max}$ at $h = 33km$ and $x = 0.4m$ as a function of the streamwise (α) and spanwise (β) wave numbers, at: (a) $\theta = 0°$; (b) $\theta = 15°$; (c) $\theta = 40°$; (d) $\theta = 60°$; (e) $\theta = 70°$; and, (f) $\theta = 90°$.

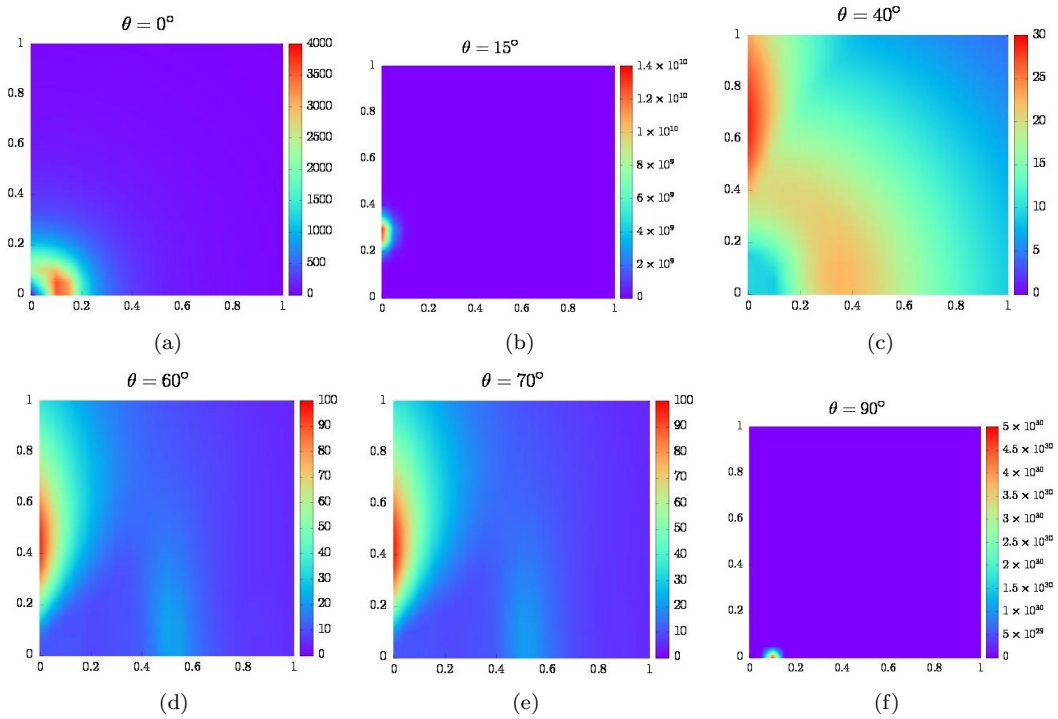

Figure 8.8: Contour plot of $G_{\max}$ at $h = 33km$ and $x = 0.5m$ as a function of the streamwise (α) and spanwise (β) wave numbers, at: (a) $\theta = 0°$; (b) $\theta = 15°$; (c) $\theta = 40°$; (d) $\theta = 60°$; (e) $\theta = 70°$; and, (f) $\theta = 90°$.

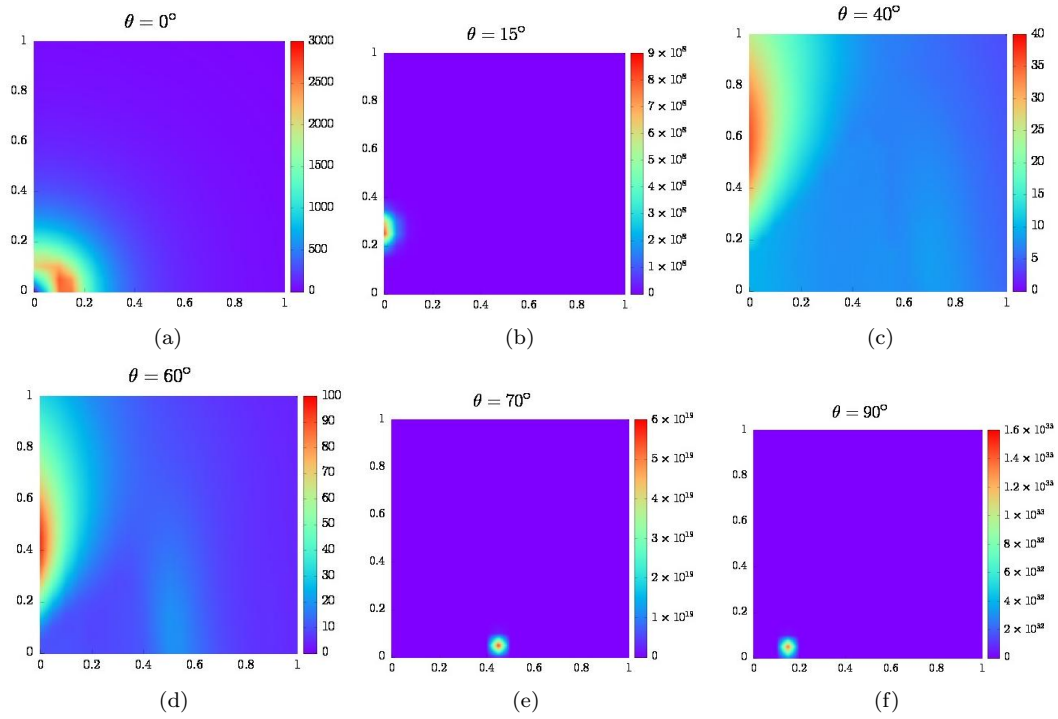

Figure 8.9: Contour plot of $G_{\max}$ at $h = 33km$ and $x = 0.6m$ as a function of the streamwise (α) and spanwise (β) wave numbers, at: (a) $\theta = 0°$; (b) $\theta = 15°$; (c) $\theta = 40°$; (d) $\theta = 60°$; (e) $\theta = 70°$; and, (f) $\theta = 90°$.

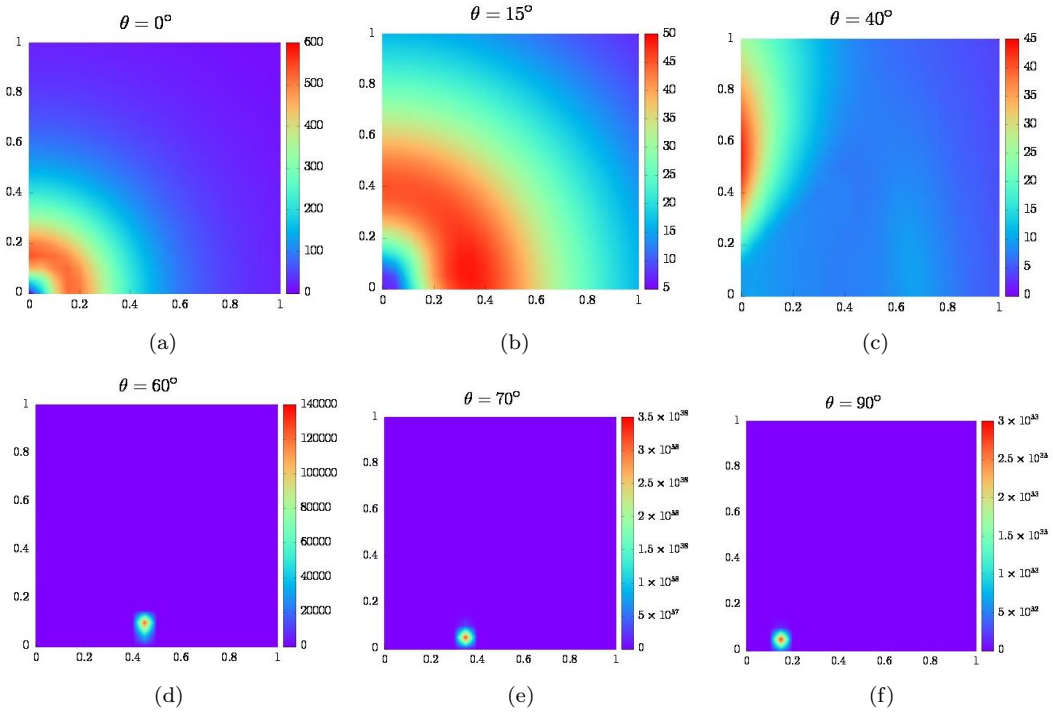

Figure 8.10: Contour plot of $G_{\max}$ at $h = 33km$ and $x = 0.7m$ as a function of the streamwise (α) and spanwise (β) wave numbers, at: (a) $\theta = 0°$; (b) $\theta = 15°$; (c) $\theta = 40°$; (d) $\theta = 60°$; (e) $\theta = 70°$; and, (f) $\theta = 90°$.

In the next position examined, $x = 0.5m$, transient growth occurs for $\theta = 40°, 60°$ and $70°$. An analogous result is found at $x = 0.6m$, however at this streamwise position at $\theta = 70°$ an amplified eigenmode dominates the spectrum. Unlike the centerline mode, though, at this location the amplified eigenmode has $\alpha \neq 0$ and $\beta \neq 0$, and can be cataloged as an exponentially amplified oblique mode.

In the last position where the analysis was performed ($x = 0.7m$) transient growth can still be found for small angles ($\theta = 15°$ and $40°$) but with two different characteristics. At $\theta = 15°$ the peak is at $\beta = 0$ and $\alpha \neq 0$ direction, but it is important to notice the existence of a smaller, but in the same order of magnitude, peak at $\alpha = 0$. At $\theta = 40°$ there is only one peak at the streamwise-oriented direction. At this $x-$location, an amplified eigenmode dominates at large angles ($\theta = 60°$, $\theta = 70°$) with the same characteristics of the one presented in the previous position, i.e. oblique mode.

At the attachment-line $\theta = 0°$ the highest amplification rate for all cases is observed in the direction of $\alpha = 0.1-0.2$. However, the values of $G_{\max}$ are one order of magnitude higher than the previous transient growth cases but still substantially smaller than the modal scenario. For this reason, it is unclear whether modal or non-modal instability prevails. In fact, the values of gain obtained could be related to strong transient growth or a low amplification rate modal instability that requires a long time-integration to reach substantial amplitude levels.

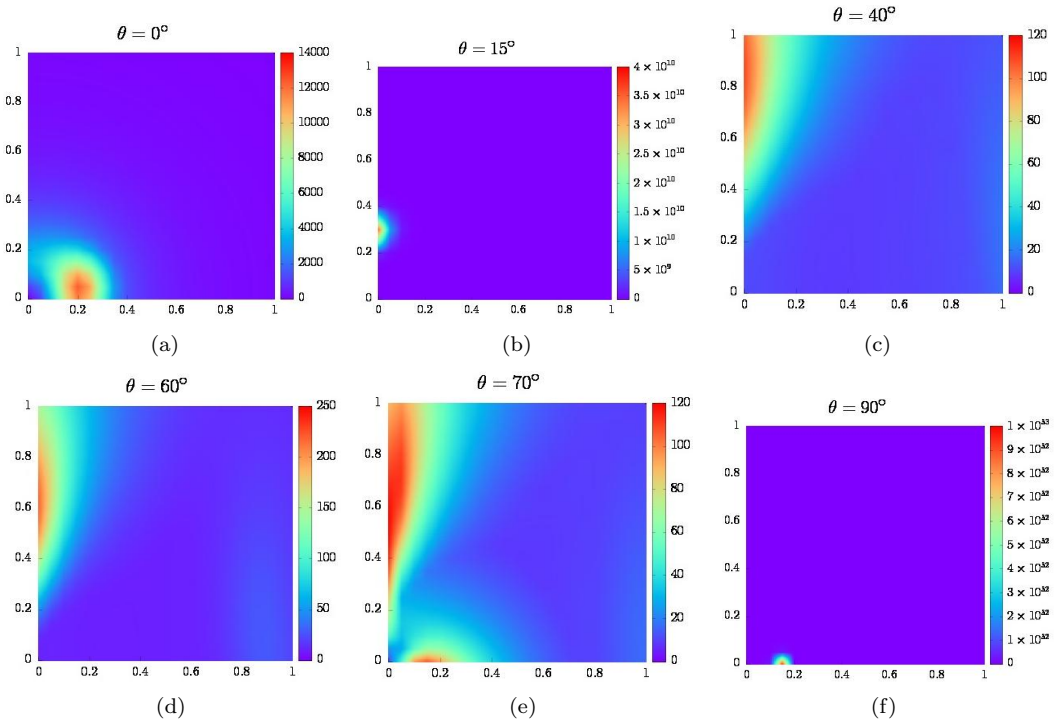

Figure 8.11: Contour plot of $G_{\max}$ at $h = 21km$ and $x = 0.3m$ as a function of the streamwise (α) and spanwise (β) wave numbers, at: (a) $\theta = 0°$; (b) $\theta = 15°$; (c) $\theta = 40°$; (d) $\theta = 60°$; (e) $\theta = 70°$; and, (f) $\theta = 90°$.

8.1.2 Altitude: 21km

For the sake of comparison with results at the higher altitude, Figures 8.11-8.15 present contour plots of transient growth analysis at $h = 21km$, at the same axial and azimuthal locations as results shown in the previous section. At this lower altitude, at which the modal global analysis of Paredes et al. (2016a) was performed, the Reynolds number is an order of magnitude higher, and the first qualitative difference compared with the $h = 33km$ case is that at the attachment line, at all axial locations examined, the dominant physical instability mechanism is non-modal, corresponding to streamwise-oriented structures. Transient energy amplification at the attachment line is found to be strongest close to the cone tip. At the centerline, modal instability mode is still the dominant instability mechanism, but once again, at $x \geq 0.4m$ the dominant modes are oblique, having both $\alpha \neq 0$ and $\beta \neq 0$. Moreover, at $x = 0.4m$, it is possible to notice that two modes may exist with both having high $G_{\max}$, a scenario already pointed out in the modal analysis of Paredes et al. (2016a).

In the crossflow region, at $x = 0.3m$, the results are analogous to those presented at positions $x = 0.4m$ and $x = 0.5m$ for the 33km altitude. An eigenmode peaks in the streamwise-oriented direction for small angles and non-modal instabilities are present at other angles. It is important to notice that at $\theta = 70°$, there are two simultaneous peaks, one corresponding to streamwise-oriented and the other to spanwise-oriented structures. At $x \geq 0.4m$ analogous phenomena as those encountered at the higher altitude are found. For small angles transient growth plays a role whereas for medium and large angles modal instability is the dominant linear scenario. One differentiating characteristic of these modes compared to the centerline mode is their at least twice as large α values. It is also found that at $x = 0.7m, \theta = 60°$ two peaks have been identified, having comparable values of magnitude of $G_{\max}$, but differing in their respective α and β values. One is a spanwise-oriented perturbation while the other is an oblique wave.

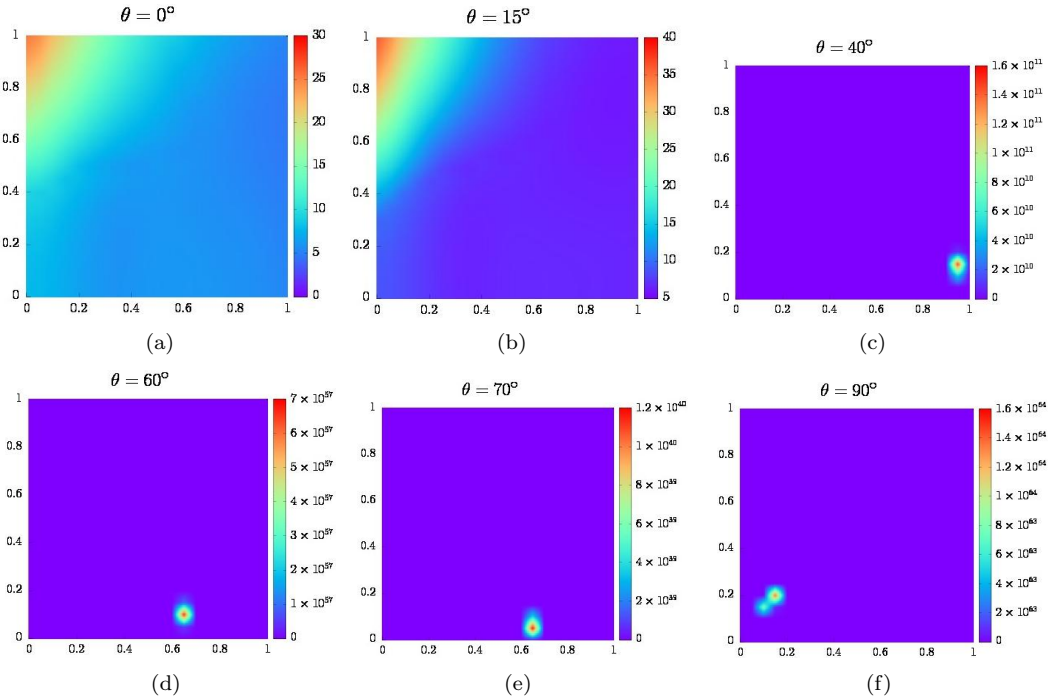

Figure 8.12: Contour plot of $G_{\max}$ at $h = 21km$ and $x = 0.4m$ as a function of the streamwise (α) and spanwise (β) wave numbers, at: (a) $\theta = 0°$; (b) $\theta = 15°$; (c) $\theta = 40°$; (d) $\theta = 60°$; (e) $\theta = 70°$; and, (f) $\theta = 90°$.

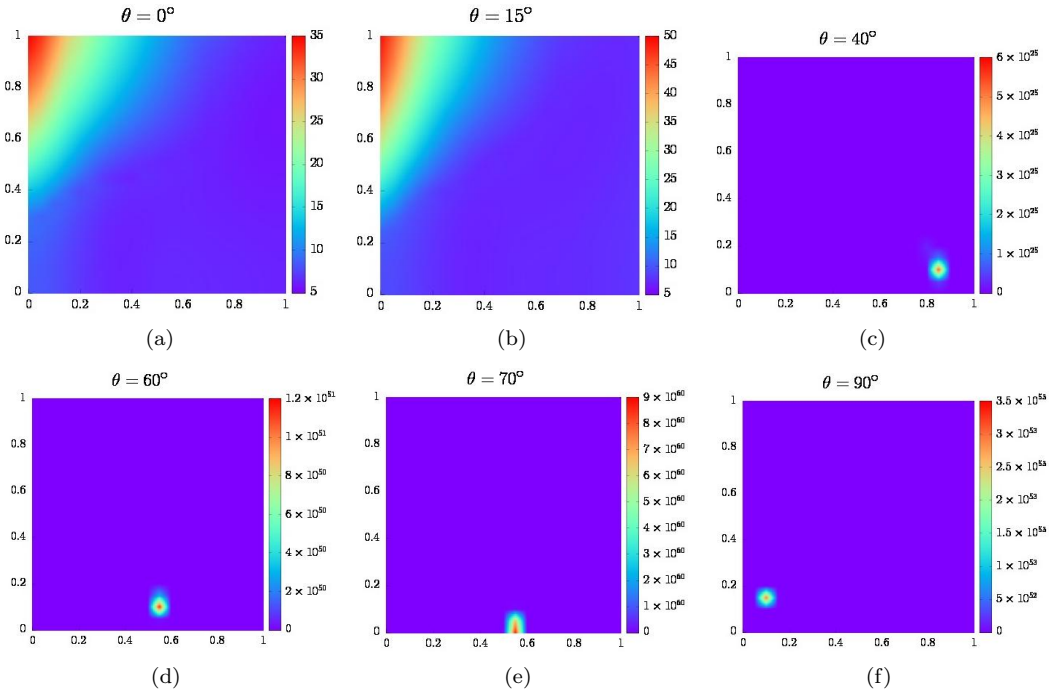

Figure 8.13: Contour plot of $G_{\max}$ at $h = 21km$ and $x = 0.5m$ as a function of the streamwise (α) and spanwise (β) wave numbers, at: (a) $\theta = 0°$; (b) $\theta = 15°$; (c) $\theta = 40°$; (d) $\theta = 60°$; (e) $\theta = 70°$; and, (f) $\theta = 90°$.

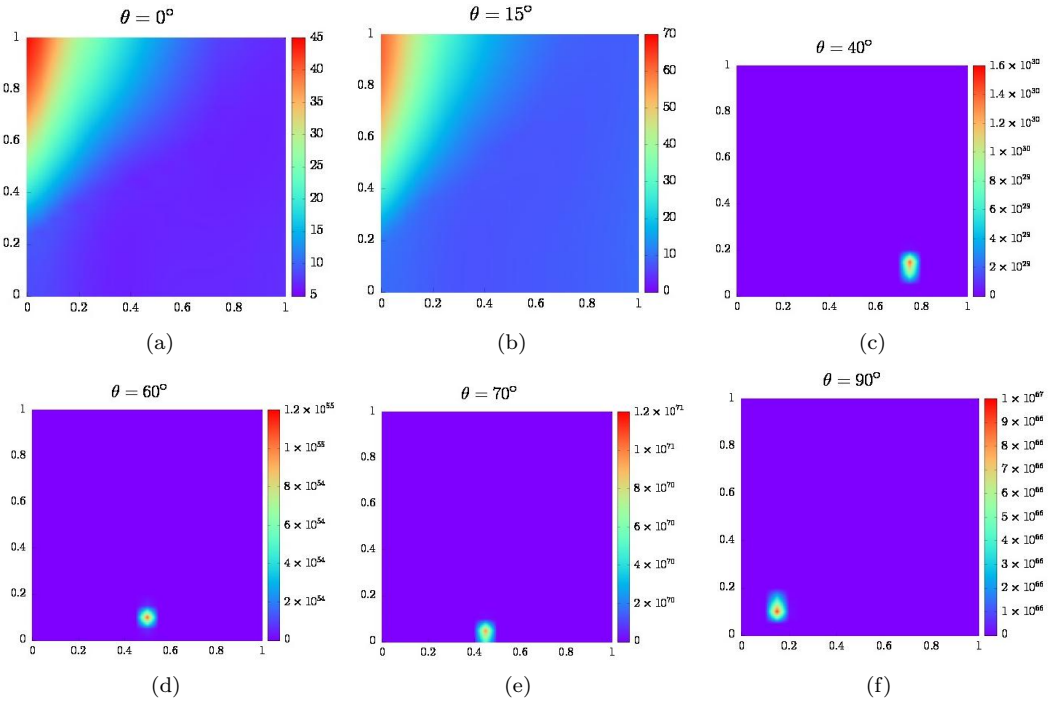

Figure 8.14: Contour plot of $G_{\max}$ at $h = 21km$ and $x = 0.6m$ as a function of the streamwise (α) and spanwise (β) wave numbers, at: (a) $\theta = 0°$; (b) $\theta = 15°$; (c) $\theta = 40°$; (d) $\theta = 60°$; (e) $\theta = 70°$; and, (f) $\theta = 90°$.

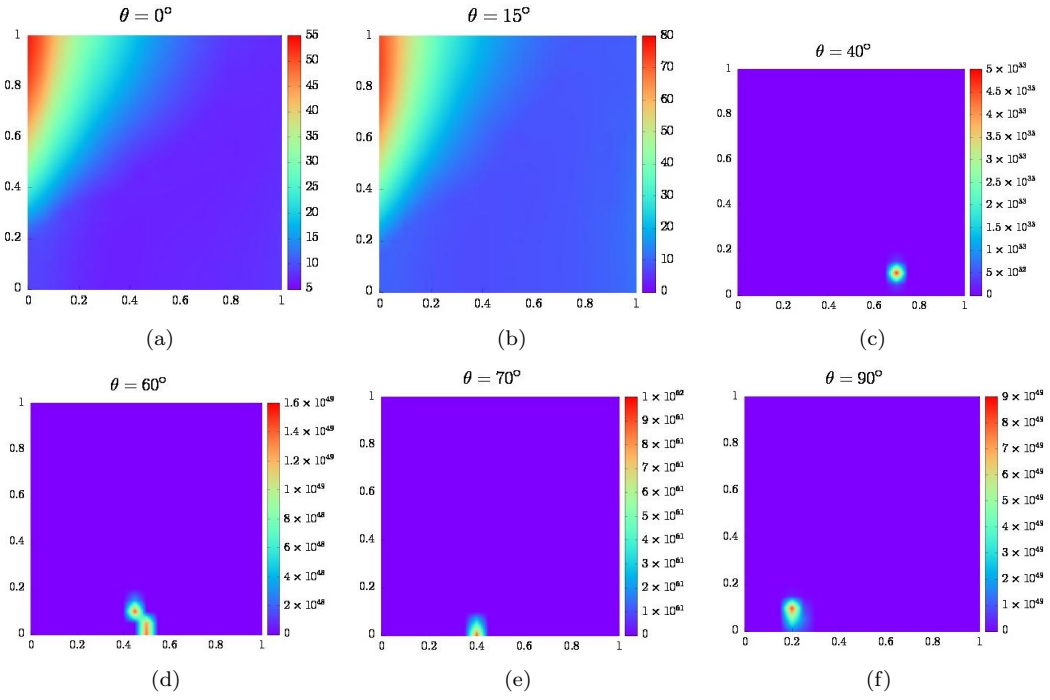

Figure 8.15: Contour plot of $G_{\max}$ at $h = 21km$ and $x = 0.7m$ as a function of the streamwise (α) and spanwise (β) wave numbers, at: (a) $\theta = 0°$; (b) $\theta = 15°$; (c) $\theta = 40°$; (d) $\theta = 60°$; (e) $\theta = 70°$; and, (f) $\theta = 90°$.

8.1.3 Comparisons with the ground-based experiments of Borg et al. (2012)

The theoretical results obtained point to the existence of elongated structures along the elliptic cone, the origin of which is modal or non-modal instability, depending on the location on the elliptic cone surface. In the absence of direct in-flight measurements on the HIFiRE-5 elliptic cone, information on these elongated structures is sought in the BAM6QT experiments of Borg et al. (2012). These experiments used a 38.1% scale model of the HIFiRE-5 elliptic cone at a comparable Reynolds number as those used in the present analysis. As a matter of fact, the experimental Reynolds number, $Re = 8.1 \times 10^6$, lies in-between those corresponding to the two altitudes analyzed.

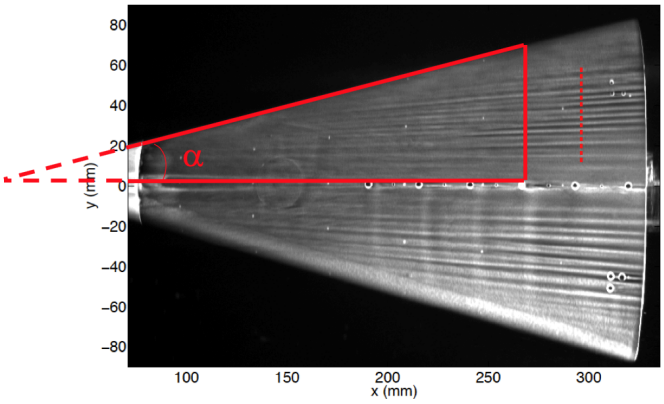

(a)

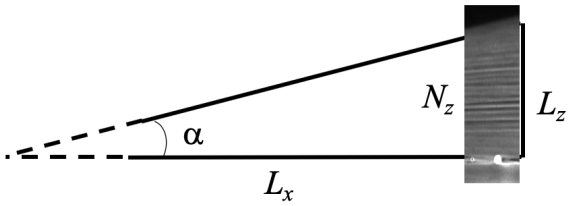

(b)

Figure 8.16: Streamwise-aligned structures in the experiment of Borg et al. (2012) (a) Oil flow visualization at a $Re = 8.1 \times 10^6$; (b) Estimation of spacing between structures

Oil flow visualization experimental results are shown in Fig. 8.16(a). In Fig. 8.16(b) the geometrical procedure used to estimate length scales and the spacing between the observed vortices is also shown. The known length $L_x \approx 250mm$ and known angle $\alpha \approx 14°$, alongside the trigonometric relationship $L_z = L_x \tan\alpha$ deliver an estimate for the spanwise length marked on Fig. 8.16(b), $L_z \approx 60mm$. The spacing between the streamwise structures was estimated using an estimate of $N_z \approx 10-15$ such structures being visible within L_z; the dotted line marked on this figure shows that the average spacing between the distinct structures is $\Delta_z \approx 2-7mm$. In order for comparisons to be made with the experimental results, the dimensional reference length used in the present analysis,

$$\frac{1}{L_{ref}} = \sqrt{\frac{x}{Re'}} \tag{8.1}$$

has been used to calculate dimensional values for the theoretical results for the wavenumbers α and β, from which the (dimensional) theoretical spanwise spacing, $\Delta_z = \frac{2\pi}{\beta}$, has been calculated. Full results from the analysis presented at $h = 33km$ and $h = 21km$ can be found in Table 8.2, while a typical result is shown in graphical form in Fig. 8.17.

	$h = 33km$					$h = 21km$				
$x \setminus \theta$	0°	15°	40°	60°	70°	0°	15°	40°	60°	70°
0.3	–	–	–	–	–	–	–	1.20	1.80	1.54
0.4	–	–	–	4.81	5.25	1.24	1.24	–	–	–
0.5	–	–	4.61	7.18	7.18	1.39	1.39	–	–	–
0.6	–	–	5.90	7.86	–	1.52	1.52	–	–	–
0.7	–	8.85	6.37	–	–	1.65	1.65	–	–	–

Table 8.2: Values of spacing between structures Δ_z in mm at $h = 33km$ and 21km

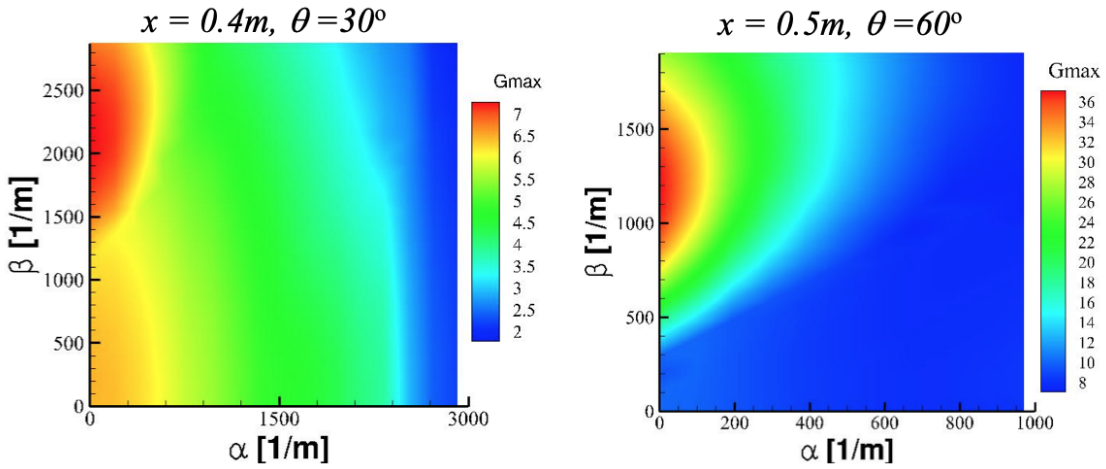

Figure 8.17: Typical dimensional wavenumber values resulting from transient growth analyses at two locations on the cone surface

In Table 8.2 it is seen that, at a given location, the spacing Δ_z between spanwise structures and, consequently, the size of the structures themselves, is seen to assume systematically larger values at $h = 33km$ and smaller corresponding values at $h = 21km$. This result is consistent with the Reynolds number increasing at the lower altitude. Significantly, the range of spacings calculated in the analyses of sections 8.1.1 and 8.1.2 and the estimates of the corresponding experimental results coincide. Notwithstanding the limitations of having performed a local transient growth analysis, *this result is the first theoretical demonstration that the transient growth phenomenon is relevant to hypersonic flow at flight conditions.*

8.2 Global transient growth analysis

Non-modal global stability analysis is carried out at the same two altitudes and parameters shown in Table 8.1, to facilitate comparisons with local transient growth results obtained in the previous section. Note that, for consistency, the homogeneous spatial direction in the BiGlobal Ansatz is x, while the spanwise direction, z, is now fully resolved. A temporal BiGlobal analysis framework is considered, in which $\alpha = 2\pi/L_x$ is a real streamwise/axial wavenumber parameter; Fig. 8.18 schematically presents the analysis concept.

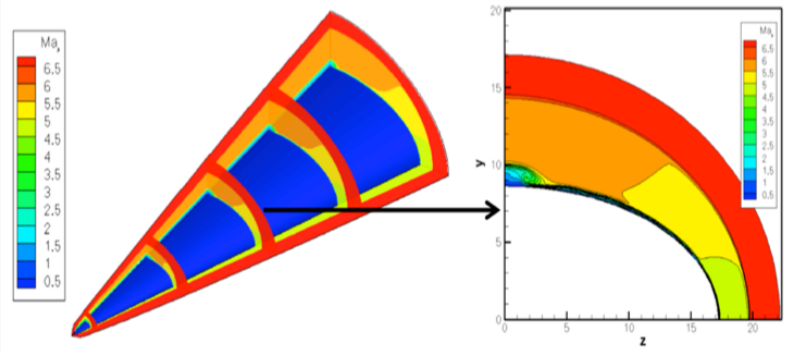

Figure 8.18: Two–dimensional profiles extracted from the base flow at a given streamwise position on the elliptic cone

The present theoretical foundation is the same as that used in the previous section and has been discussed in Section 4. The key difference with the local transient growth analysis is that in this chapter the assumption of wave-like perturbations along the spanwise direction, z, is not invoked. As such the analysis discussed in section 4.6 now refers to numerical solutions of the two-dimensional eigenvalue problem; similarly, the subsequent SVD computation discussed in section 4.7 now rests on global modes. The latter are used, alongside their adjoints, to solve the initial value problem (4.3) by projecting an initial condition onto a reduced set of eigenvectors according to (4.18-4.19). In global transient growth analysis too, time is a parameter and since no assumption of harmonic-in-time perturbations has been made, solutions of the initial value problem obtained herein encompass both classes of perturbations, those growing algebraically at early times (non-modal linear perturbations) as well as exponentially growing instabilities at large times (eigenmodes). In other words, though substantially more expensive than modal analysis, such as that performed by Choudhari et al. (2009), Paredes and Theofilis (2015) and Paredes et al. (2016a), solutions of the initial value problem obtained in this section deliver the most complete picture of linear flow instability of hypersonic flow on the elliptic cone.

Although it is relatively straightforward to assess whether transient energy growth occurs at any set of parameters, what makes global transient growth analysis expensive is the length of the time-horizon that needs to be monitored, i.e. for which the IVP needs to be solved, is unknown at the beginning of the analysis. The reason is that modal instabilities may have low amplification rates and solution of (4.3) needs to proceed for sufficiently long times until modal instabilities potentially existing in the system manifest themselves. Precisely this property is also a quality criterion for the nonmodal analysis performed: the degree of agreement between the amplification/damping rate of the leading eigenmode (obtained by solution of the EVP) and the logarithmic derivative of the time-signal of $G(t)$ at large times (obtained in the SVD context) is an objective measure of the quality of the numerical work. The results obtained in this section have been subjected to this test and representative modal and non-modal predictions of the amplification rate of the linear perturbation at long time horizons are shown in Table 8.3. These results were obtained on grids employing up to $(N_\eta, N_\zeta) = (110, 70)$ Chebyshev Gauss Lobatto points.

Altitude	Centerline BC	Wavenumber α	EVP solution	SVD solution
$33km$	Symmetry	0	0.0026771	0.0026696
$21km$	Symmetry	0	0.0225863	0.0228318

Table 8.3: Comparisons of modal and non-modal amplification rate predictions in the present global transient growth analysis

8.2.1 Altitude: 33km

Attention is focused on the vicinity of the centerline and the initial value problem is solved at an axial distance $x = 0.6m$ from the cone tip, for two streamwise wave numbers $\alpha = 0$ and 0.25. Symmetric and anti-symmetric modes are analyzed separately. At $\alpha = 0$, Fig. 8.19 shows the gain at two different time horizons, a short, $t = 60$, and a long one, $t = 1000$. As can be seen in the left part of Fig. 8.19(a), at short times transient growth of the disturbances is present, in accordance to the temporal local stability results of the previous section at the same location on the cone. Local transient growth theory predicted a $G_{\max} = O(10^3 - 10^4)$, which is also found in the present global transient growth analysis, without resorting to the spanwise homogeneity assumption. As local transient growth analysis predicted, modal instability is expected to appear at the centerline at asymptotically long times. The present BiGlobal non-modal result shows that indeed after sufficiently long integration time has elapsed, $G(t)$ grows exponentially, as shown in the right part of Fig. 8.19(a) in a semi-logarithmic scale.

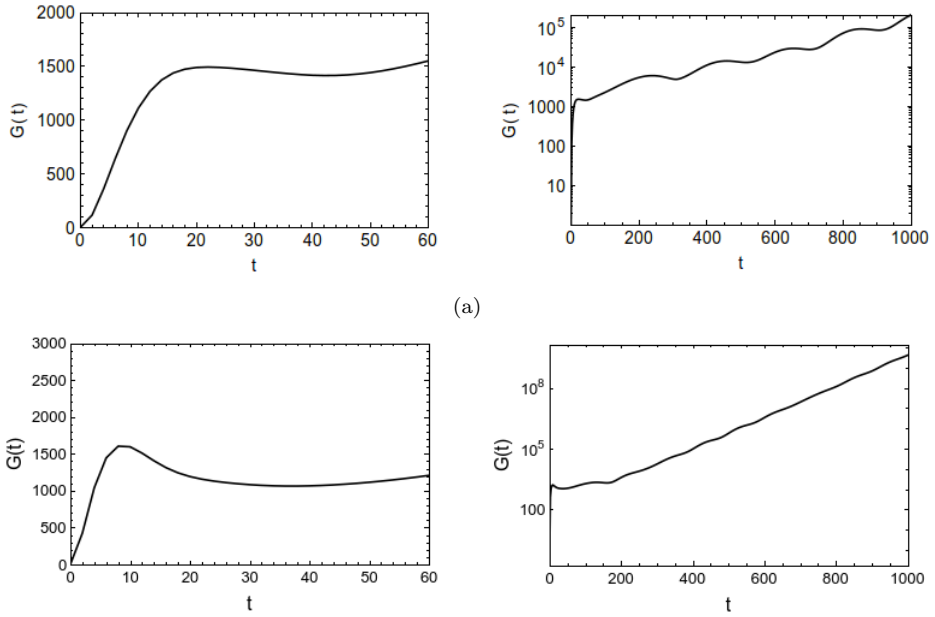

(a)

(b)

Figure 8.19: (a) $\alpha = 0$; (b) $\alpha = 0.25$

In order to obtain quantitative verification of this prediction, the logarithmic derivative (the slope) of the $G(t)$ signal is calculated at asymptotically large times and the result is compared with the amplification rate of a modal perturbation, ω_i, through the expression

$$\lim_{t\to\infty} G(t) \approx \exp(2\omega_i t). \tag{8.2}$$

The result is that shown in the first line of Table 8.3, where excellent agreement between the two quantities can be seen. This finding cross-validates the global transient growth implementation and verifies the previous investigations from a physical point of view, namely that the modal scenario dominates at the selected set of parameters. Finally, $G(t)$ in time horizons of $t = 60$ and $t = 1000$ is shown at $\alpha = 0.25$ in Fig. 8.19(b). Qualitatively the same behavior as for $\alpha = 0$ is observed. Transient growth at short-time horizon is followed by a modally unstable behavior at asymptotically long times; the slope of the semi-logarithmic $G(t)$ curve is again found to equal to twice the growth rate of the underlying most unstable mode.

Figures 8.20 and 8.21, respectively present the amplitude functions of the most unstable linear perturbations corresponding to $\alpha = 0.25$, superimposed upon iso-lines of the streamwise base flow velocity. The computed eigenvalues are $\omega = (0.03056 + \mathrm{i}\ 0.004956)$ for the first symmetric and $\omega = (0.01723 + \mathrm{i}\ 0.003272)$ for the second in significance symmetric perturbation. In both cases, the modes peak inside the boundary layer, and because of the lift-up of low momentum fluid at the centerline, the modes also peak at the location of the maximum lateral shear. In both cases, the peaks are away from the centerline.

Figures 8.23 and 8.24 present the real and imaginary part of the amplitude functions of the second in significance symmetric and anti-symmetric modes. The respective eigenvalues are $\omega = (0.01121 + \mathrm{i}\ 0.002975)$ for the symmetric case and $\omega = (0.0 + \mathrm{i}\ 0.002886)$ for the anti-symmetric mode, the latter being the only stationary disturbance of significance at these conditions. Unlike their most unstable counterparts, these modes peak only at the location of the base flow shear away from the wall, and not in the boundary layer.

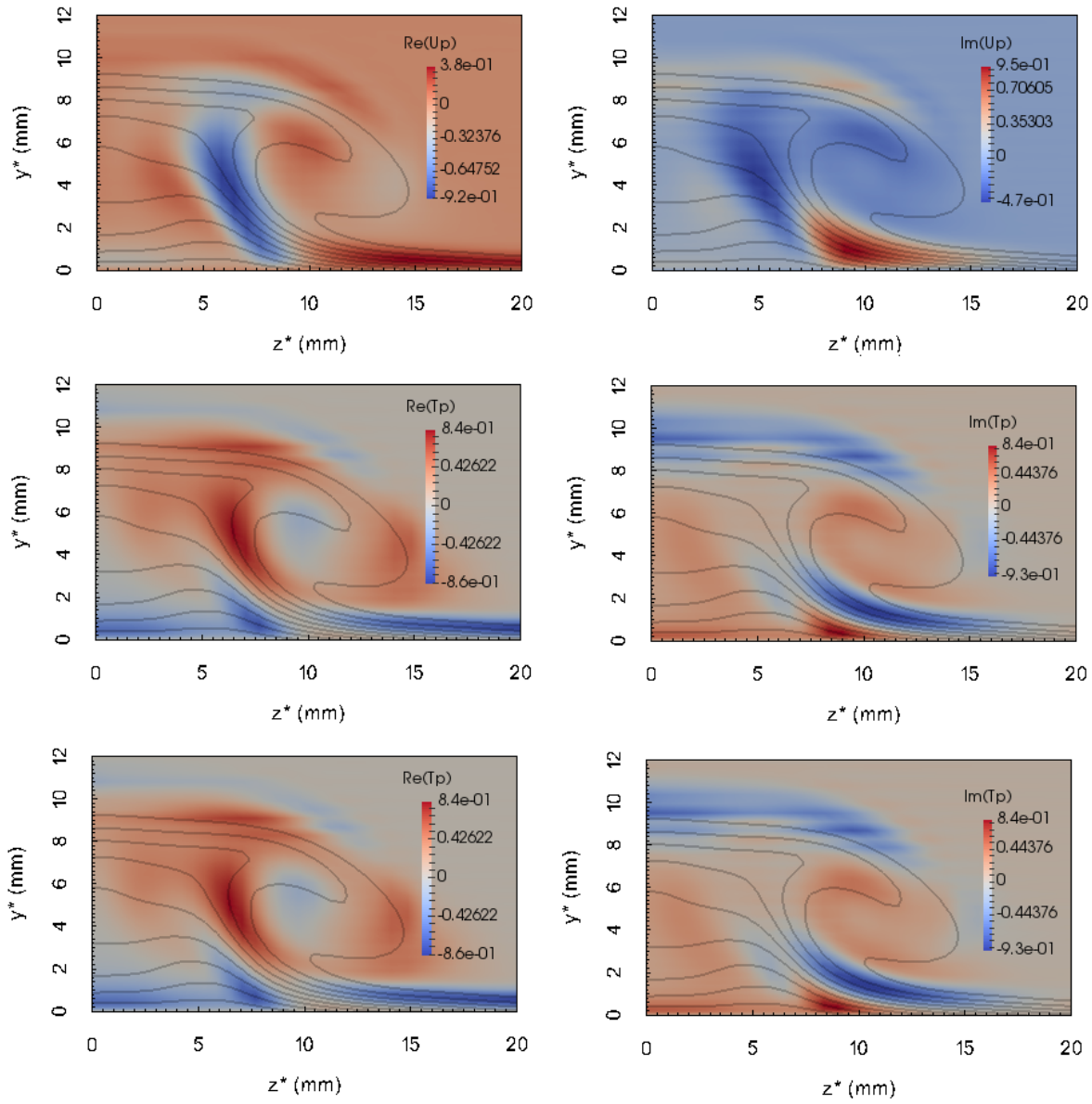

Figure 8.20: Real (left column) and Imaginary (right column) part of the streamwise (top row), spanwise (middle row) and temperature (lower row) amplitude functions of the most unstable symmetric mode at $h = 33km, \alpha = 0$ in the vicinity of the centerline, having $\omega = (0.03056 + \mathrm{i}\ 0.004956)$. The iso-lines correspond to the streamwise velocity component of the base flow

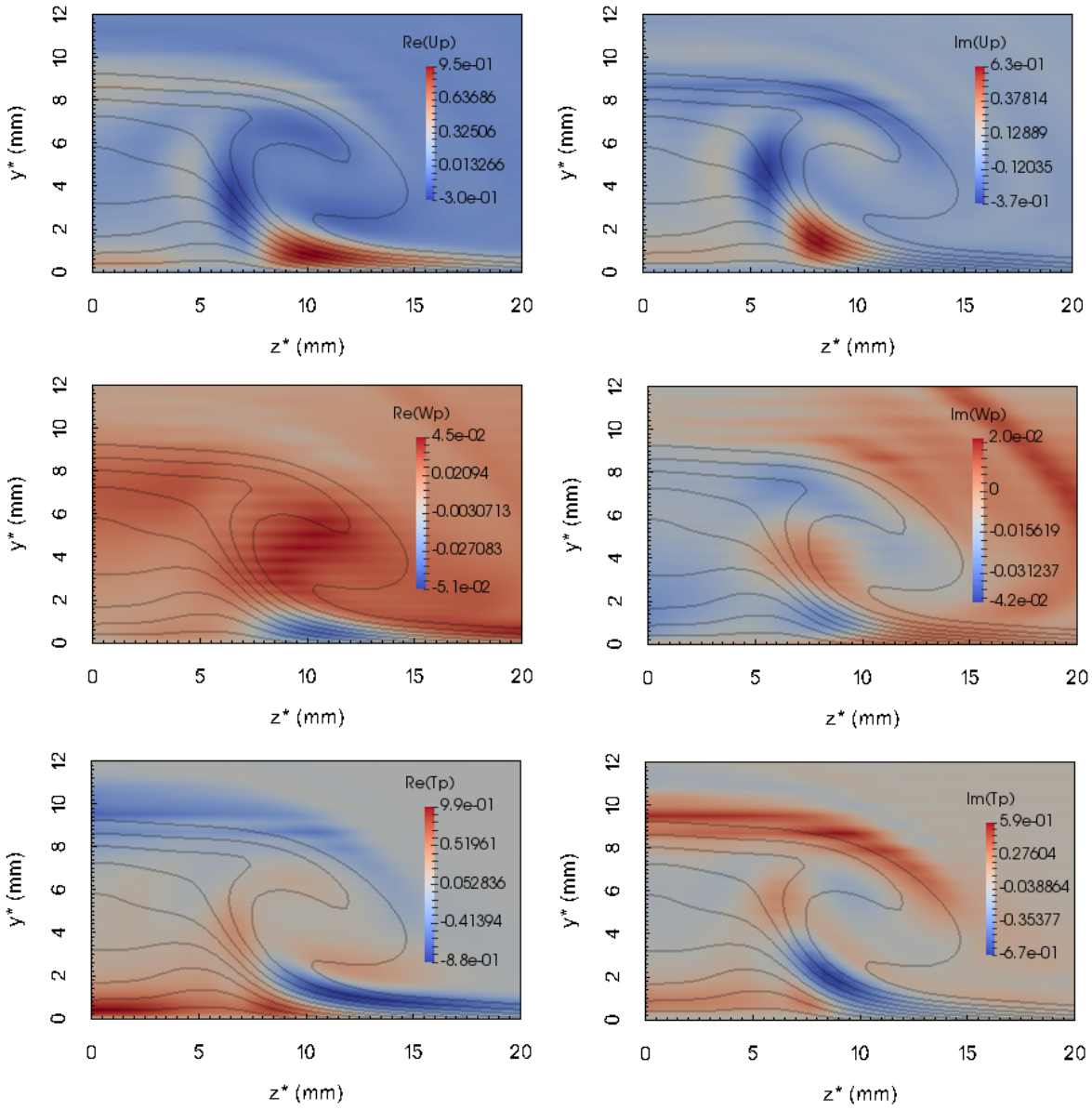

Figure 8.21: Real (left column) and Imaginary (right column) part of the streamwise (top row), spanwise (middle row) and temperature (lower row) amplitude functions of the most unstable anti-symmetric mode at $h = 33km, \alpha = 0$ in the vicinity of the centerline, having $\omega = (0.01723 + \mathrm{i}\ 0.003272)$

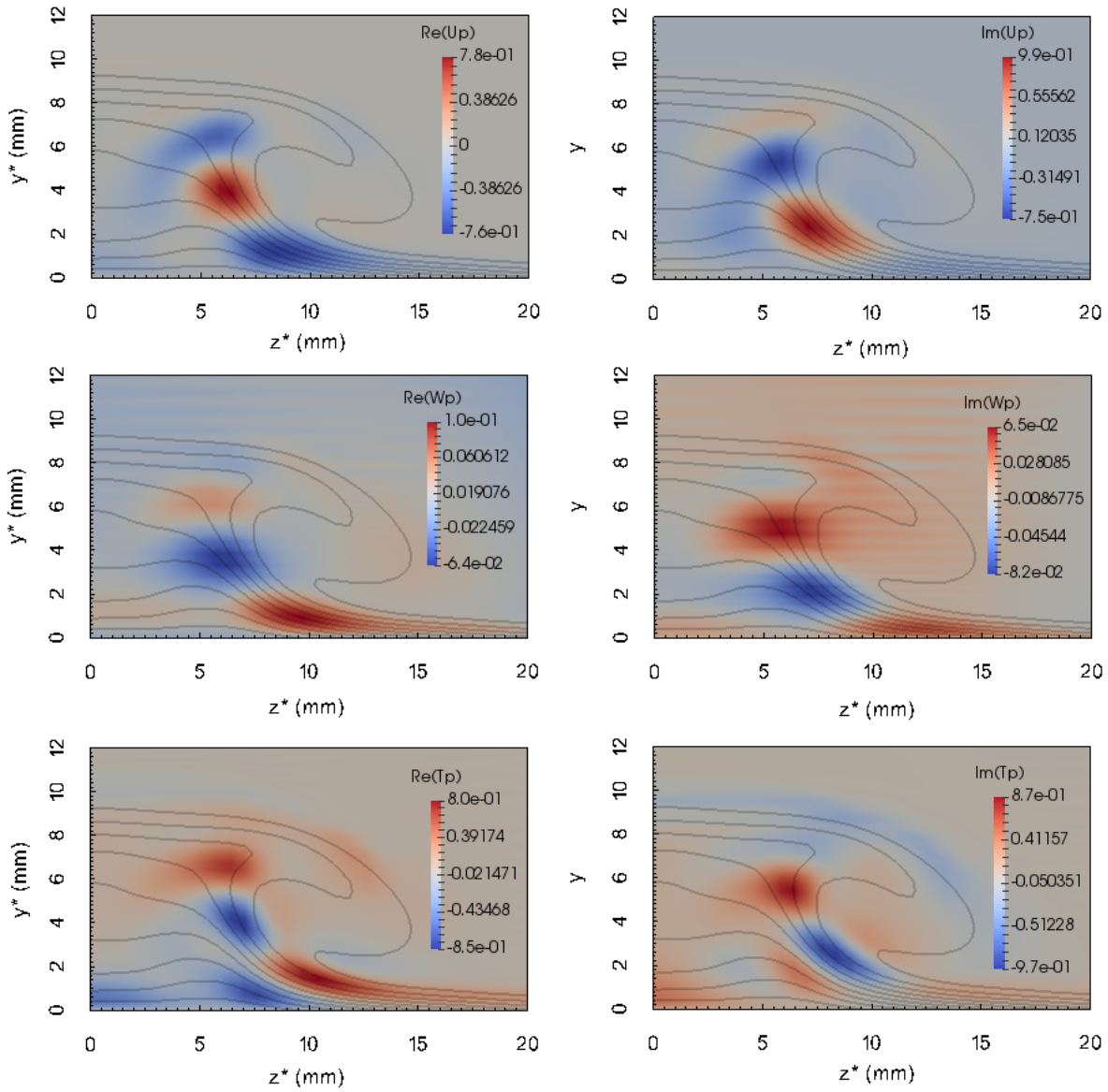

Figure 8.22: Real (left) and Imaginary (right) part of the streamwise, spanwise and temperature disturbance for the second most unstable symmetric mode ω (0.01121 + i 0.002975). The iso-lines correspond to the streamwise velocity component of the base flow.

Figure 8.23: Real (left column) and Imaginary (right column) part of the streamwise (top row), spanwise (middle row) and temperature (lower row) amplitude functions of the second in importance symmetric mode at $h = 33km, \alpha = 0$ in the vicinity of the centerline, having $\omega = (0.01121 + \text{i } 0.002975)$

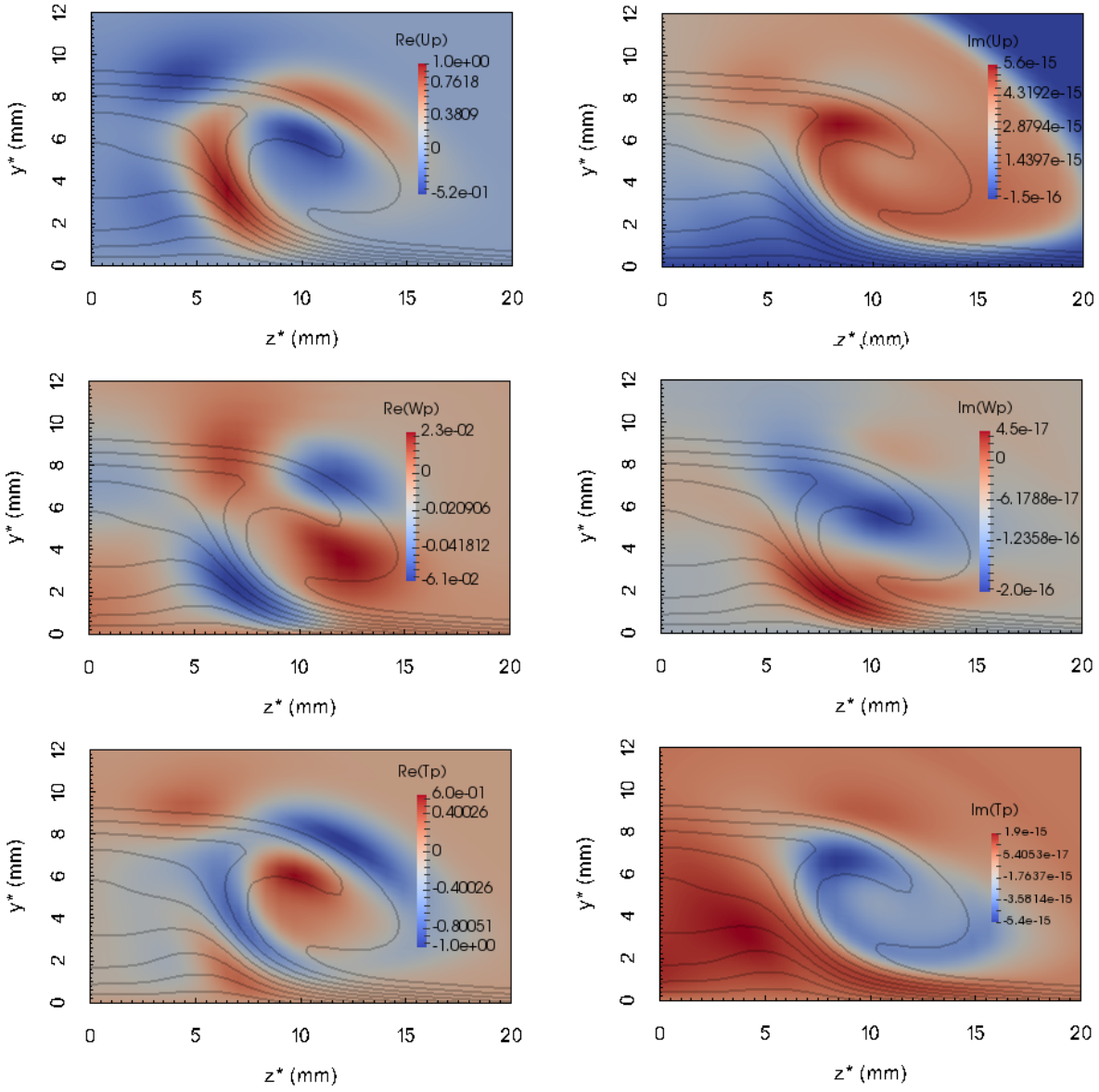

Figure 8.24: Real (left column) and Imaginary (right column) part of the streamwise (top row), spanwise (middle row) and temperature (lower row) amplitude functions of the second in importance anti-symmetric mode at $h = 33km, \alpha = 0$ in the vicinity of the centerline, having $\omega = (0 + \mathrm{i}\ 0.002886)$

8.2.2 Altitude: 21km

At $h = 21km$ global transient growth analyses are performed at the same axial position $x = 0.6m$ from the cone tip and streamwise wave-number $\alpha = 0$, in order for direct comparisons to be made with the $h = 33km$ results. Again, symmetric and anti-symmetric boundary conditions are imposed at the minor semi-axis, while resolutions analogous to those used in the analyses at the higher altitude are used. Figure 8.25 illustrates representative results for the symmetric (in (a)) and antisymmetric (in (b)) boundary conditions. Most significantly, at this altitude a qualitative difference has been found to exist, compared with results obtained at the $h = 33km$ altitude, namely that *no transient growth is found at* $h = 21km$. Results obtained at all parameters examined correspond to exponentially amplified eigenmodes, which manifest themselves already at $t = 0^+$, as can clearly be seen in the representative results of Fig.8.25.

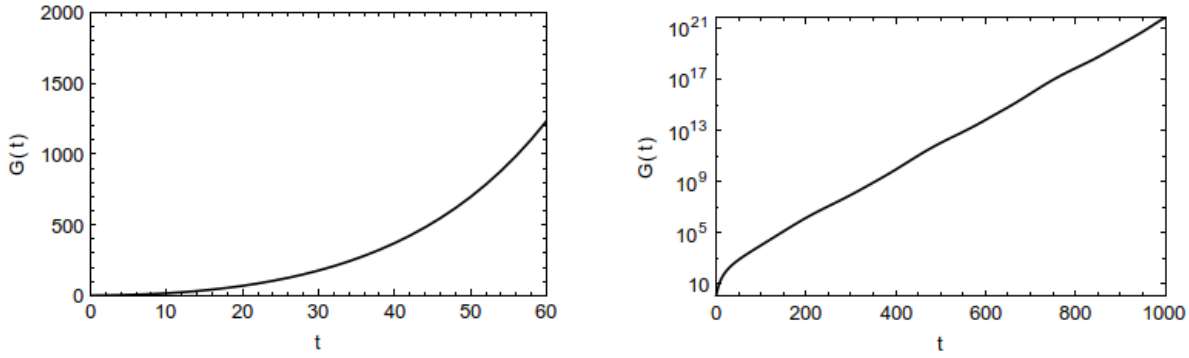

(a)

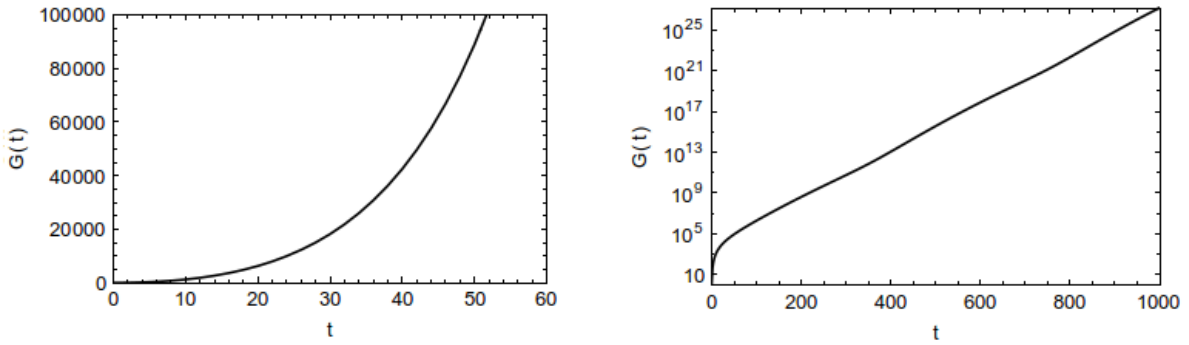

(b)

Figure 8.25: (a) Symmetric mode; (b) Anti-symmetric mode

Figures 8.26 and 8.27 present the real and imaginary parts of the amplitude functions, superimposed upon iso-lines of the streamwise base flow velocity, corresponding to symmetric and anti-symmetric modes, respectively. The respective eigenvalues both correspond to stationary disturbances, having $\omega = (0.0 + \mathrm{i}\ 0.003946)$ for the symmetric mode and $\omega = (0.0 + \mathrm{i}\ 0.003634)$ for the anti-symmetric mode. In both cases of symmetric and antisymmetric modes at the parameters shown, and others obtained but not presented here, the amplitude functions appear to inherit the mushroom-shaped structure of the underlying base flow, indicating that the centerline mode, identified in the analyses of Choudhari et al. (2009), Paredes and Theofilis (2015) and Paredes et al. (2016a) is the dominant instability.

Besides this qualitative difference with the global transient growth analysis results obtained in this section at the higher altitude of $h = 33km$, it is also instructive to note that the global nonmodal analysis confirmed the

trend identified by local transient growth theory, namely that *the significance of non-modal growth increases with increasing altitude*. Conversely, as the unit Reynolds number increases, modal instability appears to be to only relevant scenario leading laminar flow on the elliptic cone to transition. These conclusions are significant since, to the best of our knowledge, they are obtained for the first time in the configuration at hand, without relying on expensive direct numerical simulations and also free from the restrictive approximations of local transient growth theory.

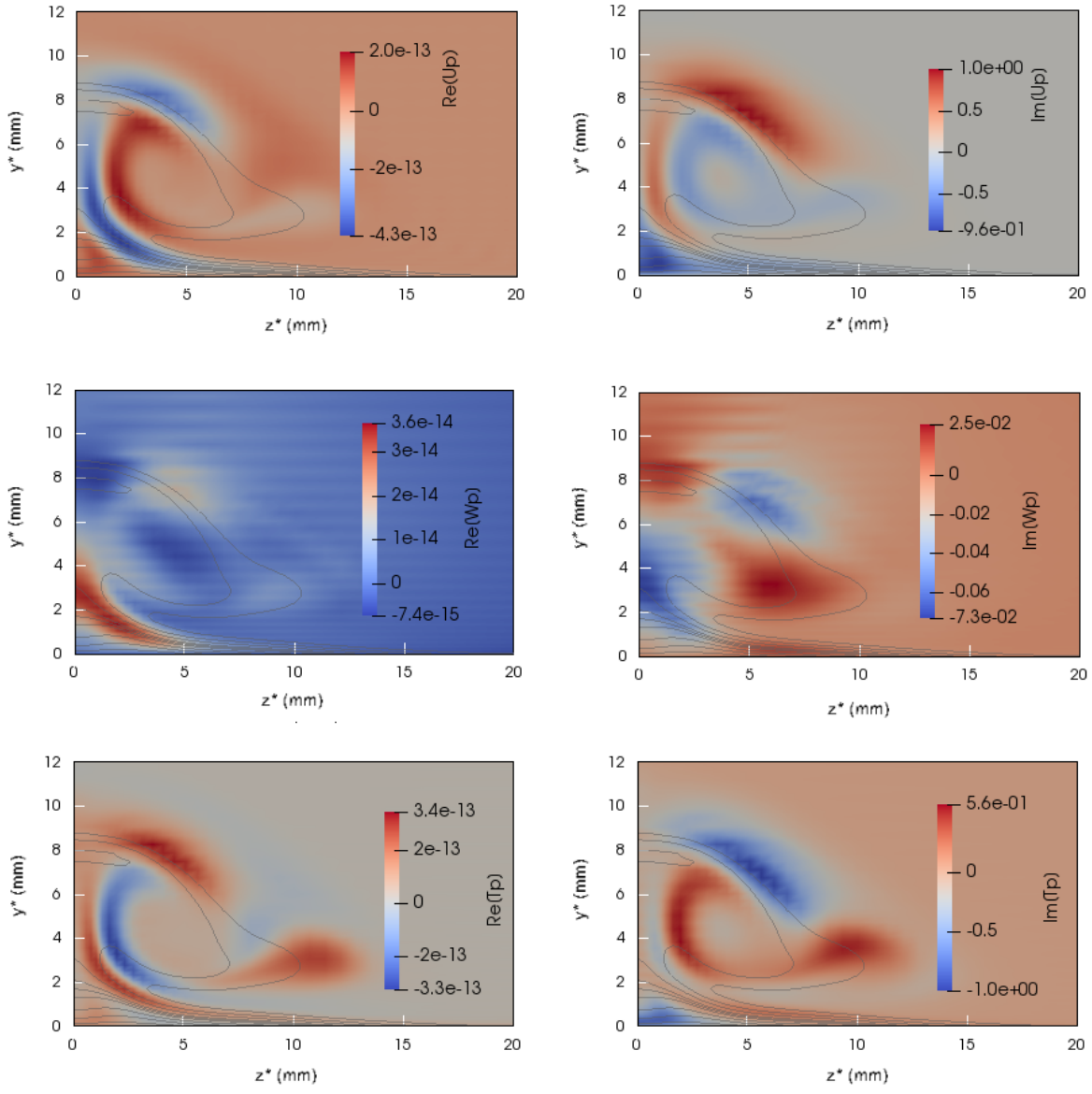

Figure 8.26: Real (left column) and Imaginary (right column) part of the streamwise (top row), spanwise (middle row) and temperature (lower row) amplitude functions of the unstable symmetric mode $\omega = (0 + \mathrm{i}\ 0.003946)$. The iso-lines correspond to the streamwise velocity component of the base flow.

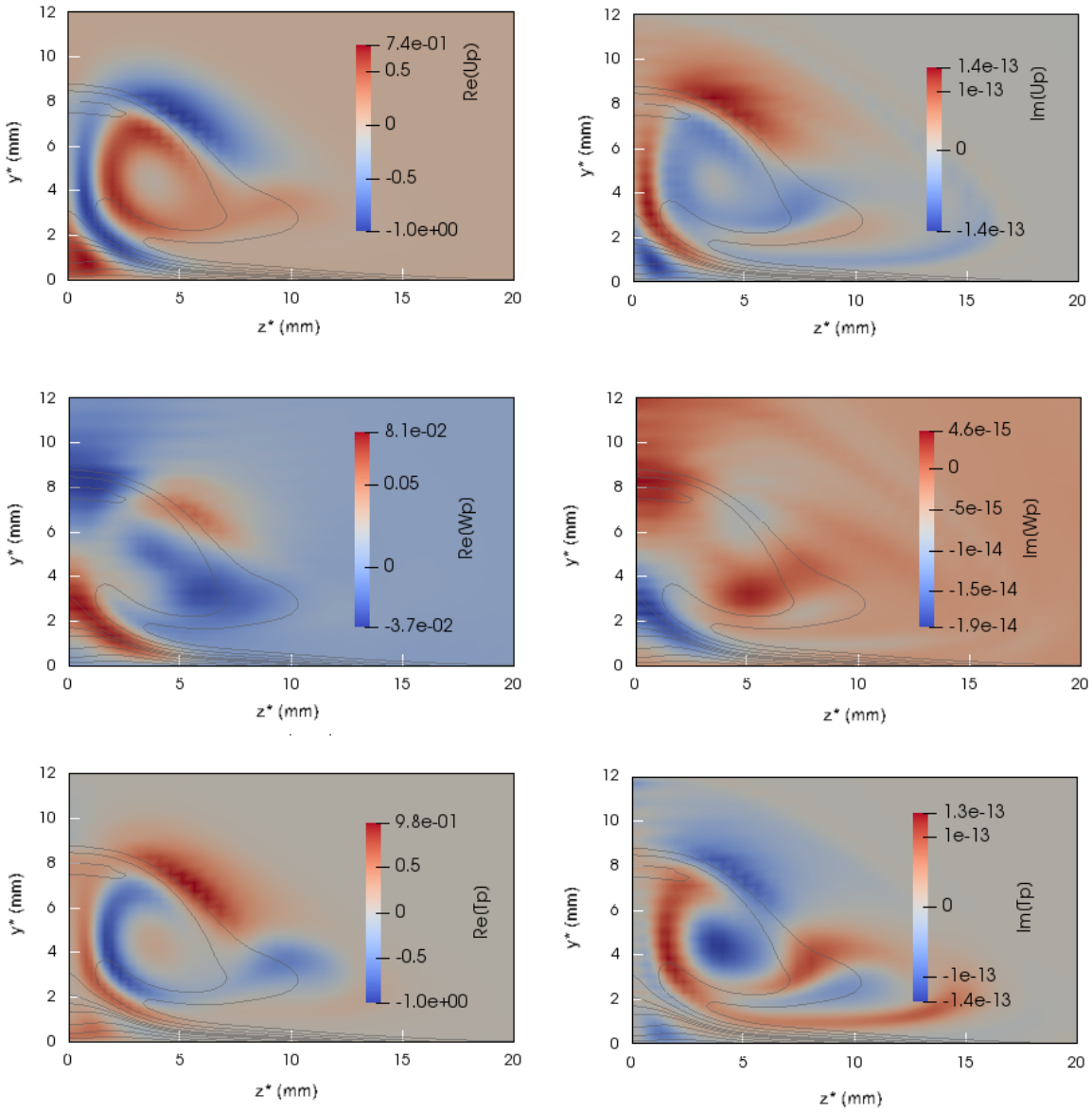

Figure 8.27: Real (left column) and Imaginary (right column) part of the streamwise (top row), spanwise (middle row) and temperature (lower row) amplitude functions of the unstable antisymmetric mode $\omega = (0 + \mathrm{i}\ 0.003634)$

Chapter 9

Summary and Future Work

Transient growth theory, underpinning non-modal (algebraic) short-time energy growth in shear flows has been revisited and extended to address global instability of compressible flows in geometries with multiple inhomogeneous spatial directions. It was shown that transient amplification may be mathematically associated with the non-orthogonal eigenvector basis and can be active even though the spectrum of the eigenvalues obtained in modal analysis of a given flow is entirely confined to the stable half-plane. Geometric and quantitative examples were provided to describe the nature of non-normal operators. The energy norm proposed by Mack (1969) in the context of modal instability and re-derived by Hanifi et al. (1996a) to quantify transient growth of the compressible boundary layer was also used in the present analysis. The concept of optimal disturbances that optimize energy amplification was introduced, alongside a detailed discussion of the linear algebra operations needed to calculate such linear optimals. These concepts, which are independent of the dimensionality of the underlying linearized Navier-Stokes equation, were developed in the framework of the present effort to address global linear instability of arbitrarily complex three-dimensional flows with multiple inhomogeneous spatial directions; the algorithms developed were then applied to analyze nonmodal instability of hypersonic flow on an elliptic cone at zero angle of attack.

The potential for transient growth on the elliptic cone was first analyzed in a local context. Parametric studies were performed at several locations along the cone surface, varying the azimuthal direction such that physical instability phenomena known to exist from the modal analysis (attachment-line, crossflow or centerline instabilities) could be followed seamlessly. Nonmodal flow instability at two different altitudes, 33km and 21km at which the Reynolds number changes by an order of magnitude, was analyzed. The results showed that multiple linear eigenmodes indeed are present at both altitudes. Moreover, transient growth has been discovered for the first time at the cross-flow region of the elliptic cone geometry. It was shown that an increase in altitude, with the consequent decrease in Reynolds number, promotes transient energy growth. Conversely, at the lower altitude - higher Reynolds number, modal instability is the predominant transition mechanism.

Qualitative comparisons with experiments were performed, monitoring the spacing between streamwise-aligned structures appearing as result of the present non-modal analysis and the cross-flow vortices documented in previous experiments (Borg et al. 2012). Notwithstanding the fact that the experimental Reynolds number lies between those at the two altitudes analyzed, non-modal analysis results obtained indicate that streamwise-aligned structures identified as linear optimal perturbations in the analysis correlate well with streamwise oriented structures found in the experiments, the order of magnitude of the spanwise spacing of the structures in question being identical in theory and experiment.

The compressible global non-modal analysis over the elliptic cone has been investigated for the first time in the framework of the present effort. Its results confirmed those found in the local nonmodal analysis, without resorting to the restrictive spanwise homogeneity assumption of local theory. Global linear optimal disturbances were calculated in a temporal framework and, at the centerline region examined, were found to evolve into modal, exponentially amplifying perturbations in the limit of asymptotically large time-horizon. Furthermore, the growth rate

predicted from the logarithmic derivative of the gain function - solution of the initial value problem at asymptotic times and the eigenvalue predicted for the most unstable eigenvalue in a modal analysis framework are in excellent agreement with each other. This finding is a cross-validation of the global transient growth implementation and verifies the previous investigations from a physical point of view, namely that the modal scenario dominates at the elliptic cone centerline region. The most significant finding of the global nonmodal analysis was that an increase in altitude and the consequent decrease in Reynolds number promote nonmodal transient growth at short time horizons.

The nonlinear three-dimensional (plane-marching) Parabolized Stability Equations (NL-PSE3D) code has been validated with well-known flow instability mechanisms, such as streamwise-oriented and crossflow linear disturbances. Further development and exploitation of this technology by Dr. Paredes is currently underway at NASA Langley.

Finally, the limitations of the computational approach employed in our previous modal and non-modal work in terms of its parallel (in)efficiency when applied to the solution of very large EVP and SVD problems were addressed by the development of a new massively parallel solver for the linearized Navier-Stokes equations in generalized three-dimensional coordinates. The LiGHT (Linear Global instability for Hypersonic Transition) code developed has advanced to the point of being able to solve massively parallel real and complex non-symmetric matrix EVP and SVD problems. It is expected that the LiGHT code, updates of the code are delivered to AFRL as they become available, will set new standards in laminar-turbulent transition research by permitting addressing modal or nonmodal flow instability in arbitrarily complex geometries from the incompressible to the hypersonic regime.

Appendix A

Compressible Navier-Stokes equations in generalized coordinates

The compressible Navier-Stokes equations in a general three-dimensional coordinate system are presented below.

A.1 Continuity

$$\frac{\partial \rho}{\partial t} + \nabla.(\rho \mathbf{V}) = 0, \tag{A.1}$$

Applying the chain rule (2.14) to the continuity equation (A.1) leads to

$$\begin{aligned} &\frac{\partial \rho}{\partial t} + \rho\left(\frac{\partial \zeta}{\partial x}\frac{\partial u}{\partial \zeta} + \frac{\partial \eta}{\partial x}\frac{\partial u}{\partial \eta} + \frac{\partial \xi}{\partial x}\frac{\partial u}{\partial \xi} + \frac{\partial \zeta}{\partial y}\frac{\partial v}{\partial \zeta} + \frac{\partial \eta}{\partial y}\frac{\partial v}{\partial \eta} + \frac{\partial \xi}{\partial y}\frac{\partial v}{\partial \xi} + \frac{\partial \zeta}{\partial z}\frac{\partial w}{\partial \zeta} + \frac{\partial \eta}{\partial z}\frac{\partial w}{\partial \eta} + \frac{\partial \xi}{\partial z}\frac{\partial w}{\partial \xi}\right) + \\ &u\left(\frac{\partial \zeta}{\partial x}\frac{\partial \rho}{\partial \zeta} + \frac{\partial \eta}{\partial x}\frac{\partial \rho}{\partial \eta} + \frac{\partial \xi}{\partial x}\frac{\partial \rho}{\partial \xi}\right) + v\left(\frac{\partial \zeta}{\partial y}\frac{\partial \rho}{\partial \zeta} + \frac{\partial \eta}{\partial y}\frac{\partial \rho}{\partial \eta} + \frac{\partial \xi}{\partial y}\frac{\partial \rho}{\partial \xi}\right) + w\left(\frac{\partial \zeta}{\partial z}\frac{\partial \rho}{\partial \zeta} + \frac{\partial \eta}{\partial z}\frac{\partial \rho}{\partial \eta} + \frac{\partial \xi}{\partial z}\frac{\partial \rho}{\partial \xi}\right) = 0 \end{aligned} \tag{A.2}$$

A.2 Momentum equation

The momentum equation along the $x-$direction is

$$\begin{aligned} \rho\frac{\partial u}{\partial t} + \rho\Bigg[&v\left(\frac{\partial \zeta}{\partial y}\frac{\partial u}{\partial \zeta} + \frac{\partial \eta}{\partial y}\frac{\partial u}{\partial \eta} + \frac{\partial \xi}{\partial y}\frac{\partial u}{\partial \xi}\right) + w\left(\frac{\partial \zeta}{\partial z}\frac{\partial u}{\partial \zeta} + \frac{\partial \eta}{\partial z}\frac{\partial u}{\partial \eta} + \frac{\partial \xi}{\partial z}\frac{\partial u}{\partial \xi}\right) + \\ &u\left(\frac{\partial \zeta}{\partial x}\frac{\partial u}{\partial \zeta} + \frac{\partial \eta}{\partial x}\frac{\partial u}{\partial \eta} + \frac{\partial \xi}{\partial x}\frac{\partial u}{\partial \xi}\right)\Bigg] + \frac{\partial \zeta}{\partial x}\frac{\partial p}{\partial \zeta} + \frac{\partial \eta}{\partial x}\frac{\partial p}{\partial \eta} + \frac{\partial \xi}{\partial x}\frac{\partial p}{\partial \xi} + \nabla.\tau \end{aligned} \tag{A.3}$$

where the three components of the stress tensor are

$$\tau_{1,1} = \lambda\left(\frac{\partial\zeta}{\partial x}\frac{\partial u}{\partial\zeta} + \frac{\partial\eta}{\partial x}\frac{\partial u}{\partial\eta} + \frac{\partial\xi}{\partial x}\frac{\partial u}{\partial\xi} + \frac{\partial\zeta}{\partial y}\frac{\partial v}{\partial\zeta} + \frac{\partial\eta}{\partial y}\frac{\partial v}{\partial\eta} + \frac{\partial\xi}{\partial y}\frac{\partial v}{\partial\xi} + \frac{\partial\zeta}{\partial z}\frac{\partial w}{\partial\zeta} + \frac{\partial\eta}{\partial z}\frac{\partial w}{\partial\eta} + \frac{\partial\xi}{\partial z}\frac{\partial w}{\partial\xi}\right) + 2\mu\left(\frac{\partial\zeta}{\partial x}\frac{\partial u}{\partial\zeta} + \frac{\partial\eta}{\partial x}\frac{\partial u}{\partial\eta} + \frac{\partial\xi}{\partial x}\frac{\partial u}{\partial\xi}\right)$$

$$\tau_{1,2} = \mu\left(\frac{\partial\zeta}{\partial y}\frac{\partial u}{\partial\zeta} + \frac{\partial\eta}{\partial y}\frac{\partial u}{\partial\eta} + \frac{\partial\xi}{\partial y}\frac{\partial u}{\partial\xi} + \frac{\partial\zeta}{\partial x}\frac{\partial v}{\partial\zeta} + \frac{\partial\eta}{\partial x}\frac{\partial v}{\partial\eta} + \frac{\partial\xi}{\partial x}\frac{\partial v}{\partial\xi}\right) \tag{A.4}$$

$$\tau_{1,3} = \mu\left(\frac{\partial\zeta}{\partial z}\frac{\partial u}{\partial\zeta} + \frac{\partial\eta}{\partial z}\frac{\partial u}{\partial\eta} + \frac{\partial\xi}{\partial z}\frac{\partial u}{\partial\xi} + \frac{\partial\zeta}{\partial x}\frac{\partial w}{\partial\zeta} + \frac{\partial\eta}{\partial x}\frac{\partial w}{\partial\eta} + \frac{\partial\xi}{\partial x}\frac{\partial w}{\partial\xi}\right)$$

Analogous expressions have been derived in the other two spatial directions.

A.3 Energy equation

$$
\begin{aligned}
&\frac{\partial p}{\partial t}+\left[v\left(\frac{\partial \zeta}{\partial y}\frac{\partial p}{\partial \zeta}+\frac{\partial \eta}{\partial y}\frac{\partial p}{\partial \eta}+\frac{\partial \xi}{\partial y}\frac{\partial p}{\partial \xi}\right)+w\left(\frac{\partial \zeta}{\partial z}\frac{\partial p}{\partial \zeta}+\frac{\partial \eta}{\partial z}\frac{\partial p}{\partial \eta}+\frac{\partial \xi}{\partial z}\frac{\partial p}{\partial \xi}\right)+u\left(\frac{\partial \zeta}{\partial x}\frac{\partial p}{\partial \zeta}+\frac{\partial \eta}{\partial x}\frac{\partial p}{\partial \eta}+\frac{\partial \xi}{\partial x}\frac{\partial p}{\partial \xi}\right)\right]+\\
&\gamma\, p\left[\left(\frac{\partial \zeta}{\partial x}\frac{\partial u}{\partial \zeta}+\frac{\partial \eta}{\partial x}\frac{\partial u}{\partial \eta}+\frac{\partial \xi}{\partial x}\frac{\partial u}{\partial \xi}\right)+\left(\frac{\partial \zeta}{\partial y}\frac{\partial v}{\partial \zeta}+\frac{\partial \eta}{\partial y}\frac{\partial v}{\partial \eta}+\frac{\partial \xi}{\partial y}\frac{\partial v}{\partial \xi}\right)+\left(\frac{\partial \zeta}{\partial z}\frac{\partial w}{\partial \zeta}+\frac{\partial \eta}{\partial z}\frac{\partial w}{\partial \eta}+\frac{\partial \xi}{\partial z}\frac{\partial w}{\partial \xi}\right)\right]+\\
&\left(\frac{\partial k}{\partial \zeta}\frac{\partial \zeta}{\partial x}+\frac{\partial k}{\partial \eta}\frac{\partial \eta}{\partial x}+\frac{\partial k}{\partial \xi}\frac{\partial \xi}{\partial x}\right)\left(\frac{\partial T}{\partial \zeta}\frac{\partial \zeta}{\partial x}+\frac{\partial T}{\partial \eta}\frac{\partial \eta}{\partial x}+\frac{\partial T}{\partial \xi}\frac{\partial \xi}{\partial x}\right)+\left(\frac{\partial k}{\partial \zeta}\frac{\partial \zeta}{\partial y}+\frac{\partial k}{\partial \eta}\frac{\partial \eta}{\partial y}+\frac{\partial k}{\partial \xi}\frac{\partial \xi}{\partial y}\right)\left(\frac{\partial T}{\partial \zeta}\frac{\partial \zeta}{\partial y}+\right.\\
&\left.\frac{\partial T}{\partial \eta}\frac{\partial \eta}{\partial y}+\frac{\partial T}{\partial \xi}\frac{\partial \xi}{\partial y}\right)+\left(\frac{\partial k}{\partial \zeta}\frac{\partial \zeta}{\partial z}+\frac{\partial k}{\partial \eta}\frac{\partial \eta}{\partial z}+\frac{\partial k}{\partial \xi}\frac{\partial \xi}{\partial z}\right)\left(\frac{\partial T}{\partial \zeta}\frac{\partial \zeta}{\partial z}+\frac{\partial T}{\partial \eta}\frac{\partial \eta}{\partial z}+\frac{\partial T}{\partial \xi}\frac{\partial \xi}{\partial z}\right)+\\
&k\left[\frac{\partial^2 T}{\partial \zeta^2}\left(\frac{\partial \zeta}{\partial x}\right)^2+2\left(\frac{\partial \eta}{\partial x}\frac{\partial^2 T}{\partial \eta\,\partial \zeta}+\frac{\partial \xi}{\partial x}\frac{\partial^2 T}{\partial \xi\,\partial \zeta}\right)\frac{\partial \zeta}{\partial x}+\frac{\partial^2 T}{\partial \eta^2}\left(\frac{\partial \eta}{\partial x}\right)^2\right.\\
&+\frac{\partial^2 T}{\partial \xi^2}\left(\frac{\partial \xi}{\partial x}\right)^2+\frac{\partial T}{\partial \zeta}\frac{\partial^2 \zeta}{\partial x^2}+\frac{\partial T}{\partial \eta}\frac{\partial^2 \eta}{\partial x^2}+\frac{\partial T}{\partial \xi}\frac{\partial^2 \xi}{\partial x^2}+\\
&2\frac{\partial \eta}{\partial x}\frac{\partial \xi}{\partial x}\frac{\partial^2 T}{\partial \xi \partial \eta}+\frac{\partial^2 T}{\partial \zeta^2}\left(\frac{\partial \zeta}{\partial y}\right)^2+2\left(\frac{\partial \eta}{\partial y}\frac{\partial^2 T}{\partial \eta\,\partial \zeta}+\frac{\partial \xi}{\partial y}\frac{\partial^2 T}{\partial \xi \partial \zeta}\right)\frac{\partial \zeta}{\partial y}+\\
&\frac{\partial^2 T}{\partial \eta^2}\left(\frac{\partial \eta}{\partial y}\right)^2+\frac{\partial^2 T}{\partial \xi^2}\left(\frac{\partial \xi}{\partial y}\right)^2+\frac{\partial T}{\partial \zeta}\frac{\partial^2 \zeta}{\partial y^2}+\frac{\partial T}{\partial \eta}\frac{\partial^2 \eta}{\partial y^2}+\\
&\frac{\partial T}{\partial \xi}\frac{\partial^2 \xi}{\partial y^2}+2\frac{\partial \eta}{\partial y}\frac{\partial \xi}{\partial y}\frac{\partial^2 T}{\partial \xi\,\partial \eta}+\left(\frac{\partial^2 T}{\partial \zeta^2}\left(\frac{\partial \zeta}{\partial z}\right)^2+2\left(\frac{\partial \eta}{\partial z}\frac{\partial^2 T}{\partial \eta\,\partial \zeta}+\right.\right.\\
&\left.\frac{\partial \xi}{\partial z}\frac{\partial^2 T}{\partial \xi\,\partial \zeta}\right)\frac{\partial \zeta}{\partial z}+\frac{\partial^2 T}{\partial \eta^2}\left(\frac{\partial \eta}{\partial z}\right)^2+\frac{\partial^2 T}{\partial \xi^2}\left(\frac{\partial \xi}{\partial z}\right)^2+\\
&\left.\left.\frac{\partial T}{\partial \zeta}\frac{\partial^2 \zeta}{\partial z^2}+\frac{\partial T}{\partial \eta}\frac{\partial^2 \eta}{\partial z^2}+\frac{\partial T}{\partial \xi}\frac{\partial^2 \xi}{\partial z^2}+2\frac{\partial \eta}{\partial z}\frac{\partial \xi}{\partial z}\frac{\partial^2 T}{\partial \xi\,\partial \eta}\right]\right.\\
&\mu\left[\left(\frac{\partial v}{\partial \zeta}\frac{\partial \zeta}{\partial x}+\frac{\partial u}{\partial \zeta}\frac{\partial \zeta}{\partial y}+\frac{\partial v}{\partial \eta}\frac{\partial \eta}{\partial x}+\frac{\partial u}{\partial \eta}\frac{\partial \eta}{\partial y}+\frac{\partial v}{\partial \xi}\frac{\partial \xi}{\partial x}+\frac{\partial u}{\partial \xi}\frac{\partial \xi}{\partial y}\right)^2+\right.\\
&\left(\frac{\partial w}{\partial \zeta}\frac{\partial \zeta}{\partial x}+\frac{\partial u}{\partial \zeta}\frac{\partial \zeta}{\partial z}+\frac{\partial w}{\partial \eta}\frac{\partial \eta}{\partial x}+\frac{\partial u}{\partial \eta}\frac{\partial \eta}{\partial z}+\frac{\partial w}{\partial \xi}\frac{\partial \xi}{\partial x}+\frac{\partial u}{\partial \xi}\frac{\partial \xi}{\partial z}\right)^2+\\
&\left.\left(\frac{\partial w}{\partial \zeta}\frac{\partial \zeta}{\partial y}+\frac{\partial v}{\partial \zeta}\frac{\partial \zeta}{\partial z}+\frac{\partial w}{\partial \eta}\frac{\partial \eta}{\partial y}+\frac{\partial v}{\partial \eta}\frac{\partial \eta}{\partial z}+\frac{\partial w}{\partial \xi}\frac{\partial \xi}{\partial y}+\frac{\partial v}{\partial \xi}\frac{\partial \xi}{\partial z}\right)^2\right]+\\
&\left(\frac{\partial u}{\partial \zeta}\frac{\partial \zeta}{\partial x}+\frac{\partial u}{\partial \eta}\frac{\partial \eta}{\partial x}+\frac{\partial u}{\partial \xi}\frac{\partial \xi}{\partial x}\right)\left[\lambda\left(\frac{\partial u}{\partial \zeta}\frac{\partial \zeta}{\partial x}+\frac{\partial v}{\partial \zeta}\frac{\partial \zeta}{\partial y}+\frac{\partial w}{\partial \zeta}\frac{\partial \zeta}{\partial z}+\frac{\partial u}{\partial \eta}\frac{\partial \eta}{\partial x}+\frac{\partial v}{\partial \eta}\frac{\partial \eta}{\partial y}+\right.\right.\\
&\left.\left.\frac{\partial w}{\partial \eta}\frac{\partial \eta}{\partial z}+\frac{\partial u}{\partial \xi}\frac{\partial \xi}{\partial x}+\frac{\partial v}{\partial \xi}\frac{\partial \xi}{\partial y}+\frac{\partial w}{\partial \xi}\frac{\partial \xi}{\partial z}\right)2\mu\left(\frac{\partial u}{\partial \zeta}\frac{\partial \zeta}{\partial x}+\frac{\partial u}{\partial \eta}\frac{\partial \eta}{\partial x}+\frac{\partial u}{\partial \xi}\frac{\partial \xi}{\partial x}\right)\right]+\\
&\left(\frac{\partial v}{\partial \zeta}\frac{\partial \zeta}{\partial y}+\frac{\partial v}{\partial \eta}\frac{\partial \eta}{\partial y}+\frac{\partial v}{\partial \xi}\frac{\partial \xi}{\partial y}\right)\left[\lambda\left(\frac{\partial u}{\partial \zeta}\frac{\partial \zeta}{\partial x}+\frac{\partial v}{\partial \zeta}\frac{\partial \zeta}{\partial y}+\frac{\partial w}{\partial \zeta}\frac{\partial \zeta}{\partial z}+\frac{\partial u}{\partial \eta}\frac{\partial \eta}{\partial x}+\frac{\partial v}{\partial \eta}\frac{\partial \eta}{\partial y}+\right.\right.\\
&\left.\left.\frac{\partial w}{\partial \eta}\frac{\partial \eta}{\partial z}+\frac{\partial u}{\partial \xi}\frac{\partial \xi}{\partial x}+\frac{\partial v}{\partial \xi}\frac{\partial \xi}{\partial y}+\frac{\partial w}{\partial \xi}\frac{\partial \xi}{\partial z}\right)+2\mu\left(\frac{\partial v}{\partial \zeta}\frac{\partial \zeta}{\partial y}+\frac{\partial v}{\partial \eta}\frac{\partial \eta}{\partial y}+\frac{\partial v}{\partial \xi}\frac{\partial \xi}{\partial y}\right)\right]+\\
&\left(\frac{\partial w}{\partial \zeta}\frac{\partial \zeta}{\partial z}+\frac{\partial w}{\partial \eta}\frac{\partial \eta}{\partial z}+\frac{\partial w}{\partial \xi}\frac{\partial \xi}{\partial z}\right)\left[\lambda\left(\frac{\partial u}{\partial \zeta}\frac{\partial \zeta}{\partial x}+\frac{\partial v}{\partial \zeta}\frac{\partial \zeta}{\partial y}+\frac{\partial w}{\partial \zeta}\frac{\partial \zeta}{\partial z}+\frac{\partial u}{\partial \eta}\frac{\partial \eta}{\partial x}+\frac{\partial v}{\partial \eta}\frac{\partial \eta}{\partial y}+\right.\right.\\
&\left.\left.\frac{\partial w}{\partial \eta}\frac{\partial \eta}{\partial z}+\frac{\partial u}{\partial \xi}\frac{\partial \xi}{\partial x}+\frac{\partial v}{\partial \xi}\frac{\partial \xi}{\partial y}+\frac{\partial w}{\partial \xi}\frac{\partial \xi}{\partial z}\right)+2\mu\left(\frac{\partial w}{\partial \zeta}\frac{\partial \zeta}{\partial z}+\frac{\partial w}{\partial \eta}\frac{\partial \eta}{\partial z}+\frac{\partial w}{\partial \xi}\frac{\partial \xi}{\partial z}\right)\right]
\end{aligned}
\tag{A.5}
$$

Appendix B

Compressible BiGlobal LNSE in Cartesian coordinates

The entries of the matrices shown in (2.11) are

$$\begin{aligned}
\mathcal{A}_{11} &= -\frac{4}{3}\frac{\bar{\mu}}{Re}D_{xx} + \left[-\frac{4}{3}\frac{1}{Re}\frac{d\bar{\mu}}{dT}\bar{T}_x + \bar{\rho}\bar{u}\right]D_x - \frac{\bar{\mu}}{Re}D_{yy} + \left[-\frac{1}{Re}\frac{d\bar{\mu}}{dT}\bar{T}_y + \bar{\rho}\bar{v}\right]D_y \\
&\quad \frac{\beta^2\bar{\mu}}{Re} + \bar{\rho}\bar{u}_x + i\beta\bar{\rho}\bar{w} \\
\mathcal{A}_{12} &= -\frac{1}{3}\frac{\bar{\mu}}{Re}D_{xy} - \frac{1}{Re}\frac{\bar{\mu}}{dT}\bar{T}_y D_x + \frac{2}{3}\frac{1}{Re}\frac{d\bar{\mu}}{dT}\bar{T}_x D_y + \bar{\rho}\bar{u}_y \\
\mathcal{A}_{13} &= -\frac{i}{3}\frac{\beta}{Re}\bar{\mu}D_x + \frac{2}{3}\frac{i\beta}{Re}\frac{d\bar{\mu}}{dT}\bar{T}_x \\
\mathcal{A}_{14} &= -\frac{1}{Re}\frac{d\bar{\mu}}{dT}\left(\frac{4}{3}\bar{u}_x - \frac{2}{3}\bar{v}_y\right)D_x - \frac{1}{Re}\frac{d\bar{\mu}}{dT}(\bar{u}_y + \bar{v}_x)D_y - \\
&\frac{1}{Re}\frac{d\bar{\mu}}{dT}\left(i\beta\bar{w}_x + \frac{4}{3}\bar{u}_{xx} + \bar{u}_{yy} + \frac{1}{3}\bar{v}_{xy}\right) - \frac{1}{Re}\frac{d^2\bar{\mu}}{dT^2}\left(\frac{4}{3}\bar{T}_x\bar{u}_x + \bar{T}_y(\bar{u}_y + \bar{v}_x) - \frac{2}{3}\bar{T}_x\bar{v}_y\right) \\
&\quad -\frac{\bar{\rho}}{\bar{T}}(\bar{u}\bar{u}_x + \bar{v}\bar{u}_y) \\
\mathcal{A}_{15} &= D_x + \frac{\gamma Ma^2}{\bar{T}}(\bar{u}\bar{u}_x + \bar{v}\bar{u}_y) \\
\mathcal{B}_{11} &= i\bar{\rho}
\end{aligned} \tag{B.1}$$

$$\begin{aligned}
\mathcal{A}_{21} &= -\frac{1}{3}\frac{\bar{\mu}}{Re}D_{xy} + \frac{2}{3}\frac{1}{Re}\frac{d\bar{\mu}}{dT}\bar{T}_y D_x - \frac{1}{Re}\frac{d\bar{\mu}}{dT}\bar{T}_x D_y + \bar{\rho}\bar{v}_x \\
\mathcal{A}_{22} &= -\frac{\bar{\mu}}{Re}D_{xx} + \left[-\frac{1}{Re}\frac{d\bar{\mu}}{dT}\bar{T}_x + \bar{\rho}\bar{u}\right]D_x - \frac{4}{3}\frac{\bar{\mu}}{Re}D_{yy} + \left[-\frac{4}{3}\frac{1}{Re}\frac{d\bar{\mu}}{dT}\bar{T}_y + \bar{\rho}\bar{v}\right]D_y + \\
&\quad \frac{\beta^2\bar{\mu}}{Re} + \bar{\rho}\bar{v}_y + i\beta\bar{\rho}\bar{w} \\
\mathcal{A}_{23} &= -\frac{i}{3}\frac{\beta}{Re}\bar{\mu}D_y + \frac{2}{3}\frac{i\beta}{Re}\frac{d\bar{\mu}}{dT}\bar{T}_y \\
\mathcal{A}_{24} &= -\frac{1}{Re}\frac{d\bar{\mu}}{dT}(\bar{u}_y + \bar{v}_x)D_x - \frac{1}{Re}\frac{d\bar{\mu}}{dT}\left(\frac{4}{3}\bar{v}_y - \frac{2}{3}\bar{u}_x\right)D_y - \\
&\frac{1}{Re}\frac{d\bar{\mu}}{dT}\left(i\beta\bar{w}_y + \frac{4}{3}\bar{v}_{yy} + \frac{1}{3}\bar{u}_{xy} + \bar{v}_{xx}\right) - \frac{1}{Re}\frac{d^2\bar{\mu}}{dT^2}\left(\frac{4}{3}\bar{T}_y\bar{v}_y + \bar{T}_x(\bar{u}_y + \bar{v}_y) - \frac{2}{3}\bar{T}_y\bar{u}_x\right) \\
&\quad -\frac{\bar{\rho}}{\bar{T}}(\bar{u}\bar{v}_x + \bar{v}\bar{v}_y) \\
\mathcal{A}_{25} &= D_y + \frac{\gamma Ma^2}{\bar{T}}(\bar{u}\bar{v}_x + \bar{v}\bar{v}_y) \\
\mathcal{B}_{22} &= i\bar{\rho}
\end{aligned} \tag{B.2}$$

$$
\begin{aligned}
\mathcal{A}_{31} &= -\frac{i}{3}\ \frac{\beta}{Re}\bar{\mu}D_x - \frac{i\beta}{Re}\frac{d\bar{\mu}}{dT}\bar{T}_x + \bar{\rho}\bar{w}_x \\
\mathcal{A}_{32} = \mathcal{A}_{31} &= -\frac{i}{3}\ \frac{\beta}{Re}\bar{\mu}D_y - \frac{i\beta}{Re}\frac{d\bar{\mu}}{dT}\bar{T}_y + \bar{\rho}\bar{w}_y \\
\mathcal{A}_{33} = -\frac{\bar{\mu}}{Re}D_{xx} - \frac{\bar{\mu}}{Re}D_{yy} &+ \Big[-\frac{1}{Re}\frac{d\bar{\mu}}{dT}\bar{T}_x + \bar{\rho}\bar{u}\Big]D_x + \Big[-\frac{1}{Re}\frac{d\bar{\mu}}{dT}\bar{T}_y + \bar{\rho}\bar{v}\Big]D_y + \\
&\frac{4}{3}\frac{\beta^2\bar{\mu}}{Re} + i\beta\bar{\rho}\bar{w} \\
\mathcal{A}_{34} &= -\frac{1}{Re}\frac{d\bar{\mu}}{dT}\bar{w}_x D_x - \frac{1}{Re}\frac{d\bar{\mu}}{dT}\bar{w}_y D_y - \\
\frac{1}{Re}\frac{d\bar{\mu}}{dT}\Big(\bar{w}_{xx} + \bar{w}_{yy} &- \frac{2}{3}i\beta(\bar{u}_x + \bar{v}_y) - \frac{1}{Re}\frac{d^2\bar{\mu}}{dT^2}(\bar{T}_x\bar{w}_x + \bar{T}_y(\bar{w}_y) - \frac{\bar{\rho}}{\bar{T}}(\bar{u}\bar{w}_x + \bar{v}\bar{w}_y) \\
\mathcal{A}_{35} &= i\beta + \frac{\gamma Ma^2}{\bar{T}}(\bar{u}\bar{w}_x + \bar{v}\bar{w}_y) \\
\mathcal{B}_{33} &= i\bar{\rho}
\end{aligned}
\tag{B.3}
$$

$$
\begin{aligned}
\mathcal{A}_{41} &= \Big[-2\frac{(\gamma-1)Ma^2}{Re}\bar{\mu}\Big(\frac{4}{3}\bar{u}_x - \frac{2}{3}\bar{v}_y\Big) + \gamma Ma^2\bar{p}D_x - 2\frac{(\gamma-1)Ma^2}{Re}\bar{\mu}(\bar{u}_y) + \bar{v}_x)D_y \\
&-2\frac{(\gamma-1)Ma^2}{Re}\bar{\mu}\bar{w}_x + Ma^2\bar{p}_x \\
\mathcal{A}_{42} &= -2\frac{(\gamma-1)Ma^2}{Re}\bar{\mu}(\bar{u}_y + \bar{v}_x)D_x + \Big[-2\frac{(\gamma-1)Ma^2}{Re}\bar{\mu}\Big(-\frac{2}{3}\bar{u}_x + \frac{4}{3}\bar{v}_y\Big) + \gamma Ma^2\bar{p}\Big]D_y \\
&-2\frac{(\gamma-1)Ma^2}{Re}\bar{\mu}\bar{w}_y + Ma^2\bar{p}_y \\
\mathcal{A}_{43} &= -2\frac{(\gamma-1)Ma^2}{Re}\bar{\mu}\bar{w}_x D_x - 2\frac{(\gamma-1)Ma^2}{Re}\bar{\mu}\bar{w}_y D_y + \frac{4}{3}\frac{i\beta(\gamma-1)Ma^2}{Re}\bar{\mu}(\bar{u}_x + \bar{v}_y) + i\beta\gamma Ma^2\bar{p} \\
\mathcal{A}_{44} &= -\frac{\bar{k}}{RePr}D_{xx} - \frac{2}{RePr}\frac{d\bar{k}}{dT}\bar{T}_x D_x - \frac{\bar{k}}{RePr}D_{yy} - \frac{2}{RePr}\frac{d\bar{k}}{dT}\bar{T}_y D_y + \\
&\frac{\beta^2\bar{k}}{RePr} - \frac{1}{RePr}\frac{d\bar{k}}{dT}(\bar{T}_{xx} + \bar{T}_{yy}) - \frac{1}{RePr}\frac{d^2\bar{k}}{dT^2}(\bar{T}_x^2 + \bar{T}_y^2) \\
&+\frac{(\gamma-1)Ma^2}{Re}\frac{d\bar{\mu}}{dT}\Big(\frac{2}{3}(\bar{u}_x + \bar{v}_y)^2 - (\bar{u}_y + \bar{v}_x)^2 - 2(\bar{u}_x^2 + \bar{v}_y^2) - \bar{w}_x^2 - \bar{w}_y^2\Big) \\
\mathcal{A}_{45} &= Ma^2\bar{u}D_x + Ma^2\bar{v}D_y + i\beta Ma^2\bar{w} + \gamma Ma^2(\bar{u}_x + \bar{v}_y) \\
\mathcal{B}_{45} &= iMa^2
\end{aligned}
\tag{B.4}
$$

$$
\begin{aligned}
\mathcal{A}_{51} &= \bar{\rho}D_x + \bar{\rho}_x \\
\mathcal{A}_{52} &= \bar{\rho}D_y + \bar{\rho}_y \\
\mathcal{A}_{53} &= i\beta\bar{\rho} \\
\mathcal{A}_{54} &= -\frac{\bar{\rho}}{\bar{T}}\bar{u}D_x - \frac{\bar{\rho}}{\bar{T}}\bar{v}D_y + \frac{\bar{\rho}}{\bar{T}}(-\bar{u}_x - \bar{v}_y - i\beta\bar{w}) + \frac{\bar{\rho}}{\bar{T}^2}(\bar{u}\bar{T}_x + \bar{v}\bar{T}_y) - \frac{1}{\bar{T}}(\bar{u}\bar{\rho}_x + \bar{v}\bar{\rho}_y) \\
\mathcal{A}_{55} &= \gamma Ma^2\frac{\bar{u}}{\bar{T}}D_x + \gamma Ma^2\frac{\bar{v}}{\bar{T}}D_y - \frac{\gamma Ma^2}{\bar{T}^2}(\bar{u}\bar{T}_x + \bar{v}\bar{T}_y) + \frac{\gamma Ma^2}{\bar{T}}(\bar{u}_x + \bar{v}_y + i\beta\bar{w}) \\
\mathcal{B}_{54} &= -\frac{i\bar{\rho}}{\bar{T}} \\
\mathcal{B}_{55} &= \gamma Ma^2\frac{i}{\bar{T}}
\end{aligned}
\tag{B.5}
$$

Appendix C

Compressible BiGlobal LNSE in elliptic confocal coordinates

Recalling that the transformation from the physical coordinate system (x, y, z) into the computational coordinate system (ξ, η, ζ) is made using the follow orthogonal elliptic confocal transformation

$$x = c\ \cosh(\xi)\cos(\eta), \qquad y = c\ \sinh(\xi)\sin(\eta), \qquad z = \zeta \tag{C.1}$$

where c = 2/ $\sinh(\eta_0)$ sets the half angle of the cone minor-axis and η_0 is a parameter controlling the Aspect Ratio (AR) of the cone, $\eta_0 = \text{atanh}(1/\text{AR})$.
In terms of the elliptic confocal coordinates, the instantaneous position vector is expressed as

$$\overline{r} = c\ \cosh(\xi)\cos(\eta)\ \hat{i} + c\ \sinh(\xi)\sin(\eta)\ \hat{j} + z\ \hat{k} \tag{C.2}$$

and the unit elliptic confocal vectors is expressed in terms of the Cartesian unit vector $(\hat{i}, \hat{j}, \hat{k})$ as

$$x = \frac{\sinh(\xi)\cos(\eta)\hat{i} + \cosh(\xi)\sin(\eta)\hat{j}}{\sqrt{(\sinh^2(\xi) + \sin^2(\eta))}} \qquad y = -\frac{\cosh(\xi)\sin(\eta)\hat{i} + \sinh(\xi)\cos(\eta)\hat{j}}{\sqrt{(\sinh^2(\xi) + \sin^2(\eta))}} \qquad z = \hat{k} \tag{C.3}$$

Substituting the above transformation in the generalized BiGlobal equations leads to

C.1 Linearised continuity equation in elliptic confoal coordinates

$$
\begin{aligned}
\frac{1}{\bar{T}^2}\Bigg[\bar{T}\Bigg(c\sinh(\xi)\cos(\eta)\Bigg(\gamma\mathrm{Ma}^2\bar{u}\frac{\partial\hat{p}}{\partial\xi}+\gamma\mathrm{Ma}^2\hat{p}\Bigg(\frac{\partial\bar{u}}{\partial\xi}+\frac{\partial\bar{v}}{\partial\eta}\Bigg)+\gamma\mathrm{Ma}^2\bar{v}\frac{\partial\hat{p}}{\partial\eta}-\\
\hat{T}\bar{u}\frac{\partial\bar{\rho}}{\partial\xi}-\bar{\rho}\Bigg(\bar{u}\frac{\partial\hat{T}}{\partial\xi}+\hat{T}\Bigg(\frac{\partial\bar{u}}{\partial\xi}+\frac{\partial\bar{v}}{\partial\eta}\Bigg)+\bar{v}\frac{\partial\hat{T}}{\partial\eta}\Bigg)-\hat{T}\bar{v}\frac{\partial\bar{\rho}}{\partial\eta}\Bigg)+\\
c\cosh(\xi)\sin(\eta)\Bigg(\gamma\mathrm{Ma}^2\bar{u}\frac{\partial\hat{p}}{\partial\eta}+\gamma\mathrm{Ma}^2\hat{p}\Bigg(\frac{\partial\bar{u}}{\partial\eta}-\frac{\partial\bar{v}}{\partial\xi}\Bigg)-\gamma\mathrm{Ma}^2\bar{v}\frac{\partial\hat{p}}{\partial\xi}-\hat{T}\bar{u}\frac{\partial\bar{\rho}}{\partial\eta}\\
+\bar{\rho}\Bigg(\bar{u}\Bigg(-\frac{\partial\hat{T}}{\partial\eta}\Bigg)+\hat{T}\Bigg(\frac{\partial\bar{v}}{\partial\xi}-\frac{\partial\bar{u}}{\partial\eta}\Bigg)+\bar{v}\frac{\partial\hat{T}}{\partial\xi}\Bigg)+\hat{T}\bar{v}\frac{\partial\bar{\rho}}{\partial\xi}\Bigg)-\\
i\Bigg(\gamma\mathrm{Ma}^2\hat{p}-\hat{T}\bar{\rho}\Bigg)\Bigg(\omega-\beta\bar{w}\Bigg)\Bigg)+\\
c\Bigg(\gamma\mathrm{Ma}^2\hat{p}-\hat{T}\bar{\rho}\Bigg)\Bigg(\frac{\partial\bar{T}}{\partial\xi}\Bigg(\cosh(\xi)\sin(\eta)\bar{v}-\sinh(\xi)\cos(\eta)\bar{u}\Bigg)-\\
\frac{\partial\bar{T}}{\partial\eta}\Bigg(\cosh(\xi)\sin(\eta)\bar{u}+\sinh(\xi)\cos(\eta)\bar{v}\Bigg)\Bigg)+\\
\bar{T}^2\Bigg(c\sinh(\xi)\cos(\eta)\Bigg(\hat{u}\frac{\partial\bar{\rho}}{\partial\xi}+\bar{\rho}\Bigg(\frac{\partial\hat{u}}{\partial\xi}+\frac{\partial\hat{v}}{\partial\eta}\Bigg)+\hat{v}\frac{\partial\bar{\rho}}{\partial\eta}\Bigg)+\\
c\cosh(\xi)\sin(\eta)\Bigg(\hat{u}\frac{\partial\bar{\rho}}{\partial\eta}+\bar{\rho}\Bigg(\frac{\partial\hat{u}}{\partial\eta}-\frac{\partial\hat{v}}{\partial\xi}\Bigg)-\hat{v}\frac{\partial\bar{\rho}}{\partial\xi}\Bigg)+i\beta\bar{\rho}\hat{w}\Bigg)\Bigg]=0
\end{aligned}
\tag{C.4}
$$

C.2 Linearized momentum equation along the ξ-direction in elliptic confocal coordinates

$$
\begin{aligned}
&-i\omega\hat{u}\bar{\rho} + \frac{1}{\bar{T}}\Bigg[c\sinh(\xi)\cos(\eta)\Bigg(\bar{u}\frac{\partial\bar{u}}{\partial\xi}\Bigg(\gamma\mathrm{Ma}^2\hat{p} - \hat{T}\bar{\rho}\Bigg)+\\
&\bar{v}\Bigg(\frac{\partial\bar{u}}{\partial\eta}\Bigg(\gamma\mathrm{Ma}^2\hat{p} - \hat{T}\bar{\rho}\Bigg) + \bar{\rho}\bar{T}\frac{\partial\hat{u}}{\partial\eta}\Bigg) + \bar{\rho}\bar{T}\Bigg(\bar{u}\frac{\partial\hat{u}}{\partial\xi} + \hat{u}\frac{\partial\bar{u}}{\partial\xi} + \hat{v}\frac{\partial\bar{u}}{\partial\eta}\Bigg)\Bigg)+\\
&c\cosh(\xi)\sin(\eta)\Bigg(\bar{u}\Bigg(\frac{\partial\bar{u}}{\partial\eta}\Bigg(\gamma\mathrm{Ma}^2\hat{p} - \hat{T}\bar{\rho}\Bigg) + \bar{\rho}\bar{T}\frac{\partial\hat{u}}{\partial\eta}\Bigg) + \bar{v}\frac{\partial\bar{u}}{\partial\xi}\Bigg(\hat{T}\bar{\rho} - \gamma\mathrm{Ma}^2\hat{p}\Bigg)+\\
&\bar{\rho}\bar{T}\Bigg(\hat{u}\frac{\partial\bar{u}}{\partial\eta} + \bar{v}\Bigg(-\frac{\partial\hat{u}}{\partial\xi}\Bigg) - \hat{v}\frac{\partial\bar{u}}{\partial\xi}\Bigg)\Bigg) + i\beta\hat{u}\bar{\rho}\bar{T}\bar{w}\Bigg]+\\
&\Bigg(c\sinh(\xi)\cos(\eta)\frac{\partial\hat{p}}{\partial\xi} + c\cosh(\xi)\sin(\eta)\frac{\partial\hat{p}}{\partial\eta} + i\beta\hat{p}\Bigg)+
\end{aligned}
\tag{C.5}
$$

$$
\begin{aligned}
&-\frac{1}{Re}\Bigg(\frac{\partial\hat{T}}{\partial\eta}\Bigg(\cosh(\xi)\frac{d\lambda}{dT}\sin(\eta)\Bigg(\cosh(\xi)\Bigg(\frac{\partial\bar{u}}{\partial\eta} - \frac{\partial\bar{v}}{\partial\xi}\Bigg)\sin(\eta) + \cos(\eta)\Bigg(\frac{\partial\bar{u}}{\partial\xi} + \frac{\partial\bar{v}}{\partial\eta}\Bigg)\sinh(\xi)\Bigg)\\
&+\frac{d\mu}{dT}\Bigg(\cos(\eta)\sinh(\xi)\Bigg(\cosh(\xi)\Bigg(\frac{\partial\bar{u}}{\partial\xi} + \frac{\partial\bar{v}}{\partial\eta}\Bigg)\sin(\eta) + \cos(\eta)\frac{\partial\bar{v}}{\partial\xi}\sinh(\xi)\Bigg)+\\
&\frac{\partial\bar{u}}{\partial\eta}\Bigg(2\cosh^2(\xi)\sin^2(\eta) + \cos^2(\eta)\sinh^2(\xi)\Bigg)\Bigg)\Bigg)c^2+\\
&\frac{\partial\hat{T}}{\partial\xi}\Bigg(\cos(\eta)\frac{d\lambda}{dT}\sinh(\xi)\Bigg(\cosh(\xi)\Bigg(\frac{\partial\bar{u}}{\partial\eta} - \frac{\partial\bar{v}}{\partial\xi}\Bigg)\sin(\eta) + \cos(\eta)\Bigg(\frac{\partial\bar{u}}{\partial\xi} + \frac{\partial\bar{v}}{\partial\eta}\Bigg)\sinh(\xi)\Bigg)+\\
&\frac{d\mu}{dT}\Bigg(-\cosh^2(\xi)\frac{\partial\bar{v}}{\partial\eta}\sin^2(\eta) + \cos(\eta)\cosh(\xi)\frac{\partial\bar{u}}{\partial\eta}\sinh(\xi)\sin(\eta) - \cos(\eta)\cosh(\xi)\frac{\partial\bar{v}}{\partial\xi}\sinh(\xi)\sin(\eta)+\\
&\frac{\partial\bar{u}}{\partial\xi}\Bigg(\cosh^2(\xi)\sin^2(\eta) + 2\cos^2(\eta)\sinh^2(\xi)\Bigg)\Bigg)\Bigg)c^2 + \Bigg(\Bigg(\cosh^2(\xi)\frac{\partial^2\hat{u}}{\partial\eta^2}\sin^2(\eta) - \cosh^2(\xi)\frac{\partial^2\hat{v}}{\partial\xi\,\partial\eta}\sin^2(\eta)+\\
&\cos(\eta)\cosh(\xi)\frac{\partial^2\hat{v}}{\partial\eta^2}\sinh(\xi)\sin(\eta) - \cos(\eta)\cosh(\xi)\frac{\partial^2\hat{v}}{\partial\xi^2}\sinh(\xi)\sin(\eta)+\\
&2\cos(\eta)\cosh(\xi)\frac{\partial^2\hat{u}}{\partial\xi\,\partial\eta}\sinh(\xi)\sin(\eta) + \cos^2(\eta)\frac{\partial^2\hat{u}}{\partial\xi^2}\sinh^2(\xi) + \cos^2(\eta)\frac{\partial^2\hat{v}}{\partial\xi\,\partial\eta}\sinh^2(\xi)\Bigg)\bar{\lambda}+\\
&\Bigg(\cosh^2(\xi)\frac{\partial^2\hat{u}}{\partial\xi^2}\sin^2(\eta) - \cosh^2(\xi)\frac{\partial^2\hat{v}}{\partial\xi\,\partial\eta}\sin^2(\eta) + \cos(\eta)\cosh(\xi)\frac{\partial^2\hat{v}}{\partial\eta^2}\sinh(\xi)\sin(\eta)-\\
&\cos(\eta)\cosh(\xi)\frac{\partial^2\hat{v}}{\partial\xi^2}\sinh(\xi)\sin(\eta) + 2\cos(\eta)\cosh(\xi)\frac{\partial^2\hat{u}}{\partial\xi\,\partial\eta}\sinh(\xi)\sin(\eta)+\\
&2\cos^2(\eta)\frac{\partial^2\hat{u}}{\partial\xi^2}\sinh^2(\xi) + \cos^2(\eta)\frac{\partial^2\hat{v}}{\partial\xi\,\partial\eta}\sinh^2(\xi)+\\
&\frac{\partial^2\hat{u}}{\partial\eta^2}\Bigg(2\cosh^2(\xi)\sin^2(\eta) + \cos^2(\eta)\sinh^2(\xi)\Bigg)\Bigg)\bar{\mu}\Bigg)c^2 + i\beta\cosh(\xi)\frac{\partial\hat{w}}{\partial\eta}\sin(\eta)\Bigg(\bar{\lambda} + \bar{\mu}\Bigg)c+\\
&i\beta\cos(\eta)\frac{\partial\hat{w}}{\partial\xi}\sinh(\xi)\Bigg(\bar{\lambda} + \bar{\mu}\Bigg)c - \frac{\partial\hat{v}}{\partial\xi}\Bigg(c\cos(\eta)\cosh(\xi)\frac{\partial\bar{T}}{\partial\xi}\Big(\frac{d\lambda}{dT} + \frac{d\mu}{dT}\Big)\sin(\eta)\sinh(\xi) + \sin(\eta)\bar{\lambda}\sinh(\xi)+\\
&\sin(\eta)\bar{\mu}\sinh(\xi) + c\frac{\partial\bar{T}}{\partial\eta}\Bigg(\cosh^2(\xi)\frac{d\lambda}{dT}\sin^2(\eta) - \cos^2(\eta)\frac{d\mu}{dT}\sinh^2(\xi)\Bigg)\Bigg)c+
\end{aligned}
\tag{C.6}
$$

$$\frac{\partial \hat{u}}{\partial \eta}\Bigg(c\cos(\eta)\cosh(\xi)\frac{\partial \bar{T}}{\partial \xi}(\frac{d\lambda}{dT}+\frac{d\mu}{dT})\sin(\eta)\sinh(\xi)+\sin(\eta)\bar{\lambda}\sinh(\xi)+\sin(\eta)\bar{\mu}\sinh(\xi)+$$
$$c\frac{\partial \bar{T}}{\partial \eta}\Bigg(\cosh^2(\xi)(\frac{d\lambda}{dT}+2\frac{d\mu}{dT})\sin^2(\eta)+\cos^2(\eta)\frac{d\mu}{dT}\sinh^2(\xi)\Bigg)\Bigg)c+$$
$$\frac{\partial \hat{v}}{\partial \eta}\Bigg(c\frac{\partial \bar{T}}{\partial \xi}\Bigg(\cos^2(\eta)\frac{d\lambda}{dT}\sinh^2(\xi)-\cosh^2(\xi)\frac{d\mu}{dT}\sin^2(\eta)\Bigg)+$$
$$\cos(\eta)\cosh(\xi)\Bigg(c\frac{\partial \bar{T}}{\partial \eta}(\frac{d\lambda}{dT}+\frac{d\mu}{dT})\sin(\eta)\sinh(\xi)+\bar{\lambda}+\bar{\mu}\Bigg)\Bigg)c+\frac{\partial \hat{u}}{\partial \xi}\Bigg(c\frac{\partial \bar{T}}{\partial \xi}\Bigg(\cosh^2(\xi)\frac{d\mu}{dT}\sin^2(\eta)$$
$$+\cos^2(\eta)(\frac{d\lambda}{dT}+2\frac{d\mu}{dT})\sinh^2(\xi)\Bigg)+\cos(\eta)\cosh(\xi)\Bigg(c\frac{\partial \bar{T}}{\partial \eta}(\frac{d\lambda}{dT}+\frac{d\mu}{dT})\sin(\eta)\sinh(\xi)+\bar{\lambda}+\bar{\mu}\Bigg)\Bigg)c+$$
$$\Bigg(\frac{d\lambda}{dT}\Bigg(c\cosh^2(\xi)\frac{\partial^2 \bar{u}}{\partial \eta^2}\sin^2(\eta)-c\cosh^2(\xi)\frac{\partial^2 \bar{v}}{\partial \xi\,\partial \eta}\sin^2(\eta)+\frac{\partial \bar{u}}{\partial \eta}\sinh(\xi)\sin(\eta)-\frac{\partial \bar{v}}{\partial \xi}\sinh(\xi)\sin(\eta)+$$
$$c\cos(\eta)\cosh(\xi)\frac{\partial^2 \bar{v}}{\partial \eta^2}\sinh(\xi)\sin(\eta)-c\cos(\eta)\cosh(\xi)\frac{\partial^2 \bar{v}}{\partial \xi^2}\sinh(\xi)\sin(\eta)+$$
$$2c\cos(\eta)\cosh(\xi)\frac{\partial^2 \bar{u}}{\partial \xi\,\partial \eta}\sinh(\xi)\sin(\eta)+c\cos^2(\eta)\frac{\partial^2 \bar{u}}{\partial \xi^2}\sinh^2(\xi)+c\cos^2(\eta)\frac{\partial^2 \bar{v}}{\partial \xi\,\partial \eta}\sinh^2(\xi)+$$
$$\cos(\eta)\cosh(\xi)\frac{\partial \bar{u}}{\partial \xi}+\cos(\eta)\cosh(\xi)\frac{\partial \bar{v}}{\partial \eta}\Bigg)+\frac{d\mu}{dT}\Bigg(2c\cosh^2(\xi)\frac{\partial^2 \bar{u}}{\partial \eta^2}\sin^2(\eta)+c\cosh^2(\xi)\frac{\partial^2 \bar{u}}{\partial \xi^2}\sin^2(\eta)-$$
$$c\cosh^2(\xi)\frac{\partial^2 \bar{v}}{\partial \xi\,\partial \eta}\sin^2(\eta)+i\beta\cosh(\xi)\frac{\partial \bar{w}}{\partial \eta}\sin(\eta)+\frac{\partial \bar{u}}{\partial \eta}\sinh(\xi)\sin(\eta)-\frac{\partial \bar{v}}{\partial \xi}\sinh(\xi)\sin(\eta)+ \tag{C.7}$$
$$c\cos(\eta)\cosh(\xi)\frac{\partial^2 \bar{v}}{\partial \eta^2}\sinh(\xi)\sin(\eta)-c\cos(\eta)\cosh(\xi)\frac{\partial^2 \bar{v}}{\partial \xi^2}\sinh(\xi)\sin(\eta)+2c\cos(\eta)\cosh(\xi)$$
$$\frac{\partial^2 \bar{u}}{\partial \xi\,\partial \eta}\sinh(\xi)\sin(\eta)+c\cos^2(\eta)\frac{\partial^2 \bar{u}}{\partial \eta^2}\sinh^2(\xi)+2c\cos^2(\eta)\frac{\partial^2 \bar{u}}{\partial \xi^2}\sinh^2(\xi)+$$
$$c\cos^2(\eta)\frac{\partial^2 \bar{v}}{\partial \xi\,\partial \eta}\sinh^2(\xi)+\cos(\eta)\cosh(\xi)\frac{\partial \bar{u}}{\partial \xi}+\cos(\eta)\cosh(\xi)\frac{\partial \bar{v}}{\partial \eta}+i\beta\cos(\eta)\frac{\partial \bar{w}}{\partial \xi}\sinh(\xi)\Bigg)+$$
$$c\Bigg(\frac{d^2\lambda}{dT^2}\Bigg(\cosh(\xi)\frac{\partial \bar{T}}{\partial \eta}\sin(\eta)+\cos(\eta)\frac{\partial \bar{T}}{\partial \xi}\sinh(\xi)\Bigg)\Bigg(\cosh(\xi)\Bigg(\frac{\partial \bar{u}}{\partial \eta}-\frac{\partial \bar{v}}{\partial \xi}\Bigg)\sin(\eta)+$$
$$\cos(\eta)\Bigg(\frac{\partial \bar{u}}{\partial \xi}+\frac{\partial \bar{v}}{\partial \eta}\Bigg)\sinh(\xi)\Bigg)+\mathrm{d2}\mu\mathrm{dT2b}\Bigg(\frac{\partial \bar{T}}{\partial \eta}\Bigg(\cos(\eta)\sinh(\xi)\Bigg(\cosh(\xi)\Bigg(\frac{\partial \bar{u}}{\partial \xi}+\frac{\partial \bar{v}}{\partial \eta}\Bigg)\sin(\eta)+$$
$$\cos(\eta)\frac{\partial \bar{v}}{\partial \xi}\sinh(\xi)\Bigg)+\frac{\partial \bar{u}}{\partial \eta}\Bigg(2\cosh^2(\xi)\sin^2(\eta)+\cos^2(\eta)\sinh^2(\xi)\Bigg)\Bigg)+$$
$$\frac{\partial \bar{T}}{\partial \xi}\Bigg(-\cosh^2(\xi)\frac{\partial \bar{v}}{\partial \eta}\sin^2(\eta)+\cos(\eta)\cosh(\xi)\frac{\partial \bar{u}}{\partial \eta}\sinh(\xi)\sin(\eta)-\cos(\eta)\cosh(\xi)\frac{\partial \bar{v}}{\partial \xi}\sinh(\xi)\sin(\eta)+$$
$$\frac{\partial \bar{u}}{\partial \xi}\Bigg(\cosh^2(\xi)\sin^2(\eta)+2\cos^2(\eta)\sinh^2(\xi)\Bigg)\Bigg)\Bigg)\Bigg)\Bigg)\hat{T}c+$$
$$i\beta\frac{d\lambda}{dT}\Bigg(\cosh(\xi)\frac{\partial \bar{T}}{\partial \eta}\sin(\eta)+\cos(\eta)\frac{\partial \bar{T}}{\partial \xi}\sinh(\xi)\Bigg)\hat{w}c-\beta^2\bar{\mu}\hat{u}\Bigg)=0.$$

The equations along the other two transformed spatial directions can be obtained in an analogous manner.

C.3 Linearized energy equation in elliptic confocal coordinates

$$
\begin{aligned}
Ma^2\Big\{ &- i\omega\hat{p} + c\sinh(\xi)\cos(\eta)\Big(\bar{u}\frac{\partial\hat{p}}{\partial\xi} + \hat{u}\frac{\partial\bar{p}}{\partial\xi} + \bar{v}\frac{\partial\hat{p}}{\partial\eta} + \hat{v}\frac{\partial\bar{p}}{\partial\eta}\Big) + \\
&c\cosh(\xi)\sin(\eta)\Big(\bar{u}\frac{\partial\hat{p}}{\partial\eta} + \hat{u}\frac{\partial\bar{p}}{\partial\eta} - \bar{v}\frac{\partial\hat{p}}{\partial\xi} - \hat{v}\frac{\partial\bar{p}}{\partial\xi}\Big) + i\beta\hat{p}\bar{w} + \\
&\gamma\Big(c\,\hat{p}\Big(\sinh(\xi)\cos(\eta)\Big(\frac{\partial\bar{u}}{\partial\xi} + \frac{\partial\bar{v}}{\partial\eta}\Big) + \cosh(\xi)\sin(\eta)\Big(\frac{\partial\bar{u}}{\partial\eta} - \frac{\partial\bar{v}}{\partial\xi}\Big)\Big) + \\
&\bar{p}\Big(c\sinh(\xi)\cos(\eta)\Big(\frac{\partial\hat{u}}{\partial\xi} + \frac{\partial\hat{v}}{\partial\eta}\Big) + c\cosh(\xi)\sin(\eta)\Big(\frac{\partial\hat{u}}{\partial\eta} - \frac{\partial\hat{v}}{\partial\xi}\Big) + i\beta\hat{w}\Big)\Big)\Big\} +
\end{aligned}
\tag{C.8}
$$

$$
\begin{aligned}
&c\frac{(\gamma-1)Ma^2}{Re}\Big(\frac{1}{2}c\Big(2\frac{d\lambda}{dT}\Big(\cosh(\xi)\Big(\frac{\partial\bar{u}}{\partial\eta} - \frac{\partial\bar{v}}{\partial\xi}\Big)\sin(\eta) + \cos(\eta)\Big(\frac{\partial\bar{u}}{\partial\xi} + \frac{\partial\bar{v}}{\partial\eta}\Big)\sinh(\xi)\Big)^2 + \\
&\frac{d\mu}{dT}\Big(2\Big(2\cosh^2(\xi)\sin^2(\eta) + \cos^2(\eta)\sinh^2(\xi)\Big)\Big(\frac{\partial\bar{u}}{\partial\eta}\Big)^2 + \\
&\Big(4\cos^2(\eta)\frac{\partial\bar{v}}{\partial\xi}\sinh^2(\xi) + \Big(\frac{\partial\bar{u}}{\partial\xi} + \frac{\partial\bar{v}}{\partial\eta}\Big)\sin(2y)\sinh(2x)\Big)\frac{\partial\bar{u}}{\partial\eta} - \\
&(\cos(2y) - \cosh(2x))\Big(\Big(\frac{\partial\bar{w}}{\partial\eta}\Big)^2 + \Big(\frac{\partial\bar{w}}{\partial\xi}\Big)^2\Big) + 2\Big(\Big(\cosh^2(\xi)\sin^2(\eta) + 2\cos^2(\eta)\sinh^2(\xi)\Big)\Big(\frac{\partial\bar{u}}{\partial\xi}\Big)^2 - \\
&2\cos(\eta)\cosh(\xi)\frac{\partial\bar{v}}{\partial\xi}\sin(\eta)\sinh(\xi)\frac{\partial\bar{u}}{\partial\xi} - 2\cosh(\xi)\frac{\partial\bar{v}}{\partial\eta}\sin(\eta)\Big(\cosh(\xi)\frac{\partial\bar{u}}{\partial\xi}\sin(\eta) + \cos(\eta)\frac{\partial\bar{v}}{\partial\xi}\sinh(\xi)\Big) + \\
&\Big(\frac{\partial\bar{v}}{\partial\xi}\Big)^2\Big(2\cosh^2(\xi)\sin^2(\eta) + \cos^2(\eta)\sinh^2(\xi)\Big) + \\
&\Big(\frac{\partial\bar{v}}{\partial\eta}\Big)^2\Big(\cosh^2(\xi)\sin^2(\eta) + 2\cos^2(\eta)\sinh^2(\xi)\Big)\Big)\Big)\Big)\hat{T} + \\
&2\bar{\mu}\Big(\frac{1}{2}c\Big(-(\cos(2y) - \cosh(2x))\Big(\frac{\partial\bar{w}}{\partial\eta}\frac{\partial\hat{w}}{\partial\eta} + \frac{\partial\bar{w}}{\partial\xi}\frac{\partial\hat{w}}{\partial\xi}\Big) + \\
&2\frac{\partial\bar{u}}{\partial\eta}\Big(\cos(\eta)\sinh(\xi)\Big(\cosh(\xi)\Big(\frac{\partial\hat{u}}{\partial\xi} + \frac{\partial\hat{v}}{\partial\eta}\Big)\sin(\eta) + \cos(\eta)\frac{\partial\hat{v}}{\partial\xi}\sinh(\xi)\Big) + \\
&\frac{\partial\hat{u}}{\partial\eta}\Big(2\cosh^2(\xi)\sin^2(\eta) + \cos^2(\eta)\sinh^2(\xi)\Big)\Big) + 2\frac{\partial\bar{v}}{\partial\eta}\Big(\cos(\eta)\cosh(\xi)\frac{\partial\hat{u}}{\partial\eta}\sin(\eta)\sinh(\xi) - \\
&\cosh(\xi)\sin(\eta)\Big(\cosh(\xi)\frac{\partial\hat{u}}{\partial\xi}\sin(\eta) + \cos(\eta)\frac{\partial\hat{v}}{\partial\xi}\sinh(\xi)\Big) + \frac{\partial\hat{v}}{\partial\eta}\Big(\cosh^2(\xi)\sin^2(\eta) + \\
&2\cos^2(\eta)\sinh^2(\xi)\Big)\Big) + 2\Big(-\cosh(\xi)\frac{\partial\hat{v}}{\partial\eta}\sin(\eta)\Big(\cosh(\xi)\frac{\partial\bar{u}}{\partial\xi}\sin(\eta) + \cos(\eta)\frac{\partial\bar{v}}{\partial\xi}\sinh(\xi)\Big) + \\
&\cos(\eta)\frac{\partial\hat{u}}{\partial\eta}\sinh(\xi)\Big(\cosh(\xi)\frac{\partial\bar{u}}{\partial\xi}\sin(\eta) + \cos(\eta)\frac{\partial\bar{v}}{\partial\xi}\sinh(\xi)\Big) + \\
&\frac{\partial\hat{v}}{\partial\xi}\Big(\frac{\partial\bar{v}}{\partial\xi}\Big(2\cosh^2(\xi)\sin^2(\eta) + \cos^2(\eta)\sinh^2(\xi)\Big) - \cos(\eta)\cosh(\xi)\frac{\partial\bar{u}}{\partial\xi}\sin(\eta)\sinh(\xi)\Big) + \\
&\frac{\partial\hat{u}}{\partial\xi}\Big(\frac{\partial\bar{u}}{\partial\xi}\Big(\cosh^2(\xi)\sin^2(\eta) + 2\cos^2(\eta)\sinh^2(\xi)\Big) - \cos(\eta)\cosh(\xi)\frac{\partial\bar{v}}{\partial\xi}\sin(\eta)\sinh(\xi)\Big)\Big)\Big) + \\
&i\beta\Big(\cosh(\xi)\frac{\partial\bar{w}}{\partial\eta}\sin(\eta) + \cos(\eta)\frac{\partial\bar{w}}{\partial\xi}\sinh(\xi)\Big)\hat{u} + \\
&i\beta\Big(\cos(\eta)\frac{\partial\bar{w}}{\partial\eta}\sinh(\xi) - \cosh(\xi)\frac{\partial\bar{w}}{\partial\xi}\sin(\eta)\Big)\hat{v}\Big) + 2\Big(\cosh(\xi)\Big(\frac{\partial\bar{u}}{\partial\eta} - \frac{\partial\bar{v}}{\partial\xi}\Big)\sin(\eta) + \\
&\cos(\eta)\Big(\frac{\partial\bar{u}}{\partial\xi} + \frac{\partial\bar{v}}{\partial\eta}\Big)\sinh(\xi)\Big)\bar{\lambda}\Big(c\cosh(\xi)\Big(\frac{\partial\hat{u}}{\partial\eta} - \frac{\partial\hat{v}}{\partial\xi}\Big)\sin(\eta) + c\cos(\eta)\Big(\frac{\partial\hat{u}}{\partial\xi} + \frac{\partial\hat{v}}{\partial\eta}\Big)\sinh(\xi) + i\beta\hat{w}\Big)\Big)
\end{aligned}
\tag{C.9}
$$

$$\frac{1}{2}-\frac{1}{(RePr)}\left\{\bar{k}\left(c^2(-(\cos(2\eta)-\cosh(2\xi)))\left(\frac{\partial^2\hat{T}}{\partial\eta^2}+\frac{\partial^2\hat{T}}{\partial\xi^2}\right)-2\beta^2\hat{T}\right)-\right.$$
$$c^2(\cos(2\eta)-\cosh(2\xi))\left(\frac{d^2k}{dT^2}\hat{T}\left(\left(\frac{\partial\bar{T}}{\partial\eta}\right)^2+\left(\frac{\partial\bar{T}}{\partial\xi}\right)^2\right)+\right. \tag{C.10}$$
$$\left.\left.\frac{dk}{dT}\left(\hat{T}\left(\frac{\partial^2\bar{T}}{\partial\eta^2}+\frac{\partial^2\bar{T}}{\partial\xi^2}\right)+2\frac{\partial\hat{T}}{\partial\eta}\frac{\partial\bar{T}}{\partial\eta}+2\frac{\partial\hat{T}}{\partial\xi}\frac{\partial\bar{T}}{\partial\xi}\right)\right)\right\}$$

Bibliography

Abdessemed, N., Sharma, A. S., Sherwin, S. and Theofilis, V.: 2009, Transient growth analysis of the flow past a circular cylinder, *Physics of Fluids* **21**(4), 044103.

Adamczak, D., Kimmel, R., team Brisbane, T. D. A., Paull, A. and Alesi, H.: 2011, Hifire-1 flight trajectory estimation and initial experimental results, *17th AIAA International Space Planes and Hypersonic Systems and Technologies Conference*, p. 2358.

Albensoeder, S., H. C., K. and H. J., R.: 2001, Three-dimensional centrifugal-flow instabilities in the lid-driven-cavity problem, *Physics of fluids* **13.1**, 121–135.

Andersson, P., Berggren, M. and Henningson, D. S.: 1999, Optimal disturbances and bypass transition in boundary layers., *Phys. Fluids* **11**(1), 134–150.

Archer: n.d., Cray XC30, http://www.archer.ac.uk/. Accessed: 2018-10-18.

Arnoldi, W. E.: 1951, The principle of minimized iterations in the solution of the matrix eigenvalue problem, *Quarterly of Applied Mathematics* **9**, 17–29.

Bagheri, S. and Hanifi, A.: 2007, The stabilizing effect of streaks on Tollmien-Schlichting and oblique waves: A parametric study, *Phys. Fluids* **19**, 078103.

Bippes, H.: 1991, Experiments on transition in three-dimensional accelerated boundary-layer flows, *RAS Conf. on Boundary layer transition and control*, Cambridge, England.

Blackford, L. S., Choi, J., Cleary, A., D'Azevedo, E., Demmel, J., Dhillon, I., Dongarra, J., Hammarling, S., Henry, G., Petitet, A. et al.: 1997, *ScaLAPACK users' guide*, Vol. 4, Siam.

Borg, M., Kimmel, R. and Stanfield, S.: 2011, Hifire-5 attachment-line and crossflow instability in a quiet hypersonic wind tunnel, AIAA 2011-3247, 41st AIAA Fluid Dynamics Conference and Exhibit 27 - 30 June 2011, Honolulu, Hawaii.

Borg, M., Kimmel, R. and Stanfield, S.: 2012, Traveling crossflow instability for hifire-5 in a quiet hypersonic wind tunnel, *43rd AIAA Fluid Dynamics Conference*, p. 2737.

Borrill, J.: 1999, Madcap: The microwave anisotropy dataset computational analysis package, *Proceedings of the 5th European SGI/Cray MPP Workshop* .

Boyd, J.: 1989, *Chebyshev & Fourier Spectral Methods*, Springer-Verlag.

Bridges, T. and Morris, P.: 1984a, Differential eigenvalue problems in which the parameter appears nonlinearly, *Journal of Computational Physics* **55**(3), 437–460.

Bridges, T. and Morris, P.: 1984b, Differential eigenvalue problems in which the parameter appears nonlinearly, *J. Comp. Phys.* **55**, 437–460.

Broadhurst, M. and Sherwin, S.: 2008, The parabolised stability equations for 3d-flows: implementation and numerical stability, *Applied Numerical Mathematics* **58**(7), 1017–1029.

Canuto, C., Hussaini, M., Quarteroni, A. and Zang, T.: 1988, *Spectral Methods*, Springer.

Choudhari, M., Chang, C.-L., Jentink, T., Li, F., Berger, K., Candler, G. and Kimmel, R.: 2009, Transition analysis for the hifire-5 vehicle, *39th AIAA Fluid Dynamics Conference*. AIAA Pap 2009–4056.

Chu, B.-T.: 1965, On the energy transfer to small disturbances in fluid flow (part i), *Acta Mechanica* **1**(3), 215–234.

Copper: n.d., Cray XE6m, https://www.ors.hpc.mil/. Accessed: 2018-10-18.

Corbett, P. and Bottaro, A.: 2001a, Optimal linear growth in swept boundary layers, *Journal of Fluid Mechanics* **435**, 1–23.

Corbett, P. and Bottaro, A.: 2001b, Optimal linear growth in swept boundary layers, *J. Fluid Mech.* **435**, 1–23.

Cossu, C. and Brandt, L.: 2002, Stabilization of Tollmien-Schlichting waves by finite amplitude optimal streaks in the Blasius boundary layer, *Phys. Fluids* **14**, L57.

De Tullio, N., Paredes, P., Sandham, N. and Theofilis, V.: 2013, Laminar–turbulent transition induced by a discrete roughness element in a supersonic boundary layer, *Journal of Fluid Mechanics* **735**, 613–646.

Dolvin, D.: 2008, Hypersonic international flight research and experimentation (hifire) fundamental science and technology development strategy, *15th AIAA International Space Planes and Hypersonic Systems and Technologies Conference*, p. 2581.

Drazin, P., Reid, W. and Busse, F.: 1982, Hydrodynamic stability.

Farrell, B. F. and Ioannou, P. J.: 1996, Generalized stability theory. part i: Autonomous operators, *Journal of the atmospheric sciences* **53**(14), 2025–2040.

Fedorov, A.: 2011, Transition and stability of high-speed boundary layers, *Annual Review of Fluid Mechanics* **43**, 79–95.

Fei, L., Choudhari, M., Chang, C.-L., Kimmel, R., Adamczak, D. and Smith, M.: 2011, Transition analysis for the hifire-1 flight experiment, *41st AIAA Fluid Dynamics Conference and Exhibit*, p. 3414.

Fransson, J., Brandt, L., Talamelli, A. and Cossu, C.: 2005, Experimental study of the stabilization of Tollmien-Schlichting waves by finite amplitude streaks, *Phys. Fluids* **17**, 054110.

Gennaro, E. M., D., R., M. A. F., M. and Theofilis, V.: 2013, Sparse techniques in global flow instability with application to compressible leading-edge flow, *AIAA journal* **51.9**, 2295–2303.

Gómez, F., Paredes, P., Gómez, R. and Theofilis, V.: 2012, Global stability of cubic and large aspect ratio three-dimensional lid-driven cavities, AIAA 2012-3274.

Gosse, R., Kimmel, R. and Johnson, H.: 2010, Cfd study of the hifire-5 flight experiment, *40th Fluid Dynamics Conference and Exhibit*, AIAA Pap. 2010-4854.

Gosse, R., Kimmel, R. and Johnson, H. B.: 2013, Study of boundary-layer transition on hypersonic international flight research experimentation 5, *Journal of Spacecraft and Rockets* **51**(1), 151–162.

Hanifi, A., Henningson, D., Hein, S., Bertolotti, F. and Simen, M.: 1994, Linear nonlocal instability analysis - the linear NOLOT code, *Technical Report TN 1994-54*, FFA.

Hanifi, A., Schmid, P. J. and Henningson, D. S.: 1996a, Transient growth in compressible boundary layer flow, *Physics of Fluids* **8**(3), 826–837.

Hanifi, A., Schmid, P. J. and Henningson, D. S.: 1996b, Transient growth in compressible boundary layer flow, *Phys. Fluids* **8**(3), 826–837.

He, W., Gioria, R., Pérez, J. and Theofilis, V.: 2017, Linear instability of low reynolds number massively separated flow around three naca airfoils, *Journal of Fluid Mechanics* **811**, 701–741.

Heeg, R. S. and Geurts, B. J.: 1997, Spatial instabilities of the incompressible attachment-line flow using sparse matrix jacobi–davidson techniques, *Applied scientific research* **59**(4), 315–329.

Hein, S.: 2005, *Nonlinear nonlocal transition analysis*, PhD thesis, University of Stuttgart. DLR-FD 2005-10.

Hein, S., Bertolotti, F., Simen, M., Hanifi, A. and Henningson, D.: 1994, Linear nonlocal instability analysis - the linear NOLOT code, *Technical Report IB 223-94 A56*, DLR.

Henningson, D.: 1996, Comment on "transition in shear flows. nonlinear normality versus non-normal linearity"[phys. fluids 7, 3060 (1995)], *Physics of Fluids* **8**(8), 2257–2258.

Herbert, T.: 1994, Parabolized stability equations, *AGARD Report No. 793. Special Course on Progress in Transition Modelling* pp. 4(1)–4(34).

Herbert, T.: 1997, Parabolized stability equations, *Ann. Rev. Fluid Mech.* **29**, 245–283.

Högberg, M. and Henningson, D. S.: 1998, Secondary instability of cross-flow vortices in Falkber-Skan-Cooke boundary layers, *J. Fluid Mech.* **368**, 339–357.

Holden, M. S.: 1998, Experimental studies of laminar, transitional, and turbulent hypersonic flows over elliptic cones at angles of attack, *Technical report*, CALSPAN UB RESEARCH CENTER BUFFALO NY.

Kimmel, R.: 2008, Aerothermal design for the hifire flight vehicle, *38th Fluid Dynamics Conference and Exhibit*, p. 4034.

Kimmel, R., Adamczak, D., Berger, K. and Choudhari, M.: 2010, Hifire-5 flight vehicle design, *40th Fluid Dynamics Conference and Exhibit*, p. 4985.

Kimmel, R., Adamczak, D., Gaitonde, D., Rougeux, A. and Hayes, J.: 2007, Hifire-1 boundary layer transition experiment design, *45th AIAA Aerospace Sciences Meeting and Exhibit*, p. 534.

Kimmel, R., Adamczak, D., Paull, A., Paull, R., Shannon, J., Pietsch, R., Frost, M. and Alesi, H.: 2011, Hifire-1 preliminary aerothermodynamic measurements, *41st AIAA Fluid Dynamics Conference and Exhibit*, p. 3413.

Kimmel, R. L. and Poggie, J.: 1997a, Three-dimensional hypersonic boundary layer stability and transition, *Technical report*, AIR FORCE RESEARCH LAB WRIGHT-PATTERSON AFB OH AIR VEHICLES DIRECTORATE.

Kimmel, R. L. and Poggie, J.: 1997b, Transition on an elliptic cone at mach 8, *American Society of Mechanical Engineers ASME FEDSM97-3111* .

Kimmel, R. L., Poggie, J. and Schwoerke, S. N.: 1999, Laminar-turbulent transition in a mach 8 elliptic cone flow, *AIAA journal* **37**(9), 1080–1087.

Levin, O. and Henningson, D.: 2003, Exponential vs algebraic growth and transition prediction in boundary layer flow, *Flow, Turbl. Combust.* **70**(183).

Li, F. and Malik, M.: 1994, Mathematical nature of parabolized stability equations, *R. Kobayashi (Ed.), Laminar-Turbulent Transition, Springer* pp. 205–212.

Li, F. and Malik, M.: 1997, Spectral analysis of parabolized stability equations, *Computers and Fluids* **26 (3)**, 279–297.

Lin, C. C.: 1955, Hydrodynamic stability, *Cambridge, UP* .

Lin, R. S. and Malik, M. R.: 1995, Stability and transition in compressible attachment-line boundary-layer flow, *SAE Pap. 952041* .

Lyttle, I. and Reed, H.: 1995, Use of transition correlations for three-dimensional boundary layers within hypersonic flows, AIAA 95-2293.

Mack, C., Schmid, P. and Sesterhenn, J. S.: 2008, Global stability of swept flow around a parabolic body: connecting attachment-line and crossflow modes, *J. Fluid Mech.* **611**, 205 – 215.

Mack, L.: 1969, Boundary layer stability theory. report 900-277 rev. a, *Jet Propulsion Laboratory, Pasadena, CA* **22**.

Mack, L.: 1984, Boundary-layer stability theory, *AGARD Report No. 709. Special Course on Stability and Transition of Laminar Flow* pp. 3–1–3–81.

Moller, C. and Van Loan, C.: 2003, Nineteen dubious ways to compute the exponential of a matrix, *SIAM Review* .

Morkovin, M.: 1994, Transition in open flow systems-a reassessment, *Bull. Am. Phys. Soc.* **39**, 1882.

Paredes, P.: 2014, *Advances in global instability computations: from incompressible to hypersonic flow*, Phd thesis, Technical University of Madrid.

Paredes, P., Choudhari, M. M. and Li, F.: 2017a, Blunt-body paradox and transient growth on a hypersonic spherical forebody, *Physical Review Fluids* **2**(5), 053903.

Paredes, P., Choudhari, M. M. and Li, F.: 2017b, Instability wave–streak interactions in a supersonic boundary layer, *Journal of Fluid Mechanics* **831**, 524–553.

Paredes, P., Choudhari, M. M. and Li, F.: 2018, Blunt-body paradox and improved application of transient-growth framework, *AIAA Journal* pp. 1–11.

Paredes, P., Gosse, R., Theofilis, V. and Kimmel, R.: 2016a, Linear modal instabilities of hypersonic flow over an elliptic cone, *Journal of Fluid Mechanics* **804**, 442–466.

Paredes, P., Gosse, R., Theofilis, V. and Kimmel, R.: 2016b, Linear modal instabilities of hypersonic flow over an elliptic cone, *J. Fluid Mech.* **804**, 442–466.

Paredes, P., Hermanns, M., Clainche, S. L. and Theofilis, V.: 2013, Order 10^4 speedup in global linear instability analysis using matrix formation, *Comput. Meth. Appl. Mech. Eng.* **253**, 287–304.

Paredes, P., Hermanns, M., Le Clainche, S. and Theofilis, V.: 2013, Order 10^4 speedup in global linear instability analysis using matrix formation, *Computer Methods in Applied Mechanics and Engineering* **253**, 287–304.

Paredes, P. and Theofilis, V.: 2015, Centerline instabilities on the hypersonic international flight research experimentation hifire-5 elliptic cone model, *Journal of Fluids and Structures* **53**, 36–49.

Raghavendar, J. and Dharmaiah, V.: 2017, Geometrical interpretation of singular value decomposition(svd) and applications of svd, *International Journal of Scientific and Innovative Mathematical Research* **5**(4), 23–26.

Reddy, S. C. and Henningson, D. S.: 1993, Energy growth in viscous channel flows, *Journal of Fluid Mechanics* **252**, 209–238.

Reed, H. L. and Saric, W. S.: 1989, Stability of three-dimensional boundary layers, *Annu. Rev. Fluid Mech.* **21**, 235–284.

Rodríguez, D., Tumin, A. and Theofilis, V.: 2011, Towards the foundation of a global modes concept, AIAA 2011-3603.

Rosenhead, V.: 1963, Laminar boundary layers, *Oxford University Press*.

Saad, Y.: 1980, Variations on arnoldi's method for computing eigenelements of large unsymmetric matrices, *Linear algebra and its applications* **34**, 269–295.

Schmid, P. and Henningson, D. S.: 2001, *Stability and transition in shear flows*, Springer.

Schmid, P. J.: 2007, Nonmodal stability theory, *Annu. Rev. Fluid Mech.* **39**, 129–162.

Schmid, P. J. and Brandt, L.: 2014, Analysis of fluid systems: Stability, receptivity, sensitivitylecture notes from the flow-nordita summer school on advanced instability methods for complex flows, stockholm, sweden, 2013, *Applied Mechanics Reviews* **66**(2), 024803.

Schmid, P. J. and Henningson, D. S.: 1994, Optimal energy density growth in hagen–poiseuille flow, *Journal of Fluid Mechanics* **277**, 197–225.

Schmidt, O. T. and Rist, U.: 2011, Linear stability of compressible flow in a streamwise corner, *Journal of Fluid Mechanics* **688**, 569–590.

Schmisseur, J., Schneider, S. and Collicott, S.: 1998, Receptivity of the Mach-4 boundary-layer on an elliptic cone to laser-generated localized free stream perturbations, AIAA 98-0532.

Schmisseur, J., Schneider, S. and Collicott, S.: 1999, Response of the Mach-4 boundary layer on an elliptic cone to laser-generated free stream perturbations, AIAA 99-0410.

Schneider, S. P.: 2004, Hypersonic laminar–turbulent transition on circular cones and scramjet forebodies, *Progress in Aerospace Sciences* **40**(1-2), 1–50.

Stanfield, S., Kimmel, R. and Adamczak, D.: 2012, Hifire-1 flight data analysis: Turbulent shock-boundary-layer interaction experiment during ascent, *42nd AIAA Fluid Dynamics Conference and Exhibit*, p. 2703.

Taira, K., Brunton, S. L., Dawson, S. T. M., Rowley, C. W., Colonius, T., McKeon, B. J., Schmidt, O. T., Gordeyev, S., Theofilis, V. and Ukeiley, L. S.: 2017, Modal analysis of fluid flows: An overview, *AIAA J.* **55**(12), 4013–4041.

Taira, K. and Colonius, T.: 2009, Three-dimensional flows around low-aspect-ratio flat-plate wings at low reynolds numbers, *J. Fluid Mech.* **623**, 187–207.

Tatsumi, T. and Yoshimura, T.: 1990, Stability of the laminar flow in a rectangular duct, *Journal of Fluid Mechanics* **212**, 437–449.

Tempelmann, D., Hanifi, A. and Henningson, D. S.: 2010, Spatial optimal growth in three-dimensional boundary layers, *Journal of Fluid Mechanics* **646**, 5–37.

Tempelmann, D., Schrader, L.-U., Hanifi, A., Brandt, L. and Henningson, D. S.: 2012, Swept wing boundary-layer receptivity to localized surface roughness, *Journal of Fluid Mechanics* **711**, 516–544.

Theofilis, V.: 1995, Spatial stability of incompressible attachment line flow, *Theor. Comput. Fluid Dyn.* **7**, 159–171.

Theofilis, V.: 2000, Globally unstable basic flows in open cavities, *6th Aeroacoustics Conference and Exhibit*, p. 1965.

Theofilis, V.: 2003, Advances in global linear instability analysis of nonparallel and three-dimensional flows, *Progress in Aerospace Sciences* **39**(4), 249–315.

Theofilis, V.: 2007, On instability properties of incompressible laminar separation bubbles on a at plate prior to shedding, *AIAA Paper 2007-0540* .

Theofilis, V.: 2011a, Global linear instability, *Annual Review of Fluid Mechanics* **43**, 319–352.

Theofilis, V.: 2011b, Pse-3d instability analysis and application to flow over an elliptic cone, *Technical Report FA8655-06-1-3066*, EOARD Final Report.

Theofilis, V.: 2017, The linearized pressure poisson equation for global instability analysis of incompressible flows, *Theor. Comp. Fluid Dyn.* **31**, 623–642.

Theofilis, V., Fedorov, A. and Collis, S.: 2004, Leading-edge boundary layer flow - Prandtl's vision, current developments and future perspectives, *IUTAM Symposium on One Hundred Years of Boundary Layer Research* **129**.

Theofilis, V., Fedorov, A. V., Obrist, D. and Dallmann, U. C.: 2003, The extended Görtler-Hämmerlin model for linear instability of three-dimensional incompressible swept attachment-line boundary layer flow, *J. Fluid Mech.* **487**, 271–313.

Theofilis, V., Hein, S. and Dallmann, U.: 2000, On the origins of unsteadiness and three-dimensionality in a laminar separation bubble, *Philosophical Transactions of the Royal Society of London A: Mathematical, Physical and Engineering Sciences* **358**(1777), 3229–3246.

Timme, S. and Badcock, K. J.: 2011, Transonic aeroelastic instability searches using sampling and aerodynamic model hierarchy, *AIAA J.* **49**(6), 1191–1201.

Timme, S., Badcock, K. J., Wu, M. and Spence, A.: 2012, Lyapunov inverse iteration for stability analysis using computational fluid dynamics, *53rd AIAA/ASME/ASCE/AHS/ASC Structures, Structural Dynamics and Materials Conference*, AIAA Paper 2012-1563, 23 - 27 April 2012, Honolulu, Hawaii, USA.

Trefethen, L. N.: 1992, Pseudospectra of matrices, *in* D. F. Griffiths and G. A. Watson (eds), *Numerical Analysis 1991*, Longman Scientific & Technical, Harlow, Essex, UK, pp. 234–265.

Trefethen, L. N.: 1997, Pseudospectra of linear operators, *SIAM review* **39**(3), 383–406.

Trefethen, L. N. and Embree, M.: 2005, *Spectra and pseudospectra: the behavior of nonnormal matrices and operators*, Princeton University Press.

Trefethen, L. N., Trefethen, A. E., Reddy, S. C. and Driscoll, T. A.: 1993, Hydrodynamic stability without eigenvalues, *Science* **261**(5121), 578–584.

Tumin, A. and Reshotko, E.: 2001, Spatial theory of optimal disturbances in boundary layers, *Physics of Fluids* **13**(7), 2097–2104.

Tumin, A. and Reshotko, E.: 2003, Optimal disturbances in compressible boundary layers, *AIAA journal* **41**(12), 2357–2363.

Waleffe, F.: 1995, Transition in shear flows. nonlinear normality versus non-normal linearity, *Physics of Fluids* **7**(12), 3060–3066.

Zuccher, S., Shalaev, I., Tumin, A. and Reshotko, E.: 2007, Optimal disturbances in the supersonic boundary layer past a sharp cone, *AIAA journal* **45**(2), 366–373.

Zuccher, S., Tumin, A. and Reshotko, E.: 2006, Parabolic approach to optimal perturbations in compressible boundary layers, *Journal of Fluid Mechanics* **556**, 189–216.